

2003

# Large eddy simulation of compressible turbulent pipe flow with heat transfer

Xiaofeng Xu  
Iowa State University

Follow this and additional works at: <https://lib.dr.iastate.edu/rtd>

 Part of the [Mechanical Engineering Commons](#)

## Recommended Citation

Xu, Xiaofeng, "Large eddy simulation of compressible turbulent pipe flow with heat transfer " (2003). *Retrospective Theses and Dissertations*. 1477.

<https://lib.dr.iastate.edu/rtd/1477>

This Dissertation is brought to you for free and open access by the Iowa State University Capstones, Theses and Dissertations at Iowa State University Digital Repository. It has been accepted for inclusion in Retrospective Theses and Dissertations by an authorized administrator of Iowa State University Digital Repository. For more information, please contact [digirep@iastate.edu](mailto:digirep@iastate.edu).

**Large eddy simulation of compressible turbulent pipe flow with heat transfer**

by

Xiaofeng Xu

A dissertation submitted to the graduate faculty  
in partial fulfillment of the requirements for the degree of  
**DOCTOR OF PHILOSOPHY**

Major: Mechanical Engineering

Program of Study Committee:  
Richard H. Pletcher, Major Professor  
Francine Battaglia  
Soma Chaudhuri  
Gerald M. Colver  
Ganesh R. Rajagopalan  
John C. Tannehill

Iowa State University

Ames, Iowa

2003

Copyright © Xiaofeng Xu, 2003. All rights reserved.

UMI Number: 3105120

**UMI**<sup>®</sup>

---

UMI Microform 3105120

Copyright 2003 by ProQuest Information and Learning Company.

All rights reserved. This microform edition is protected against  
unauthorized copying under Title 17, United States Code.

ProQuest Information and Learning Company  
300 North Zeeb Road  
P.O. Box 1346  
Ann Arbor, MI 48106-1346

Graduate College  
Iowa State University

This is to certify that the doctoral dissertation of  
Xiaofeng Xu  
has met the dissertation requirements of Iowa State University

Signature was redacted for privacy.

Major Professor

Signature was redacted for privacy.

For the Major Program

## TABLE OF CONTENTS

<b>LIST OF TABLES</b> . . . . .	vii
<b>LIST OF FIGURES</b> . . . . .	ix
<b>NOMENCLATURE</b> . . . . .	xiii
<b>ABSTRACT</b> . . . . .	xix
<b>CHAPTER 1. INTRODUCTION</b> . . . . .	1
1.1 Motivation . . . . .	1
1.2 Review of Internal Gas Flows with Property Variations . . . . .	3
1.2.1 Experiments and Turbulence Modeling . . . . .	3
1.2.2 DNS and LES Studies . . . . .	5
1.3 Objectives . . . . .	6
1.3.1 Develop an Efficient Finite Volume Scheme . . . . .	6
1.3.2 Validate a Second-Order Accurate Compressible Finite Volume Formu- lation for LES . . . . .	7
1.3.3 Validate the Finite Volume Formulation with Very Low Heat Transfer . . . . .	8
1.3.4 Study Capability of LES Formulation for the Turbulent Flow in a Vertical Pipe with Significant Variable Properties . . . . .	8
1.4 Dissertation Organization . . . . .	9
<b>CHAPTER 2. GOVERNING EQUATIONS</b> . . . . .	11
2.1 Compressible Navier-Stokes Equations . . . . .	11
2.2 Non-dimensionalization . . . . .	12
2.3 Filtering . . . . .	13

2.4	Favre Filtered Governing Equations . . . . .	15
2.5	Subgrid Scale Models . . . . .	20
2.5.1	Eddy Viscosity Model . . . . .	21
2.5.2	Smagorinsky SGS model . . . . .	21
2.5.3	Dynamic SGS model . . . . .	23
2.6	Integral-Vector Form of Favre Filtered Equations . . . . .	26
<b>CHAPTER 3. FINITE VOLUME FORMULATION . . . . .</b>		<b>29</b>
3.1	Spatial Discretization . . . . .	29
3.1.1	Dependent Variables . . . . .	29
3.1.2	Computational Domain . . . . .	30
3.1.3	Integral Approximations . . . . .	31
3.1.4	Gradients . . . . .	34
3.2	Low Mach Preconditioning . . . . .	37
3.3	LU-SGS Scheme . . . . .	39
3.4	Convergence Criterion . . . . .	44
3.5	Boundary Conditions . . . . .	45
3.5.1	Solid Wall Boundary Conditions . . . . .	45
3.5.2	Periodic Boundary Conditions . . . . .	46
3.5.3	Step-periodic Boundary Conditions . . . . .	47
<b>CHAPTER 4. RESULTS FOR THREE-DIMENSIONAL ISOTHERMAL</b>		
<b>TURBULENT FLOWS IN THIN ANNULAR AND PIPE PASSAGES .</b>		<b>48</b>
4.1	Annular Flow . . . . .	48
4.1.1	Boundary Conditions . . . . .	49
4.1.2	Simulation Details . . . . .	50
4.1.3	Results for Mean Flow and Velocity Statistics . . . . .	52
4.1.4	Instantaneous Vector Plot . . . . .	59
4.2	Pipe Flow . . . . .	59
4.2.1	Boundary Conditions . . . . .	63

4.2.2	Simulation Details . . . . .	63
4.2.3	Results of Turbulence Statistics . . . . .	66
4.2.4	Instantaneous Results . . . . .	73
4.2.5	Friction Coefficient . . . . .	74
4.3	Summary . . . . .	76
<b>CHAPTER 5. TURBULENT PIPE FLOW WITH LOW HEAT TRANSFER</b>		<b>79</b>
5.1	Problem Description . . . . .	79
5.2	Boundary Conditions . . . . .	80
5.3	Simulation Details . . . . .	82
5.4	Results for Temperature Statistics . . . . .	82
5.4.1	Friction Coefficients and Nusselt Numbers . . . . .	85
5.5	Summary . . . . .	90
<b>CHAPTER 6. LES OF MIXED CONVECTION IN A VERTICAL TUR-</b>		
<b>BULENT PIPE FLOW . . . . .</b>		<b>92</b>
6.1	Introduction . . . . .	92
6.2	Governing Equation . . . . .	94
6.2.1	Compressible Nondimensional Navier-Stokes (N-S) Equations . . . . .	94
6.2.2	Favre Filtered Equations . . . . .	95
6.3	Boundary Conditions . . . . .	96
6.4	Simulation Details . . . . .	97
6.5	Investigation of $\Delta T_x$ . . . . .	99
6.6	Results . . . . .	100
6.6.1	Averaged Flow Parameters . . . . .	100
6.6.2	Mean Profile . . . . .	102
6.6.3	Fluctuation Profiles . . . . .	111
6.6.4	Shear Stress and Heat Flux Profiles . . . . .	113
6.7	Instantaneous Results . . . . .	121
6.8	Friction Coefficient and Nusselt Number . . . . .	121

6.9 Summary . . . . .	132
<b>CHAPTER 7. CONCLUSIONS AND RECOMMENDATIONS . . . . .</b>	<b>136</b>
7.1 Summary . . . . .	136
7.2 Contributions . . . . .	137
7.3 Conclusions . . . . .	138
7.4 Recommendations for Future Work . . . . .	139
<b>APPENDIX A. JACOBIAN MATRICES FOR FAVRE FILTERED SYS-</b>	
<b>TEM OF EQUATIONS . . . . .</b>	<b>140</b>
<b>APPENDIX B. STREAMWISE TEMPERATURE DIFFERENCE FOR QUASI-</b>	
<b>DEVELOPED FLOW WITH HIGH HEAT TRANSFER . . . . .</b>	<b>142</b>
<b>BIBLIOGRAPHY . . . . .</b>	<b>144</b>
<b>ACKNOWLEDGMENTS . . . . .</b>	<b>153</b>

## LIST OF TABLES

Table 4.1	Control volume dimensions in streamwise and radial directions . . . . .	65
Table 4.2	Control volume dimensions in circumferential direction . . . . .	65
Table 4.3	Mean flow properties of LES, DNS and experiments . . . . .	66
Table 4.4	Comparison of friction coefficient with $48 \times 32 \times 64$ grid . . . . .	77
Table 4.5	Comparison of friction coefficient with $64 \times 40 \times 80$ grid . . . . .	77
Table 4.6	Comparison of friction coefficient with $64 \times 40 \times 100$ grid . . . . .	78
Table 5.1	Nusselt numbers and friction factors for the present simulations . . . . .	88
Table 5.2	Comparison to constant property correlations for friction coefficient with isoflux thermal boundary condition . . . . .	89
Table 5.3	Comparison to constant property correlations for friction coefficient with fixed wall temperature condition . . . . .	89
Table 5.4	Comparison to constant property correlations for Nusselt number with isoflux thermal boundary condition . . . . .	89
Table 5.5	Comparison to constant property correlations for friction coefficient with fixed wall temperature condition . . . . .	90
Table 6.1	Conditions for cases . . . . .	99
Table 6.2	Local bulk properties for LES . . . . .	102
Table 6.3	Local bulk properties for corresponding experiments . . . . .	102
Table 6.4	Comparison with variable property correlations for case 1 . . . . .	132
Table 6.5	Comparison with variable property correlations for case 2 . . . . .	133
Table 6.6	Comparison with variable property correlations for case 3 . . . . .	133

Table 6.7	Comparison with variable property correlations for case 4 . . . . .	134
Table 6.8	Comparison with variable property correlations for case 5 . . . . .	134
Table 6.9	Comparison with variable property correlations for case 6 . . . . .	135

## LIST OF FIGURES

3.1	Sketch of the computational domain and analogous domain . . . . .	30
3.2	Sketch of control volumes . . . . .	31
3.3	Non-Cartesian hexahedral control volume with cell center, $(i,j,k)$ , and six neighboring cell centers, labeled as E, W, N, S, U, and D . . . . .	32
3.4	Sketch of non-Cartesian the hexahedral volume for approximations of $v$ and $w$ at the D surface . . . . .	33
3.5	Non-Cartesian tetrahedral control volume with cell center, $(i,j,k)$ , and five neighboring cell centers, labeled as E, W, S, U, and D . . . . .	35
3.6	Auxiliary non-Cartesian hexahedral control volume for calculation of gradients on east/west (E/W) faces of the main control volume . . . . .	36
3.7	Sketch of grids in $yz$ plane . . . . .	41
3.8	Ghost cells for boundary conditions . . . . .	45
4.1	Geometry of annular: (a) cross section of computational domain, (b) cross section of annular . . . . .	49
4.2	Mean velocity profile in global coordinates . . . . .	53
4.3	Mean velocity profile in wall coordinates . . . . .	55
4.4	Velocity cross-correlation coefficient . . . . .	56
4.5	Root-mean-square of velocity fluctuations normalized by wall friction velocity . . . . .	57
4.6	Skewness factor of the velocity fluctuations . . . . .	58
4.7	Flatness factor of the velocity fluctuations . . . . .	60
4.8	Turbulent kinetic energy scaled by bulk velocity in global coordinates .	61

4.9	Turbulent kinetic energy in wall coordinates . . . . .	61
4.10	Instantaneous vector plot of $u_r$ and $u_\theta$ in cross section . . . . .	62
4.11	Pipe flow geometry and coordinate system . . . . .	63
4.12	Mean streamwise velocity profile in wall coordinates . . . . .	67
4.13	RMS velocity fluctuations normalized by wall friction velocity . . . . .	69
4.14	Skewness factor of the velocity fluctuations . . . . .	70
4.15	Flatness factor of the velocity fluctuations . . . . .	71
4.16	Shear stress distributions scaled by wall shear stress . . . . .	72
4.17	Total shear stress distribution scaled by wall shear stress . . . . .	73
4.18	Instantaneous velocity vector plot in the cross section of pipe . . . . .	74
4.19	Contours of instantaneous streamwise velocity in the $yz$ plane . . . . .	75
4.20	Contours of instantaneous streamwise velocity in the near wall region . . . . .	75
5.1	Schematic of pipe flow with constant wall heat flux, $q_w$ . . . . .	80
5.2	Mean temperature distribution in wall coordinates for very low heat flux case . . . . .	84
5.3	RMS of the temperature fluctuations normalized by friction temperature	85
5.4	Streamwise turbulent heat flux normalized by friction velocity and tem- perature . . . . .	86
5.5	Wall-normal turbulent heat flux normalized by friction velocity and temperature . . . . .	86
5.6	Cross-correlation coefficient between normal-to-wall velocity and tem- perature . . . . .	87
5.7	Cross-correlation coefficient between streamwise velocity and temperature	87
6.1	The configuration of vertical pipe flow . . . . .	98
6.2	Effects of different $\Delta T_x$ distributions on mean velocity profiles in case 4	101
6.3	Effects of different $\Delta T_x$ distributions on mean temperature profiles in case 4 . . . . .	101

6.4	Comparison of mean velocity between case 1 and experimental case 618	104
6.5	Comparison of mean velocity between case 2 and experimental case 635	104
6.6	Comparison of mean velocity between case 3 and experimental case 445	105
6.7	Comparison of mean velocity between case 4 and experimental case 618	105
6.8	Comparison of mean velocity between case 5 and experimental case 635	106
6.9	Comparison of mean velocity between case 6 and experimental case 445	106
6.10	Mean velocity profiles in wall coordinates . . . . .	107
6.11	Mean velocity profiles in semi-local coordinates . . . . .	107
6.12	Comparison of simulated mean temperature profile of case 1 and experimental case 618 . . . . .	108
6.13	Comparison of simulated mean temperature profile of case 2 and experimental case 635 . . . . .	108
6.14	Comparison of simulated mean temperature profile of case 3 and experimental case 445 . . . . .	109
6.15	Comparison of simulated mean temperature profile of case 4 and experimental case 618 . . . . .	109
6.16	Comparison of simulated mean temperature profile of case 1 and experimental case 635 . . . . .	110
6.17	Comparison of simulated mean temperature profile of case 2 and experimental case 445 . . . . .	110
6.18	Mean temperature in wall coordinates . . . . .	111
6.19	Mean temperature profiles normalized by bulk temperature . . . . .	112
6.20	Mean density profiles normalized by bulk density . . . . .	112
6.21	Mean streamwise momentum profiles . . . . .	113
6.22	Velocity fluctuations in wall coordinates . . . . .	114
6.23	Velocity fluctuations in semi-local coordinates . . . . .	115
6.24	Turbulent kinetic energy in wall coordinates . . . . .	116
6.25	Turbulent kinetic energy in semi-local coordinates . . . . .	116

6.26	Shear stress distributions normalized by wall shear stress . . . . .	118
6.27	Heat flux distributions normalized by wall heat flux . . . . .	119
6.28	Sum of resolved, viscous, and SGS shear stresses contributions normalized by wall shear stress . . . . .	120
6.29	Sum of resolved, conductive, and SGS heat flux distributions normalized by wall heat flux . . . . .	120
6.30	Instantaneous streamwise velocity for case 1 . . . . .	122
6.31	Instantaneous streamwise velocity for case 2 . . . . .	122
6.32	Instantaneous streamwise velocity for case 3 . . . . .	123
6.33	Instantaneous streamwise velocity for case 4 . . . . .	123
6.34	Instantaneous streamwise velocity for case 5 . . . . .	124
6.35	Instantaneous streamwise velocity for case 6 . . . . .	124
6.36	Instantaneous temperature for case 1 . . . . .	125
6.37	Instantaneous temperature for case 2 . . . . .	125
6.38	Instantaneous temperature for case 3 . . . . .	126
6.39	Instantaneous temperature for case 4 . . . . .	126
6.40	Instantaneous temperature for case 5 . . . . .	127
6.41	Instantaneous temperature for case 6 . . . . .	127
6.42	Instantaneous velocity vector plot for case 1 . . . . .	128
6.43	Instantaneous velocity vector plot for case 2 . . . . .	128
6.44	Instantaneous velocity vector plot for case 3 . . . . .	129
6.45	Instantaneous velocity vector plot for case 4 . . . . .	129
6.46	Instantaneous velocity vector plot for case 5 . . . . .	130
6.47	Instantaneous velocity vector plot for case 6 . . . . .	130

## NOMENCLATURE

### Roman Symbols

$[A], [B], [C]$	inviscid flux Jacobians
$A^+$	constant in Van Driest damping formula
$A_c$	pipe cross-sectional area ( $= \pi r^2$ )
$\mathbf{B}$	body force vector
$\mathbf{C}$	discretized convective and viscous flux vector
$C_d, C_i$	dynamic subgrid-scale model coefficients
$C_{ij}$	cross subgrid-scale stress tensor
$C_f$	friction coefficient ( $= 2\tau_w/(\rho_{ref}U_{ref}^2)$ )
$c$	speed of sound ( $= \sqrt{\gamma RT}$ )
$C_p$	constant pressure specific heat, coefficient of pressure
$C_v$	constant volume specific heat
$D$	Van Driest damping function or diameter of pipe
$D_h$	hydraulic diameter
$E$	specific energy
$\mathbf{E}, \mathbf{F}, \mathbf{G}$	flux vectors
$e$	specific internal energy ( $= C_v T$ )
$F$	flatness factor
$G$	filter function
$G_r$	Grashof number ( $= (gD_h^4 q_w)/(\nu_b^2 k_b T_b)$ )
$g$	gravitational constant

$H$	total enthalpy ( $= h + u_i u_i / 2$ )
$H_j$	resolved turbulent heat flux vector
$h$	heat transfer coefficient, or specific enthalpy
$\vec{i}, \vec{j}, \vec{k}$	unit vectors for Cartesian coordinate system
$K_v$	local acceleration parameter ( $= \frac{\nu_b}{u_b^2} \frac{du_b}{dx}$ )
$k$	wave number, thermal conductivity, or turbulent kinetic energy
$[L], [D], [U]$	approximate factorization matrices for LU-SGS scheme
$L_{ij}$	Leonard subgrid-scale stress tensor
$L_{ref}$	reference length
$L_x$	streamwise length of pipe
$M$	Mach number
$m$	pseudo time index
$m_i, m_j, m_k$	vertex number in streamwise, radius and circumferential directions
$\dot{m}$	dimensionless mass flow rate
$N_{stat}$	number of time steps for turbulent statistics
$Nu_D$	Nusselt number based on hydraulic diameter ( $= hD_h/k_b$ )
$n$	physical time index
$n_i, n_j, n_k$	control volume number in streamwise, radius and circumferential directions
$\vec{n}$	unit normal vector
$n_x, n_y, n_z$	components of unit normal vector
$Pr$	Prandtl number ( $= \mu c_p / k$ )
$Pr_t$	turbulent Prandtl number
$p$	thermodynamic pressure
$Q_j$	subgrid-scale turbulent heat flux vector
$Q_{tj}$	test filtered heat flux vector
$q_j$	heat flux vector
$q_{tj}$	Favre filtered heat flux vector
$q_w$	nondimensional wall heat flux

$R$	gas constant
$R_{ij}$	Reynolds subgrid-scale stress tensor
$\mathbf{R}$	residual vector
$r$	radius of pipe
$\mathfrak{R}$	preconditioned residual vector
$Ra$	Rayleigh number
$Re$	generic Reynolds number
$Re_D$	bulk Re based on hydraulic diameter ( $= \rho_b u_b D_h / \mu_b$ )
$Re_{ref}$	Re based on reference quantities ( $= \rho_{ref} V_{ref} L_{ref} / \mu_{ref}$ )
$Re_\tau$	Reynolds number based on friction velocity ( $= \rho_{ref} u_\tau D / \mu_{ref}$ )
$Re_\delta$	bulk Re based on half-distance between inner wall and outer wall of annular ( $= \rho_b u_b \delta / \mu_b$ )
$S$	magnitude of cell face area vector or skewness factor
$\vec{S}$	cell face area vector
$S_{ij}$	strain rate tensor
$T$	thermodynamic temperature
$T_b$	bulk temperature
$[T]$	time derivative Jacobian ( $= \partial \mathbf{W} / \partial \mathbf{U}$ )
TKE	turbulent kinetic energy
$T_\tau$	friction temperature ( $= q_w / (\rho_w C_p u_\tau)$ )
$T_w$	wall temperature
$T_{ij}$	test filtered stress tensor
$t$	physical time
$[U]$	vector of conserved variables $[\rho, \rho u, \rho v, \rho w, \rho E]^T$
$u_\tau$	friction velocity ( $= \sqrt{\tau_w / \rho_w}$ )
$u_\tau^*$	semi-local friction velocity ( $= \sqrt{\tau_w / \rho(y)}$ )
$u, v, w$	Cartesian velocity components in $x, y, z$ directions
$u, u_r, u_\theta$	Cylindrical velocity components in streamwise, radius and circumferential directions

$u^+$	velocity in wall coordinates ( $= u/u_\tau$ )
$u^*$	velocity in semi-local coordinates ( $= u/u_\tau^*$ )
$V_r$	reference velocity
$\mathbf{W}$	vector of primitive variables $[p, u, v, w, T]^T$
$x, y, z$	Cartesian coordinates
$y^+$	distance to wall in wall coordinates
$y^*$	distance to wall in semi-local coordinates

### Greek Symbols

$\alpha, \pi, \epsilon$	subgrid-scale terms in energy equation
$\beta$	pressure gradient parameter
$\Gamma$	time derivative preconditioning matrix
$\gamma$	ratio of specific heats
$\Delta$	grid filter width
$\hat{\Delta}$	test filter width
$\delta$	half distance between inner and outer wall of annular pipe or Kronecker delta
$\delta_y$	distance to closest wall
$\theta$	temperature difference ( $= T_w - T$ ) or circumferential direction of pipe
$\theta^+$	temperature in wall coordinates ( $= \theta/T_\tau$ )
$\kappa$	von Karman constant
$\lambda$	eigenvalue
$\mu$	molecular dynamic viscosity
$\mu_t$	subgrid-scale turbulent viscosity
$\nu$	molecular kinematic viscosity ( $= \mu/\rho$ )
$\nu_t$	subgrid-scale turbulent kinematic viscosity ( $= \mu_t/\rho$ )
$\rho$	thermodynamic density
$\sigma_{ij}$	shear stress tensor

$\tau$	pseudo time
$\tau_{ij}$	subgrid-scale stress tensor
$\Phi$	temperature gradient parameter
$\Omega$	cell volume

### Subscripts

$b$	bulk property
$g$	ghost cell quantity
$i, j, k$	indices for Cartesian coordinates
$inner, outer$	inner wall and outer wall of annular pipe
$inv$	inviscid contribution
$nw$	near wall cell quantity
$p$	periodic component
$ref$	reference quantity
$r$	associated with radius direction of pipe
$res$	resolved contribution
$rms$	root-mean-square
$s$ or $sgs$	subgrid-scale contribution
$v$ or $vis$	viscous contribution
$w$	wall value
$x, y, z$	associated with Cartesian direction
$\beta$	cell face index
$\theta$	associated with circumferential direction of pipe

### Superscripts and Other Symbols

*	dimensional variable or semi-local coordinates
---	--

*	dimensional variable
+	wall coordinates
'	fluctuation with respect to ensemble average, or unresolved or subgrid-scale component of filtered quantity
"	fluctuation with respect to Favre ensemble average, or unresolved or subgrid-scale component of Favre filtered quantity
→	vector quantity
—	resolved or large scale component of filtered quantity
~	resolved or large scale component of Favre filtered quantity
^	test filtered quantity
<>	ensemble averaged quantity
<> <sub>s</sub>	ensemble averaged in streamwise and circumferential directions

### Abbreviations

CFD	computational fluid dynamics
DNS	direct numerical simulation
LES	large eddy simulation
LU-SGS	lower-upper symmetric-Gauss-Seidel
MPI	message passing interface
NS	Navier-Stokes
RANS	Reynolds-averaged Navier-Stokes
RMS	root mean square
SGS	subgrid-scale
TKE	turbulent kinetic energy

## ABSTRACT

A compressible finite volume formulation for large eddy simulation (LES) of turbulent channel flows was extended to solve the turbulent flows in pipes and annular passages. A general finite volume scheme was developed based on conservation equations in Cartesian coordinates with non-Cartesian control volumes. A dual-time stepping approach with time derivative preconditioning was employed and time marching was done with an implicit lower-upper-symmetric-Gauss-Seidel (LU-SGS) scheme. The small scale motions were modeled by a dynamic subgrid-scale (SGS) model. The code was developed in a multiblock framework and parallelized using the message passing interface (MPI).

The finite volume LES formulation was validated by simulating the isothermal fully developed turbulent pipe and annular flows. The results were compared to experimental data and direct numerical simulation (DNS) results. The LES formulation was further validated by the simulation of turbulent pipe flows with low heat transfer and comparisons with passive scalar DNS results. Finally, buoyancy forces were added into the LES formulation to simulate mixed convection in a vertical pipe with constant high wall heat fluxes leading to significant property variations. Step-periodic boundary conditions were studied and implemented. The results were validated by comparing with experimental results. Heating effects and flow laminarization were studied.

Excellent agreement with DNS and experimental results were obtained for isothermal turbulent pipe and annular flows. The mean temperature profile for the turbulent pipe flow with low heat transfer matched very well with the DNS passive scalar results. Good matches to constant property correlations were also achieved for friction coefficients and Nusselt numbers.

For the mixed convection in a vertical pipe, good agreement with the experimental mean

streamwise velocity and temperature profiles was obtained. High heating tended to suppress the turbulent intensities and attenuate the turbulent kinetic energy. The thinner viscous layer led to a larger Nusselt numbers which indicated a higher heat transfer rate. Laminarization phenomena were observed along with large overprediction of friction coefficients and underprediction of Nusselt numbers when comparing to fully turbulent property variation correlations.

## CHAPTER 1. INTRODUCTION

### 1.1 Motivation

Turbulence is one of the important unresolved problems in engineering and science. Turbulent flow has a wide range of applications. It is difficult to give a precise definition of turbulence; the main characteristics of turbulence are randomness, diffusivity, dissipation, high level of fluctuating vorticity, coherent structures and large Reynolds number. It is well known that turbulent flows are governed by the three-dimensional Navier-Stokes equations along with appropriate forms of the continuity and energy equations. But the system of Navier-Stokes equations is naturally nonlinear and no deterministic solution exists for turbulent flows. Thus, no analytical solutions of turbulent flows in geometries of engineering interest are available. Although experimental studies can provide great insight towards the understanding of the structure of turbulent flows, they rely heavily on measurement techniques and are costly. Therefore it is of paramount importance to be able to simulate and predict the structure and characteristics of turbulent flows numerically.

The most common numerical approach used in engineering applications with limited computer resources is the Reynolds-averaged method, which is based on the idea first proposed by Osborne Reynolds. For the Reynolds-averaged Navier-Stokes equations (RANS) utilized in the Reynolds-averaged approach, the effect of turbulent fluctuations appearing in a Reynolds stress term must be modeled. This has given rise to a variety of closure methods which vary from simple zero-equation (algebraic) models, to two-equation models (the popular  $k-\epsilon$ ,  $k-\omega$  models), to very complicated Reynolds stress models. A review of the various methods under the RANS approach is given in Speziale (1991). However, the models for Reynolds stresses generally can not represent a wide range of length and time scales, so the more complex

configurations that exist, the more likely that it will fail or provide inaccurate results.

As computer hardware and algorithms improve, direct numerical simulations (DNS) of flows of practical interest will be possible. DNS is the most straightforward and accurate approach to the solution of turbulence. All of the scales, which range from large energy-carrying to the dissipative motions, are resolved in time and space. But this method is very costly; the number of the grid points is proportional to the  $9/4$  power of the Reynolds number. Also, it is difficult for the higher-order schemes used by DNS to handle complex geometries and general boundary conditions. Because of this, its application has been limited to simple geometries and low Reynolds numbers. It is not practical to use it in engineering-like applications.

Large eddy simulation (LES) in which modeling is required only for the smallest scales, is another approach to simulate turbulence, and it can provide nearly the same capability as DNS at a fraction of the cost. The contribution of the large, energy-carrying structures to momentum and energy transfer is computed exactly in LES. The effects of the smallest scales of turbulence are removed by a spatial filtering and are modeled as subgrid-scale (SGS) stress and heat flux terms. Since the small scales are more homogeneous and universal, and less affected by the geometry and boundary conditions than the large scales, they are more likely to be universally modeled requiring less adjustment when applied to different flows than models for the RANS equations. LES can be used at much higher Reynolds numbers than DNS because only the largest scales of motion must be calculated. Although LES requires less computer power than DNS, it is still relatively computer intensive, because even when LES solves a steady, two dimensional physical flow, it still requires a time-dependent, three-dimensional calculation in order to resolve scales larger than the filter scale. The application of LES has been also limited to simple geometries and low Reynolds number, but the limitations are not as restrictive as for DNS.

The main thrust of this research is to extend LES methodology to a broader class of flows, which are practical and with complex geometries. The present research focus is on using the LES method to simulate flows in tubes and annuli with heat transfer and providing valuable information to aid modern nuclear reactor design.

## 1.2 Review of Internal Gas Flows with Property Variations

This section provides a brief literature review on experiments and numerical simulations of internal gas flows with heat transfer. Specific attention is given to turbulent pipe flow and annular flow. For more detailed reviews on the effects of property variations on turbulent internal gas flows, the interested reader is referred to reviews by McEligot (1986), Jackson et al. (1989), Cotton and Kerwin (1995) and Nagano and Shimada (1995).

### 1.2.1 Experiments and Turbulence Modeling

Pipe and annular flow are often encountered in engineering applications such as advanced gas-cooled nuclear reactors, nuclear propulsion systems, and heat exchangers. The primary application for this research is for advanced gas-cooled reactors. To advance the technology for gas-cooled reactors, fundamental thermal fluid physics knowledge and measurements are necessary. The flows in advanced reactors are mostly turbulent flows with significant heat transfer leading to large property variations. In the early years, most experiments for gas heating with significant property variations were conducted with circular tubes of small diameters and forced convection dominated. The tubes were too small for probes to measure useful velocity and temperature profiles, so the experiments could only provide integral parameters, such as local heat transfer coefficients and friction coefficients (McEligot and Bankston, 1969; Bankston and McEligot, 1970; and Kawamura, 1979). Measurements of local heat transfer coefficients and friction factors for transitional and laminarizing flows have been obtained by Ogawa et al. (1982) and Ogawa and Kawamura (1986) with circular tubes. Local Nusselt numbers were measured for annuli by Fujii et al. (1991) and Torii et al. (1991). For dominant forced convection in low Mach number pipe flow with significant gas property variations, the only published mean profiles of temperature and velocity to guide the development of predictive turbulence models were measured by Perkins (1975) and Shehata and McEligot (1995). The measurements for velocity fluctuations and correlations are still unavailable for experiments. More detailed thermal features of turbulent flow with strong heating may be predicted by numerical simulations.

Generally, turbulence models have been developed with constant property idealization for the flows with high heating rates. Kawamura (1979) first successfully used a two-equation model of turbulence to analyze the laminarization of heated turbulent gas flow, and concluded that a modified  $k - kl$  model gave good agreement with the experiments. Fujii et al. (1991) employed three types of turbulence models for comparison to their measurements of strongly-heated turbulent gas flow in an annulus. Torii et al. (1991) and Torii and Yang (1997) applied modified  $k - \epsilon$  models for predicting streamwise variation of heat transfer parameters in low-Reynolds-number turbulent and laminarizing flows in circular tubes and annuli. Torri et al. (1993) also attempted to apply the Reynolds-stress model of Launder and Sharma (1974) to a circular tube, but the agreement was poor in the range of turbulent-to-laminar transition. However, all the above turbulence models were developed without guidance from measured velocity and temperature profiles.

For the most recent low-Reynolds-number turbulence models, validation focused on comparison to the measurements of mean velocity and temperature fields. Mikielewicz et al. (1994) conducted simulations for fully developed turbulent pipe flows with uniform wall heat flux and the constant properties idealization. Eleven models including a mixing length model, eddy diffusivity models, a one-equation  $k$  model and two-equation  $k - \epsilon$  type models were considered, but poor predictions were found. Shehata and McEligot (1998) examined the validity of the modified Van Driest mixing length model of McEligot and Bankston (1969) that was derived to account for property variations in the viscous layer due to high heating rates. Reasonably good predictions of mean internal profiles and nondimensional pressure drop were obtained. The Reynolds stress model (RSM) and the  $k - kl - \overline{u'v'}$  model which had been validated for gas flows in annular tubes were employed to predict the turbulent gas flows in circular tubes with significant property variation by Nishimura and Fujii (2000); both models resulted in good agreement with the experimental data on laminarizing flows measured by Shehata and McEligot (1998).

### 1.2.2 DNS and LES Studies

Although some turbulence models were found to give reasonable agreement with the experimental data, it is not certain that they could work well when extended to other conditions. With advances in computer technology, increasing attention is being given to direct numerical simulation (DNS) and large eddy simulation (LES) to predict more accurate results, particularly at low Reynolds number. Most DNS and LES studies have been for planar channel flows and the simulations for flows in circular and annular tubes are very sparse, especially with heat transfer.

Eggels (1994) performed DNS computations for pipe flows without heat transfer at low Reynolds number, and compared with experimental results (Eggels et al., 1994). Olandi, P. and Fatica, M. (1997) simulated a rotating pipe flow with a finite volume approach in cylindrical coordinates. Singularity was avoided by using the radial flux on a staggered grid. Based on the same idea, Japanese researchers have also developed a finite volume scheme without singularity for DNS of turbulent pipe flows (Satake and Kunugi, 1998a). Using the same approach, Satake and Kunugi (1998b) successfully simulated an axisymmetric impinging jet with outflow confined between two parallel discs. This approach was further extended by including the energy equation to predict flows in circular tubes with three thermal boundary conditions: uniform heat flux, a cosine distribution and circumferential non-uniform wall temperature (Satake and Kunugi, 1998c). DNS of turbulent heat transfer in an axially rotating pipe flow with uniform heat flux was also performed by Satake and Kunugi. (1998d).

The LES work for turbulent pipe flow is very limited. To the author's knowledge, the first LES of fully developed turbulent pipe flow was computed by Unger and Friedrich (1993). Eggels and Nieuwstadt (1993) simulated rotating pipe turbulent flow by LES. LES of turbulent flow in a curved pipe was reported by Boersma and Nieuwstadt (1996), and recently a dynamic subgrid scale model was used by Yang (2000) to simulate fully developed turbulent rotating pipe flow. No LES study for turbulent heat transfer in a circular tube has been reported; however, Kawamura et al. (1994) and Satake and Kawamura (1995) performed LES calculations for turbulent heat transfer in an annulus.

It should be noted that the passive scalar approach in which the effects of property variations were ignored was employed in the above simulations with heat transfer. Very few works where significant property variations were taken into account have been reported. LES studies for planar channel flow with significant property variations were reported by Wang and Pletcher (1996) and Dailey and Pletcher (1998). DNS studies for a channel flow with variable properties were also reported by Nicoud and Poinso (1999). Satake et al. (2000) performed DNS for a turbulent gas flow with variable properties to grasp and understand the laminarization phenomena caused by strong heating.

### 1.3 Objectives

The four main objectives of this research effort to extend LES capability to more practical flows are given below.

- Develop an efficient, time-accurate compressible finite volume scheme to solve the Favre filtered governing equations that govern the wall bounded flows in tubes and annular geometries.
- Validate the second-order accurate compressible finite volume formulation for LES by simulating incompressible turbulent flow in a pipe and annulus.
- Validate the finite volume formulation by simulating turbulent pipe flow with very low heat transfer
- Study the capability of the compressible LES formulation to simulate turbulent flow in a vertical pipe with significant variable properties.

#### 1.3.1 Develop an Efficient Finite Volume Scheme

Finite volume methods can handle complex geometries quite well and are commonly employed in many engineering CFD codes. Although finite volume methods for LES have been appeared recently, most of them are incompressible formulations. For example, they have been used to simulate homogeneous, isotropic decaying turbulence by Vreman et al. (1992), lid

driven cavity flows by Zang et al. (1993), turbulent flow around a circular cylinder by Mittal (1996), planar channel and rectangular duct flows by Wang and Pletcher (1995), and planar channel flows with rib roughened walls by Yang and Ferziger (1993). The compressible finite volume formulations are less common in LES. Wang and Pletcher (1996) used a staggered grid scheme with third-order upwinding for the convective terms, and fourth-order central differences for the viscous terms to compute turbulent channel flows with significant heat transfer, Calhoun and Menon (1996) computed reacting mixing layers using the AUSM flux split scheme, Ansari and Strang (1996) simulated turbulent mixing layers using a second-order accurate unstructured finite volume scheme, and Dailey and Pletcher (1998) used a second-order accurate compressible finite volume formulation to compute the turbulent channel flow with constant high heat flux. This formulation was also used for rib-roughened channel flow by Meng et al. (1999).

To the author's knowledge, no LES work was reported using compressible finite volume formulations for turbulent pipe flow. It is very desirable to develop an efficient compressible finite volume formulation to simulate turbulent pipe flow with significant variable properties resulting from high heating. In this research, the compressible finite volume formulation for planar channel flow developed by Dailey (1997) was extended to enable simulations of turbulent pipe flows with tetrahedral and hexahedral control volumes based on Cartesian coordinates. Time derivative preconditioning was incorporated to allow the computation of low Mach number flows with the compressible formulation. The code was parallelized with the message passing interface (MPI) to reduce wall clock times.

### **1.3.2 Validate a Second-Order Accurate Compressible Finite Volume Formulation for LES**

To validate the second-order accurate compressible finite volume formulation, two incompressible "benchmark" turbulent flows were simulated: turbulent pipe flow and turbulent annular flow with a very small distance between the inner and outer walls compared to the outer radius; i.e.,  $r_i/r_o \approx 1.0$ . The flow in such an annulus closely resembles channel flow because

the effect of curvature are negligible. Thus, the channel flow DNS results reported by Kim (1987) and the experimental results of Niederschulte et al. (1990) could be used for comparison. Grid independence study was conducted for turbulent pipe flow using three different grid resolutions. DNS results obtained by Eggleston et al. (1994) and experiment data from Westerweel (1996) were used to compare with the results of turbulent pipe flow. Results of friction coefficient were compared with various empirical correlations.

### **1.3.3 Validate the Finite Volume Formulation with Very Low Heat Transfer**

Before simulating turbulent pipe flow with significant property variations, it is necessary that both heat and momentum transfer could be predicted very well with very small property variations. Therefore, the LES formulation was examined by simulating a fully developed turbulent pipe flow with very low heat transfer. The property variations were so small that the results could be compared with the passive scalar DNS results obtained by Satake and Kunugi (1999).

### **1.3.4 Study Capability of LES Formulation for the Turbulent Flow in a Vertical Pipe with Significant Variable Properties**

To advance technology in gas-cooled reactor design for improving performance, efficiency, reliability and enhancing safety, it is desirable to understand the complex flows in reactor systems. The general effects of strong heating of a gas flow are variation of the transport properties, reduction of density causing acceleration of the flow in the central core of pipe, and buoyancy effects. It is a challenge to simulate the flows with significant variable properties in computational thermal fluid dynamics, since most turbulence models and DNS and LES simulations utilized the constant property idealization. Although Satake et al. (2000) performed DNS for turbulent pipe flow with strong heating by considering the property variations, the governing equations were not fully compressible; density variations were only included in the continuity equation.

The model used in this research is based on the quasi-developed flow model that was used

successfully for LES in planar channel flow by Dailey and Pletcher (1998). Two assumptions were made in this model, namely that the temperature variations in the streamwise direction were step-periodic for the uniform heat flux case and that the mass flux was streamwise-periodic. The temperature, density and streamwise velocity all varied in the streamwise direction in this model so that we could determine the flow structure at various locations. Three characteristic cases (turbulent, laminarizing and intermediate) with property variations were studied following the experiments reported by Shehata and McEligot (1995). Results were compared with experimental data to validate the simulations.

## 1.4 Dissertation Organization

The governing equations for the LES of compressible turbulent flows are described in detail in Chapter 2. The compressible Navier-Stokes equations are nondimensionalized and Favre filtered. The modeling of the sub-grid scale terms arising due to the filtering operation is discussed. Finally, the integral-vector form amenable to the development of finite volume formulations is presented.

The details of the finite volume formulation are given in Chapter 3. First the dependent variables and computational domain are discussed. This is followed by the presentation of second-order accurate spatial discretization of the inviscid and viscous fluxes for hexahedral and tetrahedral control volumes. The time derivative preconditioning technique is mentioned and implemented. The implicit lower-upper symmetric-Gauss-Seidel (LU-SGS) time integration scheme is extended to solve the equations in a pipe geometry based on Cartesian coordinates. The various boundary conditions used in this work are also discussed.

The results of two benchmark flows are reported in Chapter 4. The incompressible, turbulent annular flow with high ratio of inner radius over outer radius is computed, and the velocity statistics were compared to experimental data and incompressible DNS results of turbulent planar channel flow. The incompressible turbulent pipe flows are simulated with three different grid resolutions, and the statistics results are validated by comparing to experimental and DNS results. The friction coefficients are also compared to various empirical correlations.

The fully developed turbulent pipe flow with very low heat transfer was simulated in Chapter 5. Two thermal wall boundary conditions were investigated. The temperature statistics were compared with the passive scalar DNS results, and friction factors and Nusselt numbers were compared with empirical correlations.

Chapter 6 presents the results of the LES of turbulent flows in a vertical pipe with significant property variations. The buoyancy forces are taken into account in all simulations. Three characteristic cases are studied, and the statistical results are compared with corresponding experimental results. Comparisons are also made to empirical correlations for the friction coefficients and Nusselt numbers.

The conclusions of this research, as well as recommendations for future work, are presented in Chapter 7.

## CHAPTER 2. GOVERNING EQUATIONS

In this chapter the non-dimensional compressible Navier-Stokes (NS) equations used for the current work are described in detail along with the derivation of the filtered set of equations specific to LES. The equations are described for a general three-dimensional problem based on Cartesian coordinates and recast in integral-vector form so that they can be numerically solved with a finite volume method that is presented in Chapter 3.

### 2.1 Compressible Navier-Stokes Equations

The fundamental equations of fluid dynamics are based on the conservation laws for mass, momentum, and energy. In Cartesian tensor notation they can be written as follows with the superscript ‘\*’ denoting dimensional quantities,

$$\frac{\partial \rho^*}{\partial t^*} + \frac{\partial(\rho^* u_j^*)}{\partial x_j^*} = 0 \quad (2.1)$$

$$\frac{\partial(\rho^* u_i^*)}{\partial t^*} + \frac{\partial(\rho^* u_i^* u_j^*)}{\partial x_j^*} = -\frac{\partial p^*}{\partial x_i^*} + \frac{\partial \sigma_{ij}^*}{\partial x_j^*} \quad (2.2)$$

$$\frac{\partial(\rho^* E^*)}{\partial t^*} + \frac{\partial(\rho^* E^* u_j^*)}{\partial x_j^*} = -\frac{\partial(p^* u_j^*)}{\partial x_j^*} - \frac{\partial q_j^*}{\partial x_j^*} + \frac{\partial(\sigma_{ij}^* u_i^*)}{\partial x_j^*} \quad (2.3)$$

where the total specific energy is  $E^* = e^* + \frac{1}{2} u_j^* u_j^*$ . The viscous stress tensor is given as

$$\sigma_{ij}^* = \mu^* \left( \frac{\partial u_i^*}{\partial x_j^*} + \frac{\partial u_j^*}{\partial x_i^*} \right) + \lambda^* \frac{\partial u_k^*}{\partial x_k^*} \delta_{ij} \quad (2.4)$$

where  $\delta_{ij}$  is the Kronecker delta function,  $\mu^*$  is the dynamic viscosity, and  $\lambda^*$  is the bulk viscosity equal to  $-\frac{2}{3}\mu^*$  by using Stokes hypothesis,  $\lambda^* + \frac{2}{3}\mu^* = 0$ . Fourier’s law for heat transfer by conduction is assumed and the heat flux vector is expressed as

$$q_j^* = -k^* \frac{\partial T^*}{\partial x_j^*} \quad (2.5)$$

where  $k^*$  is the thermal diffusion coefficient.

In order to close the system of fluid dynamic equations, an additional equation relating the thermodynamic variables ( $p^*, \rho^*, T^*, e^*, h^*$ ) is needed. The ideal gas assumption was applied in this research and the equation of state is

$$p^* = \rho^* R^* T^* \quad (2.6)$$

where  $R^*$  is the dimensional gas constant.

The properties  $\mu^*$  and  $k^*$  are functions of temperature. In this research, the non-dimensional coefficients of viscosity and thermal conductivity were evaluated using the power-law form of Sutherland's formula (Schlichting, 1979).

$$\frac{\mu^*}{\mu_{ref}} = \left( \frac{T^*}{T_{ref}} \right)^n \quad (2.7)$$

$$\frac{k^*}{k_{ref}} = \left( \frac{T^*}{T_{ref}} \right)^n \quad (2.8)$$

where  $n$  was assumed to be 0.71 and the specific heats,  $C_p^*$  and  $C_v^*$ , were treated as constants for the temperature range under consideration.

## 2.2 Non-dimensionalization

The above set of equations have been non-dimensionalized with respect to appropriate dimensional reference quantities as described below,

$$\begin{aligned} x_i &= \frac{x_i^*}{L_{ref}} & u_i &= \frac{u_i^*}{U_{ref}} & t &= \frac{t^*}{(L_{ref}/U_{ref})} \\ \rho &= \frac{\rho^*}{\rho_{ref}} & p &= \frac{p^*}{\rho_{ref} U_{ref}^2} & T &= \frac{T^*}{T_{ref}} & e &= \frac{e^*}{U_{ref}^2} \\ \mu &= \frac{\mu^*}{\mu_{ref}} & k &= \frac{k^*}{k_{ref}} & C_p &= \frac{c_p^*}{(U_{ref}^2/T_{ref})} \\ C_v &= \frac{c_v^*}{(U_{ref}^2/T_{ref})} & R &= \frac{R^*}{(U_{ref}^2/T_{ref})} = \frac{1}{\gamma M_{ref}^2} \end{aligned} \quad (2.9)$$

where  $L_{ref}$ ,  $U_{ref}$ ,  $T_{ref}$  and  $\rho_{ref}$  are the reference length, velocity, temperature and density, respectively. The reference Mach number is  $M_{ref} = \frac{U_{ref}}{\sqrt{\gamma R^* T_{ref}}}$ .

Using the above definitions, the following non-dimensional form of the NS equations are obtained,

$$\frac{\partial \rho}{\partial t} + \frac{\partial(\rho u_j)}{\partial x_j} = 0 \quad (2.10)$$

$$\frac{\partial \rho u_i}{\partial t} + \frac{\partial(\rho u_i u_j)}{\partial x_j} = -\frac{\partial p}{\partial x_i} + \frac{\partial \sigma_{ij}}{\partial x_j} \quad (2.11)$$

$$\frac{\partial(\rho E)}{\partial t} + \frac{\partial(\rho E u_j)}{\partial x_j} = -\frac{\partial(p u_j)}{\partial x_j} - \frac{\partial q_j}{\partial x_j} + \frac{\partial(\sigma_{ij} u_i)}{\partial x_j} \quad (2.12)$$

The non-dimensional viscous stress tensor and heat flux vector are given as

$$\sigma_{ij} = \frac{2\mu}{Re_{ref}} \left( S_{ij} - \frac{1}{3} S_{kk} \delta_{ij} \right) \quad (2.13)$$

$$q_j = -\frac{c_p \mu}{Pr Re_{ref}} \frac{\partial T}{\partial x_j} \quad (2.14)$$

where the strain rate tensor is

$$S_{ij} = \frac{1}{2} \left( \frac{\partial u_i}{\partial x_j} + \frac{\partial u_j}{\partial x_i} \right) \quad (2.15)$$

The Reynolds number based on reference quantities is  $Re_{ref} = \rho_{ref} U_{ref} L_{ref} / \mu_{ref}$  and the molecular Prandtl number is  $Pr = \mu^* C_p^* / k^*$ . In this work, the molecular Prandtl number was assumed to be constant at 0.71.

The ideal gas law in non-dimensional form becomes,

$$p = \rho R T = \frac{\rho T}{\gamma M_{ref}^2} = (\gamma - 1) \rho e \quad (2.16)$$

### 2.3 Filtering

The idea of large eddy simulation is to solve for the larger scales of motion of the turbulence while modeling the smaller ones. It is essential to define a field in which only large scale components of the total field exist. This is best done by filtering (Leonard, 1974). This filter can be written in terms of a convolution integral as

$$\bar{f}(\vec{x}, t) = \int_D G(\vec{x}, \vec{\xi}) f(\vec{\xi}, t) d\vec{\xi} \quad (2.17)$$

where  $D$  is the entire domain,  $G$  is a filter function that determines the size and structure of the small scales. As a result of this operation the flow variable can be viewed as being

decomposed into two components.

$$f = \bar{f} + f' \quad (2.18)$$

where  $\bar{f}$  is the large scale, or resolved component, and  $f'$  is the small-scale, unresolved, or subgrid scale component.

Filtering can be best understood in wave or Fourier space. Any signal can be broken down into its frequency components by means of transforming it into Fourier space. Filtering actually means setting the Fourier coefficients of scales smaller than a cut-off scale to be zero. The most commonly-used filter functions applied in LES are the sharp Fourier cut-off filter, box or top-hat filter and Gaussian filter.

### 1. Sharp Fourier cut-off filter:

The sharp cut-off filter is defined in wave space as

$$G(\vec{k}) = \begin{cases} 0 & |k_i| > k_c \\ 1 & |k_i| \leq k_c \end{cases} \quad (2.19)$$

where  $\vec{k}$  is the wave vector, and  $k_c$  is the cut-off wave number. This filter eliminates all of the coefficients belonging to wave numbers above a particular cut-off wave number. It is used often with spectral methods; however, it is difficult to apply to inhomogeneous flows. Also, because it is not easily defined in physical space, it is hard to implement for finite-difference and finite-volume methods.

### 2. Gaussian filter:

$$G(\vec{x}, \vec{\xi}) = \left[ \frac{\sqrt{c/\pi}}{\Delta} \right]^n \exp \left\{ - \left[ \frac{\sqrt{c}}{\Delta} \right]^n (\vec{x} - \vec{\xi})^2 \right\} \quad (2.20)$$

where  $\Delta$  is the filter width,  $c$  is a constant and  $n$  is the number of dimensions to be filtered. The Gaussian filter has the advantage of being smooth and infinitely differentiable in both physical and Fourier space. In wavenumber space, it is

$$G(\vec{k}) = \exp \left[ \frac{-\Delta^2 k^2}{4c} \right] \quad (2.21)$$

### 3. Box filter:

The box, or top-hat filter is given in physical space as,

$$G(\vec{x}, \vec{\xi}) = \begin{cases} 1/\Delta^3 & |x_i - \xi_i| \leq \Delta/2 \\ 0 & |x_i - \xi_i| > \Delta/2 \end{cases} \quad (i = 1, 2, 3) \quad (2.22)$$

where  $\Delta$  is the filter width. The filter is an average over a volume and it is a natural choice when finite-volume or finite-difference methods are used.

The Gaussian and the top-hat filters give similar results; they both smooth the large-scale fluctuations as well as the small-scale ones, while the sharp Fourier cut-off filter only affects the scales below the cut-off wavenumber.

## 2.4 Favre Filtered Governing Equations

The governing equations for large eddy simulation are obtained by filtering the compressible Navier-Stokes equations to separate the effects of the large-scale and small-scale motions. It can be shown that in the filtering operation, Eq. 2.17, if  $G$  is a function of  $\vec{x} - \vec{\xi}$  only and filtering width is constant, then differentiation and the filtering operation commute (Leonard, 1974) as

$$\overline{\frac{\partial f}{\partial t}} = \frac{\partial \bar{f}}{\partial t} \quad ; \quad \overline{\frac{\partial f}{\partial x}} = \frac{\partial \bar{f}}{\partial x} \quad (2.23)$$

The filtering operation does not generally commute with the differentiation operation for LES of inhomogeneous turbulent flow with a variable filter width if commutation is assumed, the error is second-order of filter width (Ghosal and Moin, 1995). In this research, since the grid spacing was the same order as the filter width and a second order numerical scheme was used, the finite difference error was then the same order as the commutation error. Therefore, the filtering operation in this work can be considered to commute with the differentiation operation within the accuracy of numerical approximation. The basic equations for LES based on this grid filter have already been successfully used in channel flows.

The filtering operation is applied to the nondimensional continuity and momentum equations (Eq. 2.10 and Eq. 2.11 respectively) yielding

$$\frac{\partial \bar{\rho}}{\partial t} + \frac{\partial (\bar{\rho} u_j)}{\partial x_j} = 0 \quad (2.24)$$

$$\frac{\partial(\overline{\rho u_i})}{\partial t} + \frac{\partial(\overline{\rho u_i u_j})}{\partial x_j} = -\frac{\partial \bar{p}}{\partial x_i} + \frac{\partial \bar{\sigma}_{ij}}{\partial x_j} \quad (2.25)$$

where

$$\bar{\sigma}_{ij} = \frac{2\mu}{Re_{ref}} \left( S_{ij} - \frac{1}{3} S_{kk} \delta_{ij} \right) \quad (2.26)$$

We will not directly filter the non-dimensional total energy equation, Eq. 2.12, in this work. The conservation law form of the filtered energy equation in terms of the resolved total energy is derived following Vreman et al. (1995) for the present work. First an alternate form of the energy equation, in which the mechanical energy contributions are removed from the total energy equation, is obtained by manipulation of Eqs. 2.11 and 2.12 (Currie, 1974) as

$$\frac{\partial(\rho c_v T)}{\partial t} + \frac{\partial(\rho c_v T u_j)}{\partial x_j} = -p \frac{\partial u_j}{\partial x_j} - \frac{\partial q_j}{\partial x_j} + \sigma_{ij} \frac{\partial u_i}{\partial x_j} \quad (2.27)$$

Applying the filtering operation to this thermal energy equation leads to

$$\frac{\partial(\overline{\rho c_v T})}{\partial t} + \frac{\partial(\overline{\rho c_v T u_j})}{\partial x_j} = -\overline{p \frac{\partial u_j}{\partial x_j}} - \frac{\partial \bar{q}_j}{\partial x_j} + \overline{\sigma_{ij} \frac{\partial u_i}{\partial x_j}} \quad (2.28)$$

where

$$\bar{q}_j = -\frac{c_p \mu}{Re_{ref} Pr} \frac{\partial \bar{T}}{\partial x_j} \quad (2.29)$$

and the equation of state becomes

$$\bar{p} = R \bar{\rho} \bar{T} \quad (2.30)$$

In the above filtered compressible Navier-stokes equations, there is one more unknown, the density,  $\rho$ , than in the filtered incompressible Navier-stokes equations. As a result, the filtered convective terms contain a triple product of the unknown variables. For example, the SGS Reynolds stress becomes  $\overline{\rho' u' v'}$ . So tremendous complexities would be introduced into the SGS modeling if we use the above filter operation. To simplify the filtered equations for compressible flow, Favre filtering (Favre, 1983) is further applied to give

$$\tilde{f} = \frac{\overline{\rho f}}{\bar{\rho}} \quad (2.31)$$

and hence  $\overline{\rho f} = \bar{\rho} \tilde{f}$ , where  $f$  is a general flow variable such as the velocity and temperature but not the density and pressure. Now, the variables can be decomposed in two ways,

$$f = \bar{f} + f' \quad (2.32)$$

$$f = \bar{f} + f'' \quad (2.33)$$

where  $\bar{f}$  and  $\tilde{f}$  are the resolved components and  $f'$  and  $f''$  are the unresolved components. As the result of the Favre filter,

$$\overline{\rho u_i} = \bar{\rho} \tilde{u}_i \quad ; \quad \overline{\rho u_i u_j} = \bar{\rho} \tilde{u}_i \tilde{u}_j \quad ; \quad \overline{\rho u_i T} = \bar{\rho} \tilde{u}_i \tilde{T} \quad (2.34)$$

Consequently, the Favre filtered governing equations are

$$\frac{\partial \bar{\rho}}{\partial t} + \frac{\partial(\bar{\rho} \tilde{u}_j)}{\partial x_j} = 0 \quad (2.35)$$

$$\frac{\partial(\bar{\rho} \tilde{u}_i)}{\partial t} + \frac{\partial(\bar{\rho} \tilde{u}_i \tilde{u}_j)}{\partial x_j} = -\frac{\partial \bar{p}}{\partial x_i} + \frac{\partial \bar{\sigma}_{ij}}{\partial x_j} - \frac{\partial \tau_{ij}}{\partial x_j} \quad (2.36)$$

$$\frac{\partial(\bar{\rho} c_v \tilde{T})}{\partial t} + \frac{\partial(\bar{\rho} c_v \tilde{T} \tilde{u}_j)}{\partial x_j} = -\frac{\partial \bar{q}_j}{\partial x_j} - \frac{\partial Q_j}{\partial x_j} - p \frac{\partial \tilde{u}_j}{\partial x_j} + \overline{\sigma_{ij} \frac{\partial u_i}{\partial x_j}} \quad (2.37)$$

and the equation of state is

$$\bar{p} = R \bar{\rho} \tilde{T} \quad (2.38)$$

The filtered dimensionless viscous stress and heat flux vector are approximated by assuming that the correlations between the fluid properties and the derivatives of the velocity or temperature are weak (Cebeci and Smith, 1974). The approximations are

$$\bar{\sigma}_{ij} \approx \hat{\sigma}_{ij} = \frac{2\bar{\mu}}{Re_{ref}} \left( \tilde{S}_{ij} - \frac{1}{3} \tilde{S}_{kk} \delta_{ij} \right) \quad (2.39)$$

and

$$\bar{q}_j \approx \hat{q}_j = -\frac{c_p \bar{\mu}}{Re_{ref} Pr} \frac{\partial \tilde{T}}{\partial x_j} \quad (2.40)$$

where the strain rate tensor is

$$\tilde{S}_{ij} = \frac{1}{2} \left( \frac{\partial \tilde{u}_i}{\partial x_j} + \frac{\partial \tilde{u}_j}{\partial x_i} \right) \quad (2.41)$$

and  $\bar{\mu} = \bar{\mu}(\tilde{T})$  is given by the power law stated previously.

The effect of the small-scale motions are present in the above equations through the subgrid scale (SGS) stress tensor in the Favre filtered momentum equation,

$$\tau_{ij} = \bar{\rho} (\tilde{u}_i \tilde{u}_j - \tilde{u}_i \tilde{u}_j) \quad (2.42)$$

and the SGS terms, the last three terms in the right hand side of Eq. 2.37, in the thermal energy equation. The SGS heat flux is

$$Q_j = \bar{\rho}c_v(\widetilde{T}u_j - \tilde{T}\tilde{u}_j) \quad (2.43)$$

The filtered thermal energy equation, Eq. 2.37, is not in conservation law form and thus not directly amenable to finite volume methods. A filtered energy equation in conservation law form is derived for the resolved total energy following Vreman et al. (1995) so that the finite volume methods can be used in this work. The resolved total energy is defined as

$$\hat{E} = \bar{e} + \frac{1}{2}\tilde{u}_i\tilde{u}_i \quad (2.44)$$

To obtain the equation for  $\bar{\rho}\hat{E}$ , the Favre filtered momentum equation, Eq. 2.36, is expanded as

$$\bar{\rho}\frac{\partial\tilde{u}_i}{\partial t} + \tilde{u}_i\left[\frac{\partial\bar{\rho}}{\partial t} + \frac{\partial(\bar{\rho}\tilde{u}_j)}{\partial x_j}\right] + \bar{\rho}\tilde{u}_j\frac{\partial\tilde{u}_i}{\partial x_j} = -\frac{\partial\bar{p}}{\partial x_i} + \frac{\partial\bar{\sigma}_{ij}}{\partial x_j} - \frac{\partial\tau_{ij}}{\partial x_j} \quad (2.45)$$

and the second term of the above equation vanishes due to the Favre filtered continuity equation. Eq. 2.45 is multiplied by  $\tilde{u}_i$  and added to the filtered thermal energy equation, Eq. 2.37, giving

$$\begin{aligned} & \frac{\partial(\bar{\rho}c_v\tilde{T})}{\partial t} + \frac{\partial(\bar{\rho}c_v\tilde{T}\tilde{u}_j)}{\partial x_j} + \bar{\rho}\tilde{u}_i\frac{\partial\tilde{u}_i}{\partial t} + \bar{\rho}\tilde{u}_i\tilde{u}_j\frac{\partial\tilde{u}_i}{\partial x_j} = \\ & -\overline{p\frac{\partial u_j}{\partial x_j}} - \tilde{u}_i\frac{\partial\bar{p}}{\partial x_i} + \overline{\sigma_{ij}\frac{\partial u_i}{\partial x_j}} + \tilde{u}_i\frac{\partial\hat{\sigma}_{ij}}{\partial x_j} - \tilde{u}_i\frac{\partial\tau_{ij}}{\partial x_j} - \frac{\partial\hat{q}_j}{\partial x_j} - \frac{\partial Q_j}{\partial x_j} \end{aligned} \quad (2.46)$$

where  $\hat{\sigma}_{ij}$  and  $\hat{q}_j$  are the approximation of  $\bar{\sigma}_{ij}$  and  $\bar{q}_j$  respectively. The filtered continuity equation, Eq. 2.35, is multiplied by  $\frac{1}{2}\tilde{u}_i\tilde{u}_i$  and added to Eq. 2.46, giving

$$\begin{aligned} & \frac{\partial(\bar{\rho}c_v\tilde{T})}{\partial t} + \bar{\rho}\tilde{u}_i\frac{\partial\tilde{u}_i}{\partial t} + \frac{1}{2}\tilde{u}_i\tilde{u}_i\frac{\partial\bar{\rho}}{\partial t} + \frac{\partial(\bar{\rho}c_v\tilde{T}\tilde{u}_j)}{\partial x_j} + \bar{\rho}\tilde{u}_i\tilde{u}_j\frac{\partial\tilde{u}_i}{\partial x_j} + \frac{1}{2}\tilde{u}_i\tilde{u}_i\frac{\partial(\bar{\rho}\tilde{u}_j)}{\partial x_j} = \\ & -\overline{p\frac{\partial u_j}{\partial x_j}} - \tilde{u}_i\frac{\partial\bar{p}}{\partial x_i} + \overline{\sigma_{ij}\frac{\partial u_i}{\partial x_j}} + \tilde{u}_i\frac{\partial\hat{\sigma}_{ij}}{\partial x_j} - \tilde{u}_i\frac{\partial\tau_{ij}}{\partial x_j} - \frac{\partial\hat{q}_j}{\partial x_j} - \frac{\partial Q_j}{\partial x_j} \end{aligned} \quad (2.47)$$

The first three terms and last three terms of Eq 2.47 are combined, giving

$$\frac{\partial(\bar{\rho}\hat{E})}{\partial t} + \frac{\partial(\bar{\rho}\hat{E}\tilde{u}_j)}{\partial x_j} = -\overline{p\frac{\partial u_j}{\partial x_j}} - \tilde{u}_i\frac{\partial\bar{p}}{\partial x_i} + \overline{\sigma_{ij}\frac{\partial u_i}{\partial x_j}} + \tilde{u}_i\frac{\partial\hat{\sigma}_{ij}}{\partial x_j} - \tilde{u}_i\frac{\partial\tau_{ij}}{\partial x_j} - \frac{\partial\hat{q}_j}{\partial x_j} - \frac{\partial Q_j}{\partial x_j} \quad (2.48)$$

The subgrid scale contributions are defined as

$$Q_j = \bar{\rho}c_v(\widetilde{T}u_j - \tilde{T}\tilde{u}_j) = \frac{\overline{pu_j} - \bar{p}\tilde{u}_j}{\gamma - 1} \quad (2.49)$$

$$\alpha = \tilde{u}_i \frac{\partial \tau_{ij}}{\partial x_j} \quad (2.50)$$

$$\pi = \overline{p \frac{\partial u_j}{\partial x_j}} - \bar{p} \frac{\partial \tilde{u}_j}{\partial x_j} \quad (2.51)$$

$$\varepsilon = \overline{\sigma_{ij} \frac{\partial u_i}{\partial x_j}} - \hat{\sigma}_{ij} \frac{\partial \tilde{u}_j}{\partial x_j} \quad (2.52)$$

Consequently, the Favre filtered energy equation for the resolved total energy is given by

$$\frac{\partial(\bar{\rho}\hat{E})}{\partial t} + \frac{\partial[(\bar{\rho}\hat{E} + \bar{p})\tilde{u}_j]}{\partial x_j} = \frac{\partial(\tilde{u}_i\hat{\sigma}_{ij})}{\partial x_j} - \frac{\partial\hat{q}_j}{\partial x_j} - \frac{\partial Q_j}{\partial x_j} - \alpha - \pi - \varepsilon \quad (2.53)$$

For the present work,  $\alpha$ ,  $\pi$  and  $\varepsilon$  were neglected since only low Mach number flows were considered, which is an appropriate assumption for Mach numbers below 0.2 (Vreman et al. 1995).

As expected, the unresolved SGS stress tensor  $\tau_{ij}$  and the SGS heat flux  $Q_j$  need to be modeled in order to close the system of equations. The quantity  $\tau_{ij}$  represents the effect of the subgrid scale velocity component on the evolution of the large-scale motion. Traditionally,  $\tau_{ij}$  has been split into 3 components known as the Leonard stress,  $l_{ij}$ , (Leonard 1974), cross SGS stress,  $c_{ij}$ , and the Reynolds SGS stress,  $r_{ij}$ ,

$$\tau_{ij} = l_{ij} + c_{ij} + r_{ij} \quad (2.54)$$

where,

$$\begin{aligned} l_{ij} &= -\bar{\rho}(\widetilde{\tilde{u}_i\tilde{u}_j} - \tilde{u}_i\tilde{u}_j) \\ c_{ij} &= -\bar{\rho}(\widetilde{\tilde{u}_i u'_j} + \widetilde{u'_i\tilde{u}_j}) \\ r_{ij} &= -\bar{\rho}(\widetilde{u'_i u'_j}) \end{aligned} \quad (2.55)$$

The Leonard stress can be computed explicitly from the resolved velocity field,  $\tilde{u}$ , and represents the interaction of two resolved scale eddies to produce small scale turbulence; it is also called the outscatter term. The cross SGS stress represents the interaction between large scale eddies and small scale eddies; it can transfer energy in either direction from the large scales to the small ones or from the small scales to the large ones, but totally transfers energy from the large scales to the small ones. The Reynolds SGS stress, also called backscatter term,

represents the interaction between two subgrid scales to produce a large scale eddy; it transfers energy from the small scales to the large ones. In the past, the three terms have been modeled separately; however, Speziale (1985) has shown that modeling the three terms together would satisfy the Galilean invariance property that all physical laws should be invariant with respect to an inertial coordinate transformation. Consequently, it has become common to lump and model all three terms together.

## 2.5 Subgrid Scale Models

In large eddy simulation (LES), the subgrid scales need to be modeled and the models are called subgrid scale models. This is analogous to the turbulence modeling for the Reynolds averaged Navier-Stokes (RANS) equations, but maybe more complicated physically due to an important difference; filtering a field a second time does not reproduce the original filtered field. SGS models should be simpler and more universal than RANS models since the small scales are assumed to be more isotropic and more universal for different flows than the large scales.

It has frequently been suggested that the key role of the subgrid scale model is to provide an exchange of energy between large scales and small scales at roughly the correct rate (Rogallo & Moin 1984). Instantaneously, the energy can be transferred either way from large eddies to small ones or from small eddies to large ones. The reverse transfer is termed “backscatter” (Piomelli et al. 1991). However, on average, energy is usually assumed to be transferred from large scales to the subgrid scales which corresponds to the classical concept of an energy cascade. Based on this concept, the subgrid scales essentially act as a sink of energy and maybe modeled by the dissipative eddy viscosity models. However, Piomelli et al. (1991) found that the eddy viscosity models yield to inaccurate prediction for the transitional channel flow due to the reverse energy transfer, while for fully developed channel flow the eddy viscosity models were successful. Härtel and Kleiser (1997) also found that an inverse cascade of turbulent energy occurs in the buffer layer by analyzing DNS data of turbulent channel and pipe flow. In the current work, the flows are assumed to be fully developed, so only eddy viscosity models

are used. A recent review of SGS modeling can be found in Meneveau and Katz (2000).

### 2.5.1 Eddy Viscosity Model

Eddy viscosity, or gradient-diffusion methodology is the most widely used SGS modeling approach; it is similar to the Boussinesq approximation for RANS turbulence models. By assuming that the anisotropic part of the SGS stress tensor is proportional to the rate of strain tensor, the SGS stress rate tensor is given as

$$\tau_{ij} - \frac{1}{3}q^2\delta_{ij} = -2\mu_t \left( \tilde{S}_{ij} - \frac{1}{3}\tilde{S}_{kk}\delta_{ij} \right) \quad (2.56)$$

where  $q^2 = \tau_{kk}$  is the isotropic part of  $\tau_{ij}$ . The turbulent, or eddy viscosity is defined as

$$\mu_t = C_d \bar{\rho} \Delta^2 |\tilde{S}| \quad (2.57)$$

where the magnitude of the strain rate tensor is

$$|\tilde{S}| = \left( 2\tilde{S}_{ij}\tilde{S}_{ij} \right)^{1/2} \quad (2.58)$$

The filter width,  $\Delta$ , is typically given by  $\Delta = (\Delta_x \Delta_y \Delta_z)^{1/3}$ , where  $\Delta_x$ ,  $\Delta_y$  and  $\Delta_z$  are the control volume dimensions in the  $x$ ,  $y$  and  $z$  directions, respectively. In this research,  $V^{1/3}$  is used as the filter width due to the anisotropic grids, where  $V$  is the volume of the control volume.  $C_d$  is a coefficient to be determined.

### 2.5.2 Smagorinsky SGS model

The eddy viscosity model is further classified depending on the method for determining the anisotropic coefficient,  $C_d$ . The Smagorinsky SGS model was proposed by Smagorinsky as far back as 1963. This model is based on the equilibrium assumption that the small scales dissipate all the energy they receive from the large scales and are in equilibrium. The coefficient,  $C_d$  is assumed to be a constant and can be obtained from isotropic turbulence decay (Lily, 1967).

Although the Smagorinsky SGS model is widely used in LES, it has the following limitations (Moin et al, 1991).

1. The optimal model constant must be changed in different flows.

The coefficient.  $C_d$  can vary with different flow regimes, grid scales and other factors. For instance, Deardorff (1970) found 0.1 to be the optimal value for the plane channel flow and Lily (Germano et al. 1991) calculated the coefficient as 0.23 in homogeneous isotropic turbulence.

2. The model does not have the correct limiting behavior near the wall.
3. The model does not vanish in laminar flow, and it is demonstrated to be too dissipative in the laminar/turbulent transition region.

For instance, when the resolved flow is in the laminar region, the classical  $C_d$  overestimated the dissipation and often prevents transition to turbulence. (Piomelli & Zang 1991).

4. The model does not account for backscatter of energy from small scales to large scales, which has been shown to be important in the transition regime.
5. Compressibility effects are not included in the model.

Consequently, empirical wall damping functions are needed to make the Smagorinsky SGS model appropriate in wall bounded flows (Moin and Kim, 1982; Piomelli, Moin, and Ferziger, 1988; Ciofalo and Collins, 1992). For example, Ciofalo and Collins (1992) proposed

$$\tau_{ij} - \frac{1}{3}q^2\delta_{ij} = -2\mu_t \left( \tilde{S}_{ij} - \frac{1}{3}\tilde{S}_{kk}\delta_{ij} \right) \quad (2.59)$$

$$\mu_t = C_d \bar{\rho} D^2 \Delta^2 |\tilde{S}| \quad (2.60)$$

where the Van Driest damping function is defined as

$$D = 1 - \exp\left(\frac{-y^+}{A^+}\right) \quad (2.61)$$

The constant  $A^+$  is taken as 25;  $y^+$ , which is expressed in wall units, is the distance to the nearest wall. The improved Smagorinsky SGS model has been successfully used for channel flow simulations (Dailey, 1997).

### 2.5.3 Dynamic SGS model

The dynamic model (Germano et al., 1991) is also an eddy viscosity model based on the scale-similarity ideas. It overcomes many deficiencies of Smagorinsky SGS model. For this model, the coefficient,  $C_d$ , is calculated “dynamically” by using spectral information contained in the resolved field through two different scales. Thus, the  $C_d$  is a function of space and time. The coefficient can be negative in some regions and thus hopefully account for the backscatter of energy to the large scales. Also, the SGS stress asymptotically approaches to zero near solid walls and in laminar flow without the ad hoc damping function. The dynamic model proposed for compressible turbulence by Moin et al. (1991) and recommended by Lilly (1992) not only allows the value of the eddy viscosity to vary, but also allows the eddy thermal diffusivity to be calculated dynamically. This model has been followed for this work.

#### 2.5.3.1 SGS stress tensor

For the dynamic model, a “test filter” with a larger filter width than the resolved grid filter is introduced to bring spectral information from the resolved field. The test filter width,  $\hat{\Delta}$ , is defined in the same way as the grid filter width. Using the Boussinesq assumption, the SGS stress tensor based on the grid filter can be modeled as

$$\tau_{ij} - \frac{1}{3}\tau_{kk}\delta_{ij} = -2C_d\bar{\rho}\Delta^2|\tilde{S}| \left( \tilde{S}_{ij} - \frac{1}{3}\tilde{S}_{kk}\delta_{ij} \right) \quad (2.62)$$

where the Favre filtered SGS stress expression is

$$\begin{aligned} \tau_{ij} &= \bar{\rho}(\widetilde{u_i u_j} - \tilde{u}_i \tilde{u}_j) \\ &= \overline{\rho u_i u_j} - \frac{\overline{\rho u_i} \overline{\rho u_j}}{\bar{\rho}} \end{aligned} \quad (2.63)$$

The test filtered stress  $T_{ij}$  is defined by direct analogy to the SGS stresses  $\tau_{ij}$  as

$$T_{ij} = \overline{\widehat{\rho u_i u_j}} - \frac{\overline{\widehat{\rho u_i}} \overline{\widehat{\rho u_j}}}{\widehat{\rho}} \quad (2.64)$$

and is modeled as

$$T_{ij} - \frac{1}{3}T_{kk}\delta_{ij} = -2C_d\hat{\rho}\hat{\Delta}^2|\hat{S}| \left( \hat{S}_{ij} - \frac{1}{3}\hat{S}_{kk}\delta_{ij} \right) \quad (2.65)$$

For incompressible flow, the isotropic part of the SGS stress tensors,  $\tau_{kk}$  and  $T_{kk}$ , can be combined with the pressure and no model needed for them. but for compressible flow, they have to be modeled. Yoshizawa (1986) proposed a model as

$$\tau_{kk} = 2C_I \bar{\rho} \Delta^2 |\tilde{S}|^2 \quad (2.66)$$

$$T_{kk} = 2C_I \hat{\rho} \hat{\Delta}_2 |\hat{S}|^2 \quad (2.67)$$

Using Germano's identity,  $\tau_{ij}$  and  $T_{ij}$  are related in the Leonard stresses,  $L_{ij}$ , giving

$$\begin{aligned} L_{ij} &= T_{ij} - \hat{\tau}_{ij} \\ &= \widehat{\rho \tilde{u}_i \tilde{u}_j} - \frac{\widehat{\rho \tilde{u}_i \rho \tilde{u}_j}}{\hat{\rho}} \end{aligned} \quad (2.68)$$

To compute the coefficient  $C_I$ , Eq. 2.66 and Eq. 2.67 are substituted into Eq. 2.68, giving

$$L_{kk} = \widehat{\rho \tilde{u}_k \tilde{u}_k} - \frac{\widehat{\rho \tilde{u}_k \rho \tilde{u}_k}}{\hat{\rho}} = 2C_I (\hat{\rho} \hat{\Delta}^2 |\hat{S}|^2 - \Delta^2 (\bar{\rho} |\tilde{S}|^2)) \quad (2.69)$$

and thus  $C_I$  can be determined as

$$C_I = \frac{L_{kk}}{2\hat{\rho} \hat{\Delta}^2 |\hat{S}|^2 - 2\Delta^2 (\bar{\rho} |\tilde{S}|^2)} \quad (2.70)$$

Many researchers neglect the isotropic part of SGS stress tensor on the grounds that it is negligible compared to the thermodynamic pressure (Moin et al. 1991; Spyropoulos and Blaisdell, 1995). Also Vreman et al. (1995) found that the calculation was unstable if the isotropic part of SGS stress tensor was not neglected. Dailey (1997) also observed the instability. Consequently, in the present work,  $\tau_{kk}$  was neglected and  $C_I$  was set to zero.

Neglecting  $\tau_{kk}$  and  $T_{kk}$  simplified the calculations of coefficient  $C_d$ . Substituting Eq. 2.62 and Eq. ?? into Eq. 2.68 yields

$$L_{ij} = C_d \left[ -2\hat{\rho} \hat{\Delta}^2 |\hat{S}| (\hat{S}_{ij} - \frac{1}{3} \hat{S}_{kk} \delta_{ij}) + 2\Delta^2 \bar{\rho} |\tilde{S}| (\tilde{S}_{ij} - \frac{1}{3} \tilde{S}_{kk} \delta_{ij}) \right] = C_d M_{ij} \quad (2.71)$$

Using the least squares approach (Lilly,1992) and after the appropriate spatial averaging, the coefficient  $C_d$  is determined as

$$C_d = \frac{\langle L_{ij} M_{ij} \rangle}{\langle M_{kl} M_{kl} \rangle} \quad (2.72)$$

where  $\langle \rangle$  denotes to a spatial averaging procedure along the homogeneous directions of the flow. This is necessary to make the SGS coefficients well conditioned.

### 2.5.3.2 SGS heat flux vector

A procedure similar to the modeling of SGS stress tensor is followed to represent the SGS heat flux vector. Considering the modeling for the eddy diffusivity SGS model, it follows that the subgrid scale heat flux vector might be modeled as

$$\begin{aligned} Q_j &= -\frac{c_p \mu_t}{Pr_t} \frac{\partial \tilde{T}}{\partial x_j} \\ &= -\frac{c_p C_d \bar{\rho} \Delta^2 |\tilde{S}|}{Pr_t} \frac{\partial \tilde{T}}{\partial x_j} \end{aligned} \quad (2.73)$$

where the Favre filtered heat flux vector is given as

$$\begin{aligned} Q_j &= \bar{\rho} c_v (\widehat{u_j T} - \tilde{u}_j \tilde{T}) \\ &= c_v \left( \overline{\rho u_j T} - \frac{\overline{\rho u_j \rho T}}{\bar{\rho}} \right) \end{aligned} \quad (2.74)$$

and  $Pr_t$  is the turbulent Prandtl number to be determined dynamically.

Similarly, the test filtered heat flux vector  $Q_{tj}$  is defined as

$$Q_{tj} = c_v \left( \widehat{\rho u_j T} - \frac{\widehat{\rho u_j \rho T}}{\hat{\rho}} \right) \quad (2.75)$$

and modeled as

$$Q_{tj} = -\frac{c_p C_d \hat{\rho} \hat{\Delta}^2 |\hat{S}|}{Pr_t} \frac{\partial \hat{T}}{\partial x_j} \quad (2.76)$$

The algebraic identity relating the two heat fluxes is

$$\begin{aligned} H_j &= Q_{tj} - \hat{Q}_j \\ &= c_v \left( \widehat{\rho \tilde{u}_j \tilde{T}} - \frac{\widehat{\rho \tilde{u}_j \rho \tilde{T}}}{\hat{\rho}} \right) \end{aligned} \quad (2.77)$$

Substituting Eq. 2.73 and Eq. 2.76 into Eq. 2.77 we obtain

$$H_j = -\frac{c_p C_d}{Pr_t} F_j \quad (2.78)$$

where,

$$F_j = \hat{\rho} \hat{\Delta}^2 |\hat{S}| \frac{\partial \hat{T}}{\partial x_j} - \Delta^2 \left( \widehat{\rho |\tilde{S}|} \frac{\partial \tilde{T}}{\partial x_j} \right) \quad (2.79)$$

Again, using the least squares approach and averaging in the homogeneous directions we get,

$$Pr_t = -c_p C_d \frac{\langle F_j F_j \rangle}{\langle H_k F_k \rangle} \quad (2.80)$$

The dynamic model can be considered “input free” except for the test to grid filter width ratio. According to the finding by Germano et al.(1991), a test filter width twice the grid filter width is satisfactory and was used in this research. This dynamic model was successfully used by Meng (2000)

## 2.6 Integral-Vector Form of Favre Filtered Equations

The nondimensional Favre filtered Navier-Stokes equations can be expressed in terms of  $(\bar{p}, \tilde{u}, \tilde{v}, \tilde{w}, \tilde{T})$  by multiplying the equation by the gas constant,  $R$ , and replacing density with resolved pressure,  $\bar{p}$  using the equation of state. The vector form of the equations is

$$\frac{\partial \mathbf{U}}{\partial \mathbf{W}} \frac{\partial \mathbf{W}}{\partial t} + \frac{\partial \mathbf{E}}{\partial x} + \frac{\partial \mathbf{F}}{\partial y} + \frac{\partial \mathbf{G}}{\partial z} = 0 \quad (2.81)$$

The integral form of Eq. 2.81 is expressed as

$$\int_{\Omega} [T] \frac{\partial \mathbf{W}}{\partial t} d\Omega + \int_{\partial \Omega} (\mathbf{E}\vec{i} + \mathbf{F}\vec{j} + \mathbf{G}\vec{k}) \cdot d\vec{S} = 0 \quad (2.82)$$

where  $\Omega$  is the volume of control volume,  $[T] = \partial \mathbf{U} / \partial \mathbf{W}$  is the time derivative Jacobian matrix which is given in Appendix A, and the flux vectors in  $x$ ,  $y$  and  $z$  directions respectively are defined as

$$\mathbf{E} = \mathbf{E}_i - \mathbf{E}_v + \mathbf{E}_s \quad (2.83)$$

$$\mathbf{F} = \mathbf{F}_i - \mathbf{F}_v + \mathbf{F}_s \quad (2.84)$$

$$\mathbf{G} = \mathbf{G}_i - \mathbf{G}_v + \mathbf{G}_s \quad (2.85)$$

where the subscript  $i$  denotes the inviscid contributions to the flux vector, the subscript  $v$  denotes the viscous contributions, and the subscript  $s$  denotes the subgrid scale contributions.

The vectors in Eq. 2.81 are defined as

$$\mathbf{W} = \begin{bmatrix} \bar{p} \\ \tilde{u} \\ \tilde{v} \\ \tilde{w} \\ \tilde{T} \end{bmatrix} ; \quad \mathbf{U} = \begin{bmatrix} \bar{p}/\tilde{T} \\ \bar{p}\tilde{u}/\tilde{T} \\ \bar{p}\tilde{v}/\tilde{T} \\ \bar{p}\tilde{w}/\tilde{T} \\ (\bar{p}/\tilde{T})[c_v\tilde{T} + (\tilde{u}^2 + \tilde{v}^2 + \tilde{w}^2)/2] \end{bmatrix} \quad (2.86)$$

$$\mathbf{E}_i = \begin{bmatrix} \bar{p}\tilde{u}/\tilde{T} \\ \bar{p}\tilde{u}^2/\tilde{T} + R\bar{p} \\ \bar{p}\tilde{u}\tilde{v}/\tilde{T} \\ \bar{p}\tilde{u}\tilde{w}/\tilde{T} \\ (\bar{p}\tilde{u}/\tilde{T})\hat{H} \end{bmatrix} ; \quad \mathbf{F}_i = \begin{bmatrix} \bar{p}\tilde{v}/\tilde{T} \\ \bar{p}\tilde{u}\tilde{v}/\tilde{T} \\ \bar{p}\tilde{v}^2/\tilde{T} + R\bar{p} \\ \bar{p}\tilde{v}\tilde{w}/\tilde{T} \\ (\bar{p}\tilde{v}/\tilde{T})\hat{H} \end{bmatrix} ; \quad \mathbf{G}_i = \begin{bmatrix} \bar{p}\tilde{w}/\tilde{T} \\ \bar{p}\tilde{u}\tilde{w}/\tilde{T} \\ \bar{p}\tilde{v}\tilde{w}/\tilde{T} \\ \bar{p}\tilde{w}^2/\tilde{T} + R\bar{p} \\ (\bar{p}\tilde{w}/\tilde{T})\hat{H} \end{bmatrix} \quad (2.87)$$

$$\mathbf{E}_v = \begin{bmatrix} 0 \\ \hat{\sigma}_{xx} \\ \hat{\sigma}_{xy} \\ \hat{\sigma}_{xz} \\ \tilde{u}\hat{\sigma}_{xx} + \tilde{v}\hat{\sigma}_{xy} + \tilde{w}\hat{\sigma}_{xz} - \hat{q}_x \end{bmatrix} ; \quad \mathbf{F}_v = \begin{bmatrix} 0 \\ \hat{\sigma}_{xy} \\ \hat{\sigma}_{yy} \\ \hat{\sigma}_{yz} \\ \tilde{u}\hat{\sigma}_{xy} + \tilde{v}\hat{\sigma}_{yy} + \tilde{w}\hat{\sigma}_{yz} - \hat{q}_y \end{bmatrix} ; \quad (2.88)$$

$$\mathbf{G}_v = \begin{bmatrix} 0 \\ \hat{\sigma}_{xz} \\ \hat{\sigma}_{yz} \\ \hat{\sigma}_{zz} \\ \tilde{u}\hat{\sigma}_{xz} + \tilde{v}\hat{\sigma}_{yz} + \tilde{w}\hat{\sigma}_{zz} - \hat{q}_z \end{bmatrix} \quad (2.89)$$

$$\mathbf{E}_s = \begin{bmatrix} 0 \\ \tau_{xx} \\ \tau_{xy} \\ \tau_{xz} \\ Q_x \end{bmatrix} ; \quad \mathbf{F}_s = \begin{bmatrix} 0 \\ \tau_{xy} \\ \tau_{yy} \\ \tau_{yz} \\ Q_y \end{bmatrix} ; \quad \mathbf{G}_s = \begin{bmatrix} 0 \\ \tau_{xz} \\ \tau_{yz} \\ \tau_{zz} \\ Q_z \end{bmatrix} \quad (2.90)$$

where the resolved total enthalpy is

$$\hat{H} = c_p \tilde{T} + \frac{1}{2}(\tilde{u}^2 + \tilde{v}^2 + \tilde{w}^2) \quad (2.91)$$

The viscous stress tensors are

$$\hat{\sigma}_{xx} = \frac{2\mu R}{3Re_{ref}} \left( 2\frac{\partial \tilde{u}}{\partial x} - \frac{\partial \tilde{v}}{\partial y} - \frac{\partial \tilde{w}}{\partial z} \right) \quad (2.92)$$

$$\hat{\sigma}_{yy} = \frac{2\mu R}{3Re_{ref}} \left( 2\frac{\partial \tilde{v}}{\partial y} - \frac{\partial \tilde{u}}{\partial x} - \frac{\partial \tilde{w}}{\partial z} \right) \quad (2.93)$$

$$\hat{\sigma}_{zz} = \frac{2\mu R}{3Re_{ref}} \left( 2\frac{\partial \tilde{w}}{\partial z} - \frac{\partial \tilde{u}}{\partial x} - \frac{\partial \tilde{v}}{\partial y} \right) \quad (2.94)$$

$$\hat{\sigma}_{xy} = \frac{\mu R}{Re_{ref}} \left( \frac{\partial \tilde{u}}{\partial y} + \frac{\partial \tilde{v}}{\partial x} \right) \quad (2.95)$$

$$\hat{\sigma}_{xz} = \frac{\mu R}{Re_{ref}} \left( \frac{\partial \tilde{u}}{\partial z} + \frac{\partial \tilde{w}}{\partial x} \right) \quad (2.96)$$

$$\hat{\sigma}_{yz} = \frac{\mu R}{Re_{ref}} \left( \frac{\partial \tilde{v}}{\partial z} + \frac{\partial \tilde{w}}{\partial y} \right) \quad (2.97)$$

and the heat flux vectors are

$$\hat{q}_x = -\frac{c_p \mu R}{Re_{ref} Pr} \frac{\partial \tilde{T}}{\partial x} ; \quad \hat{q}_y = -\frac{c_p \mu R}{Re_{ref} Pr} \frac{\partial \tilde{T}}{\partial y} ; \quad \hat{q}_z = -\frac{c_p \mu R}{Re_{ref} Pr} \frac{\partial \tilde{T}}{\partial z} \quad (2.98)$$

Finally, the SGS stress tensors are

$$\tau_{xx} = \frac{1}{3}q^2 R - \frac{2\mu_t R}{3} \left( 2\frac{\partial \tilde{u}}{\partial x} - \frac{\partial \tilde{v}}{\partial y} - \frac{\partial \tilde{w}}{\partial z} \right) \quad (2.99)$$

$$\tau_{yy} = \frac{1}{3}q^2 R - \frac{2\mu_t R}{3} \left( 2\frac{\partial \tilde{v}}{\partial y} - \frac{\partial \tilde{u}}{\partial x} - \frac{\partial \tilde{w}}{\partial z} \right) \quad (2.100)$$

$$\tau_{zz} = \frac{1}{3}q^2 R - \frac{2\mu_t R}{3} \left( 2\frac{\partial \tilde{w}}{\partial z} - \frac{\partial \tilde{u}}{\partial x} - \frac{\partial \tilde{v}}{\partial y} \right) \quad (2.101)$$

$$\tau_{xy} = -\mu_t R \left( \frac{\partial \tilde{u}}{\partial y} + \frac{\partial \tilde{v}}{\partial x} \right) \quad (2.102)$$

$$\tau_{xz} = -\mu_t R \left( \frac{\partial \tilde{u}}{\partial z} + \frac{\partial \tilde{w}}{\partial x} \right) \quad (2.103)$$

$$\tau_{yz} = -\mu_t R \left( \frac{\partial \tilde{v}}{\partial z} + \frac{\partial \tilde{w}}{\partial y} \right) \quad (2.104)$$

and the SGS heat flux vectors are

$$Q_x = -\frac{c_p \mu_t R}{Pr_t} \frac{\partial \tilde{T}}{\partial x} ; \quad Q_y = -\frac{c_p \mu_t R}{Pr_t} \frac{\partial \tilde{T}}{\partial y} ; \quad Q_z = -\frac{c_p \mu_t R}{Pr_t} \frac{\partial \tilde{T}}{\partial z} \quad (2.105)$$

The integral governing equations in conservation form, Eq. 2.82, were numerically solved using a finite volume formulation based on Cartesian coordinates as discussed in the next chapter.

## CHAPTER 3. FINITE VOLUME FORMULATION

The numerical discretization of the filtered compressible NS equations based on Cartesian coordinates is described in this chapter. The finite volume method starts from the integral form of the conserved equations and the conservation principles are applied to each contiguous control volume. The advantage of the finite volume method is that it is easily extended to be suitable for the flows in complex geometries. Recently, finite volume methods have been used for many DNS and LES computations with staggered meshes in pipe flows (Satake and Kunugi, 1998a; Yang, 2000). But to the author's knowledge, all the finite volume methods were based on the conservation equations in cylindrical coordinates. This may be the first LES work to apply the finite volume method on turbulent flows in pipes based on Cartesian coordinates. The spatial discretization procedure and time marching scheme based on Cartesian coordinates are explained in detail.

### 3.1 Spatial Discretization

#### 3.1.1 Dependent Variables

To avoid the singularity at the center line of a pipe when using cylindrical coordinates, the radial flux,  $q_r = rv_r$ , was used as one of the primitive variables with a staggered grid in most DNS research (Verzicco and Orlandi, 1996; Satake and Kunugi, 1998a). Similarly, both axial and radial fluxes,  $q_x = ru$  and  $q_r = rv_r$ , were used as primitive variables by Yang (2000) in dealing with the singularity in his LES simulations. But in the current work, the primitive variables  $(p, u_i, T)$  were used to apply a low Mach number preconditioning method (Pletcher and Chen, 1993). Large eddy simulations of channel flow with significant heat transfer using this preconditioning method with primitive variables  $(p, u_i, T)$  were reported by Wang and

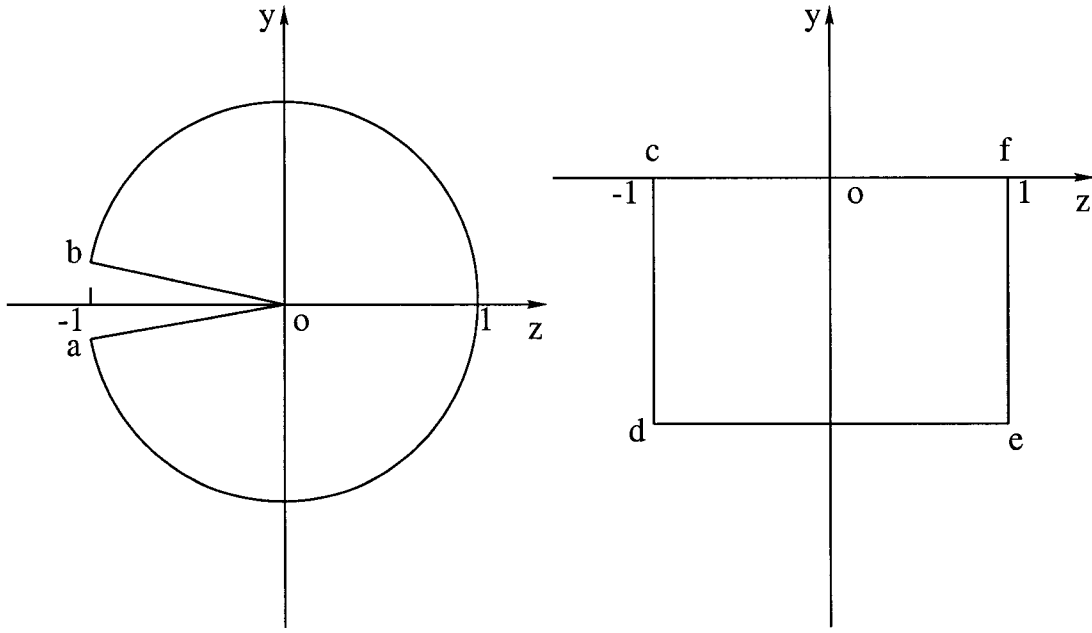


Figure 3.1 Sketch of the computational domain and analogous domain

Pletcher (1996) and Dailey and Pletcher (1998).

Shuen, Chen and Choi (1992) found that at low Mach numbers, if the conserved variables are used, computing the pressure from the equation of state may result in significant roundoff errors. Therefore, instead of using density as a primitive variable, the pressure, is used as a dependent variable.

### 3.1.2 Computational Domain

To solve the governing equations in Cartesian coordinates, the computational domain in the  $yz$  plane is made analogous to a rectangular region as shown in Fig. 3.1. The computational domain is cut along the radius  $oa$ , and points  $a$  and  $b$  are the same point. The boundary  $oa$  in the computational domain is analogous to the boundary  $cd$  in the rectangular domain, and  $ab$  and  $ob$  are analogous to  $de$  and  $fe$ , respectively. The center point,  $o$ , in the computational domain is analogous to boundary  $cf$  by setting the same coordinates for all the vertices in the boundary. Consequently, the computational domain has four boundaries, boundary  $oa$ , boundary  $ob$ , boundary  $ab$  and point  $o$ . Periodic boundary conditions are applied in the boundaries of  $oa$  and  $ob$ , no slip boundary conditions are used on the wall boundary,  $ab$ . For

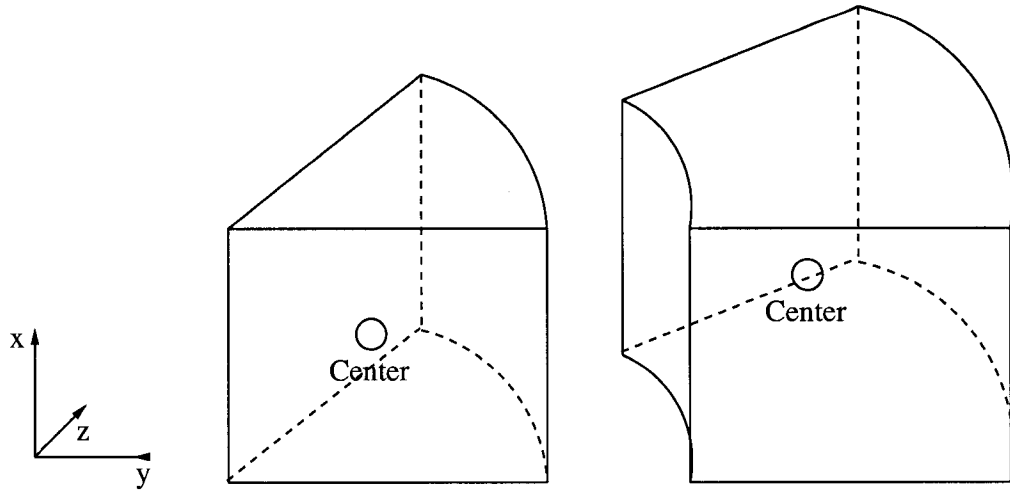


Figure 3.2 Sketch of control volumes

point  $o$ , no boundary condition is needed because the area goes zero and the momentum and mass flux is zero too. Consequently, no singularity is encountered at the center point.

### 3.1.3 Integral Approximations

The solution domain was continuously subdivided into non-Cartesian hexahedral and tetrahedral control volumes of unequal dimensions based on cylindrical coordinates. The typical two types of control volumes are shown in Fig. 3.2. The primitive variables ( $p$ ,  $u_i$ ,  $T$ ) were stored at the geometric centers of the control volumes (cell center scheme). The cell center approach is second-order accuracy on smoothly stretched meshes, has three decoupling modes, and compared with the cell vertex method, the solution domain is easier to decompose into multi-blocks. This is very important for the treatment of complex geometries and parallelization of the code. The disadvantage of the cell center approach is that additional storage is needed for the image cells. Since the multi-block and complex geometry capabilities were considered very important in this research, the cell center method was used.

The integral-vector form of the filtered governing equations, given by Eq. 2.82, was applied to each control volume as well as the whole solution domain. To obtain an algebraic equation for each control volume, the surface and volume integrals must be approximated. A hexahedral control volume depicted in Fig 3.3 is used to explain the approximations in detail and the

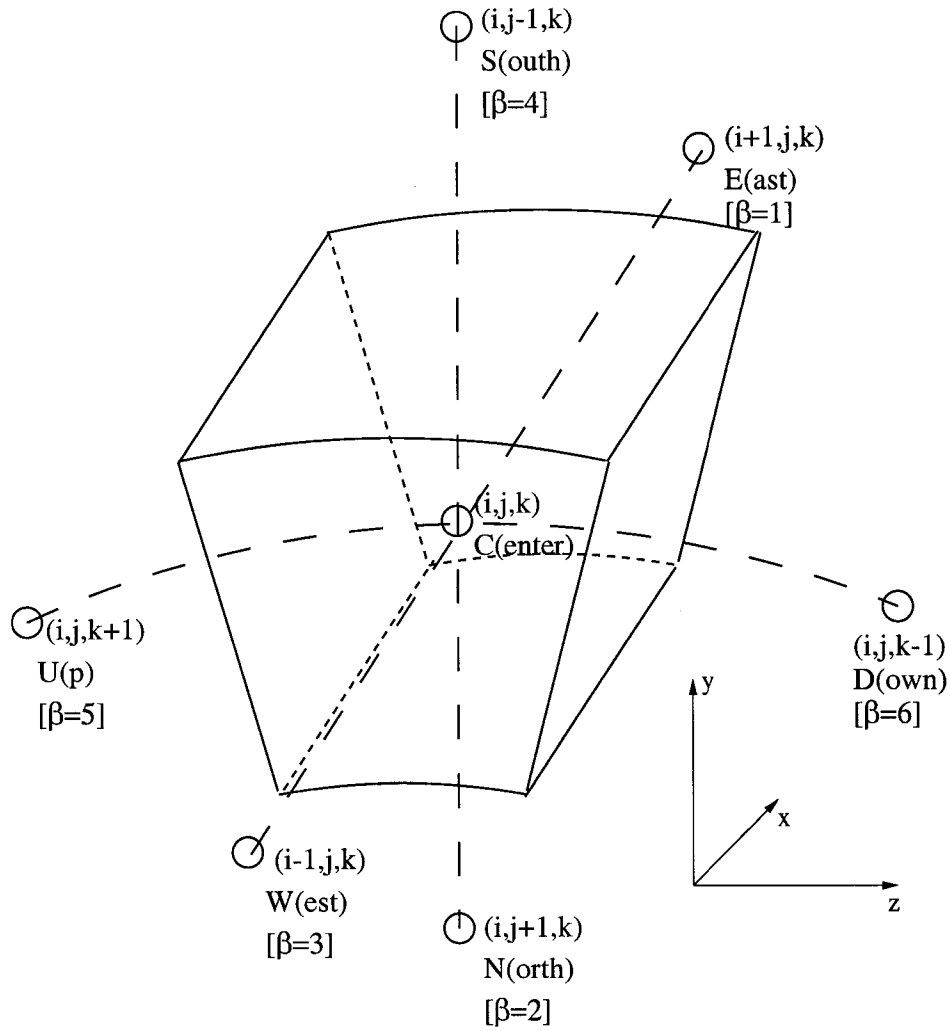


Figure 3.3 Non-Cartesian hexahedral control volume with cell center,  $(i,j,k)$ , and six neighboring cell centers, labeled as E, W, N, S, U, and D

approximations of the tetrahedral control volume can be obtained analogously. The cell center of this control volume is labeled as  $C$  and the cell centers of its six neighboring control volumes are labeled as  $E$ ,  $W$ ,  $N$ ,  $S$ ,  $U$  and  $D$ . The index  $i$  is increasing in the streamwise direction, index  $j$  is increasing from wall boundary toward pipe centerline, and the index  $k$  is increasing in the counter clockwise direction.  $\beta$  denotes the six faces of the control volumes.

The simplest second-order accurate approximation for the volume integral in Eq 2.82 is obtained by replacing the integral by the product of the mean value and the volume of the cell:

$$\int_{\Omega} [T] \frac{\partial \mathbf{W}}{\partial t} d\Omega \approx \left( [T] \frac{\partial \mathbf{W}}{\partial t} \right)_{i,j,k} \Omega_{i,j,k} \quad (3.1)$$

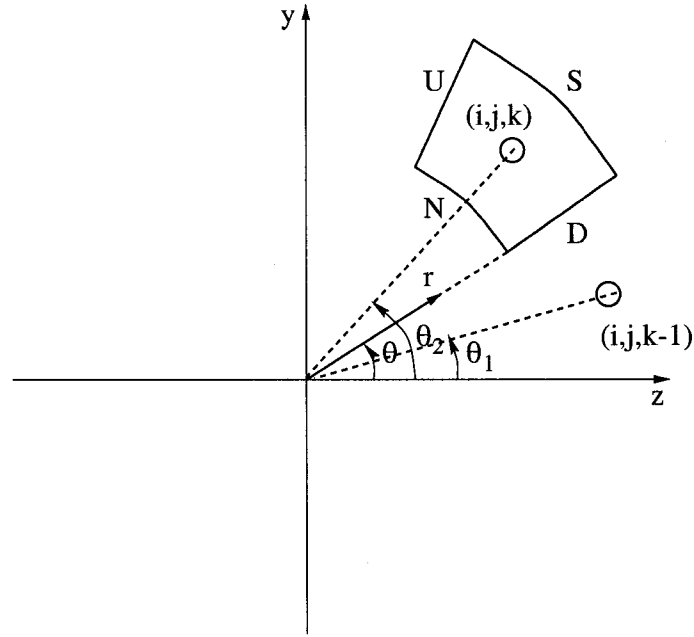


Figure 3.4 Sketch of non-Cartesian the hexahedral volume for approximations of  $v$  and  $w$  at the D surface

where the mean value is approximated as the value at the center of the control volume.

To calculate the surface integral in Eq. 2.82 exactly, the flux vectors should be known everywhere on the surface. Since the information at the center of the control volumes was available, the cell face values were approximated in terms of the volume center values using the “mid-point” rule. The weighting function which will be introduced in next section was needed in the radius direction because the grid was stretched toward the wall. Consequently, the surface integrals were approximated as

$$\int_{\partial\Omega} (\mathbf{E}\vec{i} + \mathbf{F}\vec{j} + \mathbf{G}\vec{k}) \cdot d\vec{S} \approx \mathbf{C}(\mathbf{W}) \quad (3.2)$$

where

$$\mathbf{C}(\mathbf{W}) = \sum_{\beta=1}^6 [(\mathbf{E}n_x + \mathbf{F}n_y + \mathbf{G}n_z) S]_{\beta} \quad (3.3)$$

and  $d\vec{S}$  is the cell face area vector,  $(n_x, n_y, n_z)$  is the unit normal of the surface. For east/west (E/W) and up/down (U/D) faces,  $S$  is the magnitude of the face area vector, but for north/south (N/S) faces, it is the area of the N/S face projected onto a plane perpendicular to  $(n_x, n_y, n_z)$ .

To calculate the flux vectors at the cell face centers, first the primitive variables  $p, u, v, w$

and  $T$  were approximated in terms of the primitive variable values at the cell centers, between which the cell face lies. However, the  $v$  and  $w$  can't be simply averaged at the up and down surface due to the non-Cartesian hexahedral control volume. The  $v$  and  $w$  at the cell centers were first transferred to  $v_r$  and  $v_\theta$ , and then  $v_r$  and  $v_\theta$  were averaged at the up and down surfaces; finally, the  $v_r$  and  $v_\theta$  were decomposed to  $v$  and  $w$ . For example, as shown in Fig. 3.4, to obtain the approximations of  $v$  and  $w$  at the D surface, first  $v_r$  and  $v_\theta$  were calculated at the surface as

$$v_r = \frac{1}{2}(v_{i,j,k-1} \sin \theta_1 + w_{i,j,k-1} \cos \theta_1 + v_{i,j,k} \sin \theta_2 + w_{i,j,k} \cos \theta_2) \quad (3.4)$$

$$v_\theta = \frac{1}{2}(v_{i,j,k-1} \cos \theta_1 - w_{i,j,k-1} \sin \theta_1 + v_{i,j,k} \cos \theta_2 - w_{i,j,k} \sin \theta_2) \quad (3.5)$$

and then  $v_r$  and  $v_\theta$  were decomposed as

$$v = v_r \sin \theta + v_\theta \cos \theta \quad (3.6)$$

$$w = v_r \cos \theta - v_\theta \sin \theta \quad (3.7)$$

Consequently, the flux vectors on the cell faces were calculated using the primitive variable values. The tetrahedral volume at the center region of pipe, as shown in Fig 3.5, can be considered as the special case of hexahedral volumes, whose north surface is collapsed to a line. Therefore, the integral approximations for the tetrahedral volumes were obtained in a way analogous to the procedure for the hexahedral volumes.

With these approximations to the integrals, Eq. 2.82 becomes

$$[T] \frac{\partial \mathbf{W}}{\partial t} \Omega + \mathbf{C}(\mathbf{W}) = 0 \quad (3.8)$$

### 3.1.4 Gradients

The gradients of  $u$ ,  $v$ ,  $w$  and  $T$  at the cell faces are needed to calculate the viscous and sub-grid scale contributions to the flux vectors. The face based approach is used in this work and the gradients were calculated and stored on the faces of the control volumes. The gradients were calculated using the Gauss divergence theorem on an auxiliary control volume as

$$\int_{\Omega'} \nabla \phi d\Omega' = \int_{\partial\Omega'} \phi d\vec{S}' \quad (3.9)$$

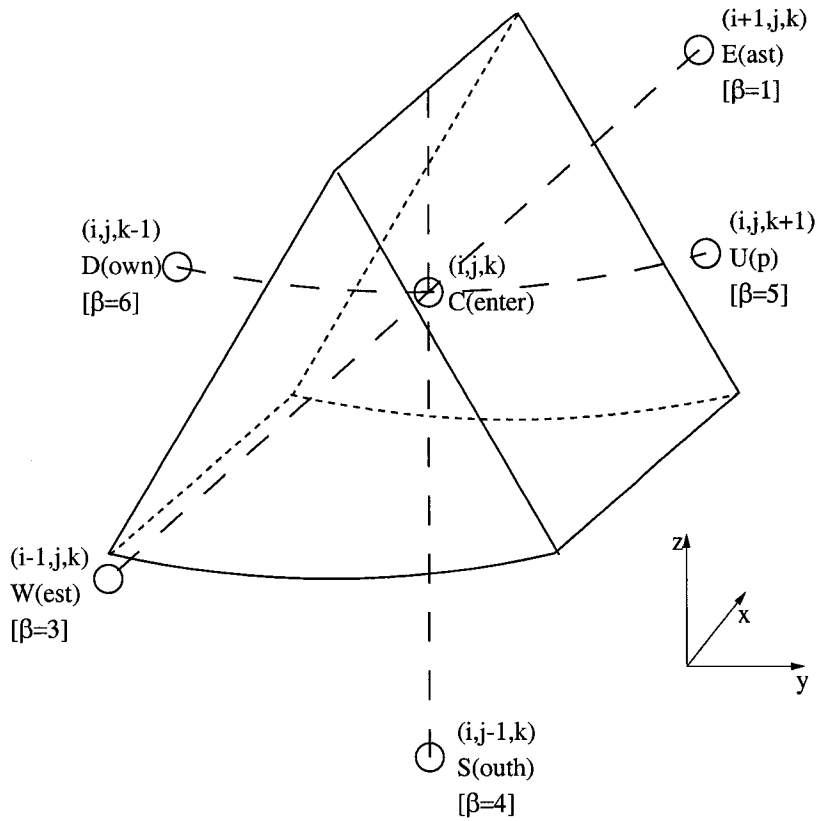


Figure 3.5 Non-Cartesian tetrahedral control volume with cell center,  $(i,j,k)$ , and five neighboring cell centers, labeled as E, W, S, U, and D

where  $\phi$  is a scalar,  $\Omega'$  is the volume of auxiliary control volume and  $d\vec{S}'$  is the cell face area vector of the auxiliary volume.

The auxiliary control volume was obtained by shifting the main control volume a half index in the direction of the particular cell face on which the gradient is to be calculated. For example, the auxiliary control volume used to calculate the gradients on the east/west (E/W) faces of the main control volume is shown in Fig 3.6, where the cell centers of the main control volumes coincide with the east and west faces of the auxiliary volume. For the Cartesian coordinates,  $\nabla\phi = \phi_x\vec{i} + \phi_y\vec{j} + \phi_z\vec{k}$ .  $\nabla\phi$  was obtained by approximating Eq. 3.9 as

$$(\nabla\phi)_{i+1/2,j,k}\Omega' = \sum_{\beta'=1}^6 [(\phi_{n'_x}\vec{i} + \phi_{n'_y}\vec{j} + \phi_{n'_z}\vec{k})S']_{\beta'} \quad (3.10)$$

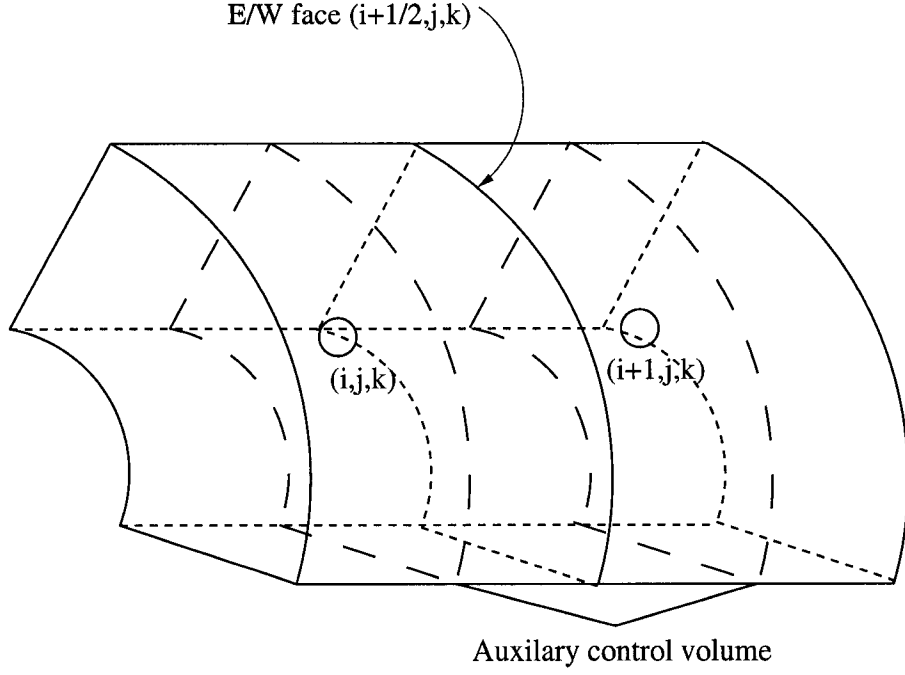


Figure 3.6 Auxiliary non-Cartesian hexahedral control volume for calculation of gradients on east/west (E/W) faces of the main control volume

where the volume of the auxiliary control volume is

$$\Omega' = \frac{1}{2}[\Omega_{i,j,k} + \Omega_{i+1,j,k}] \quad (3.11)$$

and  $(n'_x, n'_y, n'_z)$  is the unit normal of the auxiliary cell faces. Just as for the main control volume, for the E/W and U/D auxiliary cell faces,  $S'$  is the magnitude of the auxiliary cell face area vector, while for the N/S faces, it is the area of the auxiliary N/S face projected onto a plane perpendicular to  $(n'_x, n'_y, n'_z)$ .

When the grid was stretched near the wall and uniform in the  $x$  and circumferential directions, the scalar  $\phi$  on the cell faces of the auxiliary control volume was defined as

$$\phi_{E'} = \phi_{i+1,j,k} \quad (3.12)$$

$$\phi_{W'} = \phi_{i,j,k} \quad (3.13)$$

$$\phi_{N'} = \frac{1}{2} \{ [\alpha_r^+ \phi_{i+1,j+1,k} + (1 - \alpha_r^+) \phi_{i+1,j,k}] + [\alpha_r^+ \phi_{i,j+1,k} + (1 - \alpha_r^+) \phi_{i,j,k}] \} \quad (3.14)$$

$$\phi_{S'} = \frac{1}{2} \{ [\alpha_r^- \phi_{i+1,j-1,k} + (1 - \alpha_r^-) \phi_{i+1,j,k}] + [\alpha_r^- \phi_{i,j-1,k} + (1 - \alpha_r^-) \phi_{i,j,k}] \} \quad (3.15)$$

$$\phi_{U'} = \frac{1}{2} [\phi_U(i+1, j, k) + \phi_U(i, j, k)] \quad (3.16)$$

$$\phi_{D'} = \frac{1}{2} [\phi_D(i+1, j, k) + \phi_D(i, j, k)] \quad (3.17)$$

where the weighting functions are

$$\alpha_r^+ = \frac{\Delta r/2}{\sqrt{(y_{i,j+1,k} - y_{i,j,k})^2 + (z_{i,j+1,k} - z_{i,j,k})^2}} \quad (3.18)$$

$$\alpha_r^- = \frac{\Delta r/2}{\sqrt{(y_{i,j,k} - y_{i,j-1,k})^2 + (z_{i,j,k} - z_{i,j-1,k})^2}} \quad (3.19)$$

and  $\Delta r$  is the distance between the north and south surface of the auxiliary control volume.  $\phi_U$  and  $\phi_D$  are the variable values on the up and down faces of the main control volume, and can be calculated using the method in section 3.1.3. The auxiliary cell face areas are given by

$$S'_E = S_E \quad (3.20)$$

$$S'_W = S_W \quad (3.21)$$

$$S'_N = \frac{1}{2} [S_N(i, j, k) + S_N(i+1, j, k)] \quad (3.22)$$

$$S'_S = \frac{1}{2} [S_S(i, j, k) + S_S(i+1, j, k)] \quad (3.23)$$

$$S'_U = \frac{1}{2} [S_U(i, j, k) + S_U(i+1, j, k)] \quad (3.24)$$

$$S'_D = \frac{1}{2} [S_D(i, j, k) + S_D(i+1, j, k)] \quad (3.25)$$

Gradients on the north/south (N/S) and up/down (U/D) faces were calculated in a similar way.

### 3.2 Low Mach Preconditioning

Lots of mixed compressible/incompressible type flows exist in nature and engineering applications. For such problems the flow is nearly incompressible with a locally low Mach number in some regions, whereas the flow is compressible in other regions. An example is a flow around a body with a large stagnation region. Also in some cases, such as a low speed flow with high heat transfer or flows with chemical reactions, there are significant density and property variations and the incompressible assumption is not valid. Hence, it is important and of interest

to solve the compressible equations for low Mach numbers. However, it is well known that the convergence speed becomes very slow when solving compressible equations at low Mach numbers (Volpe, 1991). This is associated with the large disparity of the acoustic wave speed,  $u + a$  and convective speed  $u$  which makes the compressible NS equations very stiff. As the Mach number tends to zero, the acoustic wave speed tends to infinity. This results in a large difference in the eigenvalues of the resulting system. The convergence rate of many schemes depend on the condition number,  $\kappa$ , which is defined as

$$\kappa = \frac{\lambda_{max}}{\lambda_{min}} \quad (3.26)$$

where  $\lambda_{max}$  and  $\lambda_{min}$  are the largest and smallest eigenvalues of the system. Larger condition numbers result in a slower convergence speed. This makes the computation of low Mach number flows with compressible solver practically impossible.

To overcome this problem, a time derivative preconditioning method has been investigated by many researchers (Tukel, 1987, Feng and Merkle, 1990, Choi and Merkle, 1993). Pletcher and Chen (1993) developed a similar preconditioning formulation which was successfully used in large eddy simulation of channel flow (Dailey, 1997). This method was also applied here by adding a pseudo time derivative which is premultiplied by a preconditioning matrix to the governing equations. By incorporating the preconditioning, Eq. 3.8 becomes

$$[\Gamma] \frac{\partial \mathbf{W}}{\partial \tau} \Omega + [T] \frac{\partial \mathbf{W}}{\partial t} \Omega + \mathbf{C}(\mathbf{W}) = 0 \quad (3.27)$$

where  $\tau$  is the pseudo time and  $[\Gamma]$  is the preconditioning matrix which is given in Appendix A. The preconditioning matrix is very similar to the matrix  $[T]$  except the first column of  $[\Gamma]$  has been multiplied by the non-dimensional gas constant,  $R$ . With the preconditioning technique, the magnitudes of the system eigenvalues become closer together. Consequently the condition number becomes much smaller than the original one, and the convergence rate is improved dramatically for the time marching scheme. The addition of the pseudo time derivative is termed the dual time step approach, and involves iterating in pseudo time for each step in physical time. The original unsteady governing equations are satisfied when the iteration process is converged in pseudo time.

### 3.3 LU-SGS Scheme

Time integration was performed using the implicit lower-upper symmetric Gauss-Seidel (LU-SGS) scheme with a dual time stepping approach. The LU-SGS scheme was originally developed by Yoon and Jameson (1987) for the Euler and Navier-Stokes equations without preconditioning. Rieger and Jameson (1988) extended the LU-SGS scheme to three dimensions to solve the steady compressible Navier-Stokes equations using a finite volume method. Grasso and Marini (1991) used the LU-SGS scheme in a finite volume formulation to simulate two-dimensional high speed flow with an upwind biased TVD spatial discretization. Chen and Shuen (1994) solved the preconditioned Navier-Stokes equations using the LU-SGS scheme in a finite difference formulation. Dailey (1997) applied the LU-SGS scheme in a finite volume cell-center formulation to solve the preconditioned, time accurate, Favre filtered governing equations in a dual time stepping approach. This methodology was extended here to non-Cartesian control volumes.

Beginning with the preconditioned equation, Eq. 3.27, the pseudo time derivative was discretized with a first order accurate Euler backward difference, and the physical time derivative was discretized with a second-order accurate three point backward difference, giving

$$[\Gamma] \frac{\Delta \mathbf{W}}{\Delta \tau} \Omega + [T] \frac{\Omega}{2\Delta t} (3\mathbf{W}^{n+1} - 4\mathbf{W}^n + \mathbf{W}^{n-1}) + \mathbf{C}(\mathbf{W}^{n+1}) = 0 \quad (3.28)$$

where  $\Delta \mathbf{W} = \mathbf{W}^{m+1} - \mathbf{W}^m$ ,  $\Delta \tau = \tau^{m+1} - \tau^m$ ,  $m + 1$  denotes the current pseudo time step and  $n + 1$  denotes the current physical time step. For the first physical time step, the Euler backward difference was applied to the physical time discretization. To solve the nonlinear equation, Eq 3.28, the inviscid flux vectors were linearized about the pseudo time level  $m$  as

$$\mathbf{E}_i^{m+1} \approx \mathbf{E}_i^m + [A]^m \Delta \mathbf{W} \quad ; \quad [A] = \left( \frac{\partial \mathbf{E}_i}{\partial \mathbf{W}} \right)^m \quad (3.29)$$

$$\mathbf{F}_i^{m+1} \approx \mathbf{F}_i^m + [B]^m \Delta \mathbf{W} \quad ; \quad [B] = \left( \frac{\partial \mathbf{F}_i}{\partial \mathbf{W}} \right)^m \quad (3.30)$$

$$\mathbf{G}_i^{m+1} \approx \mathbf{G}_i^m + [C]^m \Delta \mathbf{W} \quad ; \quad [C] = \left( \frac{\partial \mathbf{G}_i}{\partial \mathbf{W}} \right)^m \quad (3.31)$$

where the inviscid flux Jacobians ( $[A]$ ,  $[B]$  and  $[C]$ ) are given in Appendix A. The viscous stresses and sub-grid scale stresses were lagged as the values of the previous pseudo time step.

Because the contributions of the viscous stresses and sub-grid scale stresses are assumed to be small, this lag is expected not to slow down the convergence.

The linearized fluxes were substituted into Eq. 3.28, and the entire equation was multiplied by  $[\Gamma]^{-1}$ . Consequently, the “delta” form equation at the pseudo time level  $m$  was given as

$$\left\{ \frac{\Omega}{\Delta\tau}[I] + [\Gamma]^{-1}[T] \frac{3}{2} \frac{\Omega}{\Delta t} + [\Gamma]^{-1} \sum_{\beta=1}^6 [(A)n_x + (B)n_y + (C)n_z] S_\beta \right\}^m \Delta \mathbf{W} = -\mathfrak{R}^m \quad (3.32)$$

where  $[I]$  is the identity matrix and the preconditioned residual,  $\mathfrak{R}$ , is defined as

$$\mathfrak{R} = [\Gamma]^{-1} \mathbf{R} \quad (3.33)$$

The viscous and sub-grid scale terms were included in the preconditioned residual.

The  $yz$  plane for a control volume  $(i, j, k)$  is shown in Fig. 3.7, the N/S faces at  $(i, j \pm 1/2, k)$  are labeled as  $\beta = 2$  and 4, and the U/D faces at  $(i, j, k \pm 1/2)$  are labeled as  $\beta = 5$  and 6. Similarly, the E/W faces at  $(i \pm 1/2, j, k)$  are labeled as  $\beta = 1$  and 3. As depicted in Fig 3.7,  $(n_{y_1}, n_{z_1})$  is the unit normal of the north face and  $(n_{y_2}, n_{z_2})$  is the unit normal of the up face. The inviscid flux Jacobians on each face are defined as

$$\begin{aligned} [\hat{A}] &= ([A])_{\beta=1,3} \\ [\hat{B}] &= ([B]n_{y_1} + [C]n_{z_1})_{\beta=2,4} \\ [\hat{C}] &= ([B]n_{y_2} + [C]n_{z_2})_{\beta=5,6} \end{aligned} \quad (3.34)$$

Substituting Eq. 3.34 into Eq. 3.32, we get

$$\begin{aligned} &\left[ \frac{\Omega}{\Delta\tau}[I] + [\Gamma]^{-1}[T] \frac{3}{2} \frac{\Omega}{\Delta t} \right. \\ &\left. + [\Gamma]^{-1} \left( [\hat{A}]_1 S_1 - [\hat{A}]_3 S_3 + [\hat{B}]_2 S_2 - [\hat{B}]_4 S_4 + [\hat{C}]_5 S_5 - [\hat{C}]_6 S_6 \right) \right] \Delta \mathbf{W} = -\mathfrak{R} \end{aligned} \quad (3.35)$$

Notice that the preconditioning matrix is not included in the pseudo-time term and the system is still diagonal dominant without this term, the equation, Eq. 3.35 can be simplified by dropping the pseudo-time term as

$$\left[ [\Gamma]^{-1}[T] \frac{3}{2} \frac{\Omega}{\Delta t} + [\Gamma]^{-1} \left( [\hat{A}]_1 S_1 - [\hat{A}]_3 S_3 + [\hat{B}]_2 S_2 - [\hat{B}]_4 S_4 + [\hat{C}]_5 S_5 - [\hat{C}]_6 S_6 \right) \right] \Delta \mathbf{W} = -\mathfrak{R} \quad (3.36)$$

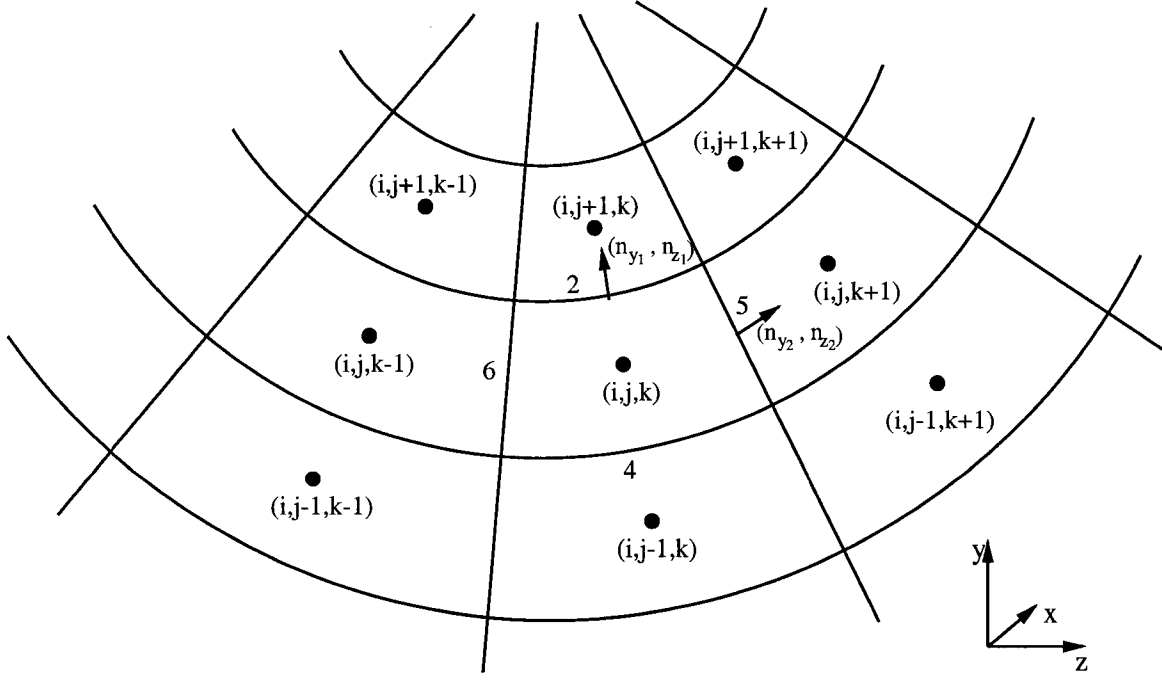


Figure 3.7 Sketch of grids in yz plane

But the iteration, which is still called pseudo-time iteration in this work, is still needed to drive the Newton linearization error to zero in each physical time step.

To apply the LU-SGS algorithm to the preconditioned equations, the flux Jacobians were modified following Chen and Shuen (1994) as

$$\begin{aligned}
 [\hat{A}] &= [\Gamma][\Gamma]^{-1}[\hat{A}] = [\Gamma][\tilde{A}] \quad ; \quad [\tilde{A}] = [\Gamma]^{-1}[\hat{A}] \\
 [\hat{B}] &= [\Gamma][\Gamma]^{-1}[\hat{B}] = [\Gamma][\tilde{B}] \quad ; \quad [\tilde{B}] = [\Gamma]^{-1}[\hat{B}] \\
 [\hat{C}] &= [\Gamma][\Gamma]^{-1}[\hat{C}] = [\Gamma][\tilde{C}] \quad ; \quad [\tilde{C}] = [\Gamma]^{-1}[\hat{C}]
 \end{aligned} \tag{3.37}$$

To ensure the diagonal dominance, the flux Jacobians were split as

$$\begin{aligned}
 [\tilde{A}] &= [\tilde{A}]^+ + [\tilde{A}]^- \\
 [\tilde{B}] &= [\tilde{B}]^+ + [\tilde{B}]^- \\
 [\tilde{C}] &= [\tilde{C}]^+ + [\tilde{C}]^-
 \end{aligned} \tag{3.38}$$

where

$$[\tilde{A}]^\pm = \frac{1}{2} \left( [\tilde{A}] \pm |\lambda_{[\tilde{A}]}| [I] \right)$$

$$\begin{aligned} [\tilde{B}]^\pm &= \frac{1}{2} \left( [\tilde{B}] \pm |\lambda_{[\tilde{B}]}| [I] \right) \\ [\tilde{C}]^\pm &= \frac{1}{2} \left( [\tilde{C}] \pm |\lambda_{[\tilde{C}]}| [I] \right) \end{aligned} \quad (3.39)$$

$\lambda_{[\tilde{A}]}$ ,  $\lambda_{[\tilde{B}]}$  and  $\lambda_{[\tilde{C}]}$  are maximum eigenvalues of flux Jacobian  $[\tilde{A}]$ ,  $[\tilde{B}]$  and  $[\tilde{C}]$  respectively.

For preconditioned system, the maximum eigenvalues are

$$\begin{aligned} \lambda_{[\tilde{A}]} &= \frac{1}{2R} \left[ (R+1)|u| + \sqrt{(R-1)^2 u^2 + 4Rc^2} \right] \\ \lambda_{[\tilde{B}]} &= \frac{1}{2R} \left[ (R+1)|vn_{y_1} + wn_{z_1}| \right. \\ &\quad \left. + \sqrt{(R-1)^2 (vn_{y_1} + wn_{z_1})^2 + 4Rc^2} \right] \\ \lambda_{[\tilde{C}]} &= \frac{1}{2R} \left[ (R+1)|vn_{y_2} + wn_{z_2}| \right. \\ &\quad \left. + \sqrt{(R-1)^2 (vn_{y_2} + wn_{z_2})^2 + 4Rc^2} \right] \end{aligned} \quad (3.40)$$

where  $R$  is gas constant,  $c$  is the speed of sound and  $u$ ,  $v$  and  $w$  are Cartesian velocity components in the  $x$ ,  $y$  and  $z$  directions, respectively.

For those control volumes not in the pipe center region, i.e. non-Cartesian hexahedral volumes, the flux Jacobians on the cell faces were approximated as

$$\begin{aligned} ([\Gamma][\tilde{A}]\Delta\mathbf{W})_1 S_1 &= ([\Gamma][\tilde{A}]^+ \Delta\mathbf{W})_{i,j,k} S_1 + ([\Gamma][\tilde{A}]^- \Delta\mathbf{W})_{i+1,j,k} S_1 \\ ([\Gamma][\tilde{A}]\Delta\mathbf{W})_3 S_3 &= ([\Gamma][\tilde{A}]^+ \Delta\mathbf{W})_{i-1,j,k} S_3 + ([\Gamma][\tilde{A}]^- \Delta\mathbf{W})_{i,j,k} S_3 \\ ([\Gamma][\tilde{B}]\Delta\mathbf{W})_2 S_2 &= ([\Gamma][\tilde{B}]^+ \Delta\mathbf{W})_{i,j,k} S_{i,j,k} + ([\Gamma][\tilde{B}]^- \Delta\mathbf{W})_{i,j+1,k} S_{i,j+1,k} \\ ([\Gamma][\tilde{B}]\Delta\mathbf{W})_4 S_4 &= ([\Gamma][\tilde{B}]^+ \Delta\mathbf{W})_{i,j-1,k} S_{i,j-1,k} + ([\Gamma][\tilde{B}]^- \Delta\mathbf{W})_{i,j,k} S_{i,j,k} \\ ([\Gamma][\tilde{C}]\Delta\mathbf{W})_5 S_5 &= ([\Gamma][\tilde{C}]^+ \Delta\mathbf{W})_{i,j,k} S_5 + ([\Gamma][\tilde{C}]^- \Delta\mathbf{W})_{i,j,k+1} S_5 \\ ([\Gamma][\tilde{C}]\Delta\mathbf{W})_6 S_6 &= ([\Gamma][\tilde{C}]^+ \Delta\mathbf{W})_{i,j,k-1} S_6 + ([\Gamma][\tilde{C}]^- \Delta\mathbf{W})_{i,j,k} S_6 \end{aligned} \quad (3.41)$$

where  $S_1 = S_3$ ,  $S_5 = S_6$  and  $S_{i,j,k} = \frac{1}{2}(S_2 + S_4)_{i,j,k}$ .

Substituting Eq. 3.37 and Eq. 3.41 into Eq. 3.36 gives

$$([L] + [D] + [U])\Delta\mathbf{W} = -\mathfrak{R} \quad (3.42)$$

where the matrices  $[L]$ ,  $[D]$  and  $[U]$  are

$$[L] = -[\Gamma]^{-1} \left[ ([\Gamma][\tilde{A}]^+)_{i-1,j,k} S_3 + ([\Gamma][\tilde{B}]^+)_{i,j-1,k} S_{i,j-1,k} + ([\Gamma][\tilde{C}]^+)_{i,j,k-1} S_6 \right] \quad (3.43)$$

$$\begin{aligned}
[D] &= [\Gamma]^{-1}[T]\frac{3}{2}\frac{\Omega}{\Delta t} + [\Gamma]^{-1} \left[ ([\Gamma][\tilde{A}]^+)_{i,j,k}S_1 - ([\Gamma][\tilde{A}]^-)_{i,j,k}S_3 + ([\Gamma][\tilde{B}]^+)_{i,j,k}S_{i,j,k} \right. \\
&\quad \left. - ([\Gamma][\tilde{B}]^-)_{i,j,k}S_{i,j,k} + ([\Gamma][\tilde{C}]^+)_{i,j,k}S_5 - ([\Gamma][\tilde{C}]^-)_{i,j,k}S_6 \right] \quad (3.44)
\end{aligned}$$

$$[U] = [\Gamma]^{-1} \left[ ([\Gamma][\tilde{A}]^-)_{i+1,j,k}S_1 + ([\Gamma][\tilde{B}]^-)_{i,j+1,k}S_{i,j+1,k} + ([\Gamma][\tilde{C}]^-)_{i,j,k+1}S_5 \right] \quad (3.45)$$

It was found that  $[D]$  only depends on the center point  $(i, j, k)$ ,  $[L]$  only depends on the lower points and  $[U]$  only depends on the upper points. These facts were utilized in the solution procedure.

Because of the splitting of the flux Jacobians,

$$[\Gamma][\tilde{A}]^+ - [\Gamma][\tilde{A}]^- = \left| \lambda_{[\tilde{A}]} \right| [\Gamma] \quad (3.46)$$

$$[\Gamma][\tilde{B}]^+ - [\Gamma][\tilde{B}]^- = \left| \lambda_{[\tilde{B}]} \right| [\Gamma] \quad (3.47)$$

$$[\Gamma][\tilde{C}]^+ - [\Gamma][\tilde{C}]^- = \left| \lambda_{[\tilde{C}]} \right| [\Gamma] \quad (3.48)$$

thus the matrix  $[D]$  can be reduced to

$$[D] = \frac{3}{2}\frac{\Omega}{\Delta t}[\Gamma]^{-1}[T] + \left( \left| \lambda_{[\tilde{A}]} \right| S_1 + \left| \lambda_{[\tilde{B}]} \right| S_{i,j,k} + \left| \lambda_{[\tilde{C}]} \right| S_5 \right) [I] \quad (3.49)$$

For the preconditioning matrix applied here, the product  $[\Gamma]^{-1}[T]$  is a diagonal matrix; hence the matrix  $[D]$  is also diagonal. However,  $[D]$  is not diagonal for the control volumes in the center region of pipe, because the north face area,  $S_2$ , is zero and the matrices  $[L]$ ,  $[D]$  and  $[U]$  are changed to

$$\begin{aligned}
[L] &= -[\Gamma]^{-1} \left[ ([\Gamma][\tilde{A}]^+)_{i-1,j,k}S_3 \right. \\
&\quad \left. + ([\Gamma][\tilde{B}]^+)_{i,j-1,k}S_{i,j-1,k} + ([\Gamma][\tilde{C}]^+)_{i,j,k-1}S_6 \right] \quad (3.50)
\end{aligned}$$

$$\begin{aligned}
[D] &= [\Gamma]^{-1}[T]\frac{3}{2}\frac{\Omega}{\Delta t} + [\Gamma]^{-1} \left[ ([\Gamma][\tilde{A}]^+)_{i,j,k}S_1 - ([\Gamma][\tilde{A}]^-)_{i,j,k}S_3 \right. \\
&\quad \left. - ([\Gamma][\tilde{B}]^-)_{i,j,k}S_{i,j,k} + ([\Gamma][\tilde{C}]^+)_{i,j,k}S_5 - ([\Gamma][\tilde{C}]^-)_{i,j,k}S_6 \right] \quad (3.51)
\end{aligned}$$

$$[U] = [\Gamma]^{-1} \left[ ([\Gamma][\tilde{A}]^-)_{i+1,j,k}S_1 + ([\Gamma][\tilde{C}]^-)_{i,j,k+1}S_5 \right] \quad (3.52)$$

where the matrix  $[D]$  can be simplified as

$$[D] = \frac{3}{2}\frac{\Omega}{\Delta t}[\Gamma]^{-1}[T] + \Omega \left( \left| \lambda_{[\tilde{A}]} \right| [I]S_1 - ([\Gamma][\tilde{B}]^-)_{i,j,k}S_{i,j,k} + \left| \lambda_{[\tilde{C}]} \right| [I]S_5 \right) \quad (3.53)$$

Due to the diagonal dominance of matrix  $D$ , Eq. 3.42 was approximately factored as

$$([L] + [D])[D]^{-1}([D] + [U])\Delta\mathbf{W} = -\mathfrak{R} \quad (3.54)$$

and efficiently solved in three steps as follows:

$$\begin{aligned} \text{Step1 :} \quad & ([L] + [D])\Delta\mathbf{W}^* = -\mathfrak{R} \\ & \Delta\mathbf{W}^* = [D]^{-1}(-\mathfrak{R} - [L]\Delta\mathbf{W}^*) \\ \text{Step2 :} \quad & ([D] + [U])\Delta\mathbf{W} = [D]\Delta\mathbf{W}^* \\ & \Delta\mathbf{W} = \Delta\mathbf{W}^* - [D]^{-1}[U]\Delta\mathbf{W} \\ \text{Step3 :} \quad & \mathbf{W}^{m+1} = \mathbf{W}^m + \Delta\mathbf{W} \end{aligned}$$

Step 1 was sweeping from  $(i, j, k) = (1, 1, 1)$  lower corner of grid to  $(i, j, k) = (ni, nj, nk)$  upper corner of grid along planes of  $i + j + k = \text{constant}$ , where  $ni$ ,  $nj$  and  $nk$  are the number of the interior control volumes in the streamwise, radius and circumferential directions, respectively. By setting  $\Delta\mathbf{W}$  equal to zero at ghost cells,  $[L]\Delta\mathbf{W}^*$  was always known during the sweep and was moved to the right hand side, consequently,  $\Delta\mathbf{W}^*$  was obtained by multiplying  $[D]^{-1}$  on both sides of the equations. Similarly,  $[U]\Delta\mathbf{W}$  was also always known during the sweeping from upper corner to lower corner in step2 and moved to the right hand side. Noted here that during the these subiterations in pseudo time, the values of  $\mathbf{W}^n$  and  $\mathbf{W}^{n-1}$  were frozen in the evaluation of the the preconditioned residual. Since  $[D]$  is diagonal except for those non-Cartesian tetrahedral control volumes in the center region of pipe, the inversion of  $[D]$  in the two sweeping processes required a trivial amount work. Thus, the LU-SGS scheme is very efficient compared to other implicit schemes.

### 3.4 Convergence Criterion

For the unsteady simulations, the number of pseudo time iterations at each physical time step was limited. In this research, the maximum number of pseudo time iterations at each physical time step was 25, and finally only 4-6 psuedo time iterations were typically needed at

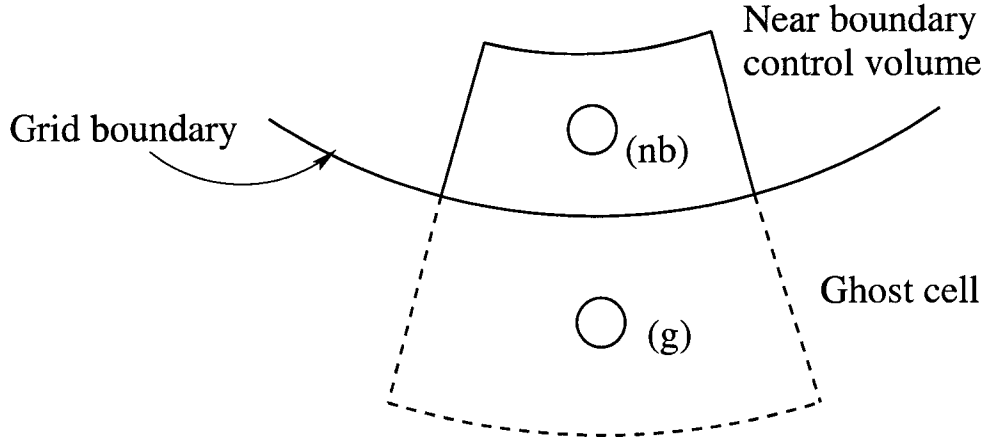


Figure 3.8 Ghost cells for boundary conditions

a physical time step. The convergence criterion of pseudo time iterations is defined as

$$\mathfrak{R}_2^{avg} = \frac{\sum_{i=1}^{n_i} \sum_{j=1}^{n_j} \sum_{k=1}^{n_k} |\mathfrak{R}_2|}{n_i \times n_j \times n_k} < TOL \quad (3.55)$$

where  $\mathfrak{R}_2$  is the second component of the preconditioned residual vector,  $\mathfrak{R}$ , corresponding to the x-direction of the momentum equation and  $TOL$  is a specified small value. Then typical value of  $TOL$  in this work is  $TOL = 1.0 \times 10^{-7}$ . As the iteration in pseudo time converged, the linearized equation, Eq. 3.32, was satisfied and primitive variable values at the current physical time step were updated by the values at pseudo time.

### 3.5 Boundary Conditions

Due to the cell center finite volume formulation, “ghost” or “image” cells, as depicted in Fig. 3.8, were needed to enforce the boundary conditions. The conditions lying on the boundaries were satisfied by setting up the proper values at ghost cells. Three boundary conditions used in this research are described here.

#### 3.5.1 Solid Wall Boundary Conditions

No slip boundary conditions were enforced for the velocity components at the solid walls as

$$u_g = -u_{nb}$$

$$v_g = -v_{nb} \quad (3.56)$$

$$w_g = -w_{nb}$$

where the subscript  $g$  denotes the ghost cell and the subscript  $nb$  denotes the near wall control volume.

Pressure was set as  $p_g = p_{nb}$  by the approximate boundary condition  $\partial p / \partial n = 0$  at the solid wall.

For heat transfer cases, two different boundary conditions were applied: fixed wall temperature or fixed wall heat flux. A fixed wall temperature,  $T_w$  was enforced by setting  $T_g = 2T_w - T_{nb}$ . To enforce the fixed nondimensional wall heat flux,  $q_w$  at the wall, the temperature at the ghost cell was set as

$$T_g = T_{nb} + \frac{q_w Re Pr}{\mu_w} \Delta l \quad (3.57)$$

where  $\Delta l$  is the distance between the cell centers of near the wall control volume and ghost cell and  $\mu_w$  is the non-dimensional molecular viscosity at the wall. For the variable property flows, the molecular viscosity at the wall is nonlinear function of the wall temperature,  $\mu_w = \mu_w(T_w)$ . An iterative procedure is needed to obtain the correct viscosity value at the wall, and hence, ghost cell temperature. The non-dimensional heat flux is given in terms of the dimensional quantities as

$$q_w = \frac{q_w^*}{\rho_{ref} V_{ref} T_{ref} c_p^*} \quad (3.58)$$

### 3.5.2 Periodic Boundary Conditions

For the isothermal cases considered in this research, the flows were assumed to be fully developed and they were simply assigned periodic boundary conditions at the inflow and outflow boundaries. The periodic boundary conditions were enforced by copying values of the variables in the boundary control volume at the outflow boundary to the ghost cell at the inflow boundary, and visa-versa. For example, the ghost cell values at the inflow boundary was set as

$$p_g = p(0, j, k) = p(ni, j, k)$$

$$\begin{aligned}
u_g &= u(0, j, k) = u(ni, j, k) \\
v_g &= v(0, j, k) = v(ni, j, k) \\
w_g &= w(0, j, k) = w(ni, j, k) \\
T_g &= T(0, j, k) = T(ni, j, k)
\end{aligned} \tag{3.59}$$

The periodicity assumption for the pressure was realized by introducing a forcing function term, which drives the flow. This issue will be discussed in the later chapters. Periodic boundary conditions were also enforced in the circumferential direction.

### 3.5.3 Step-periodic Boundary Conditions

For the heat transfer cases with property variations, due to the negative linear streamwise pressure gradient that drives the flow and the positive linear temperature gradient resulting from the heat addition, the periodicity assumptions were not valid for pressure, temperature and streamwise velocity. Step-periodic boundary conditions (Dailey and Pletcher, 1998) were adopted in this research. This is implemented by assuming that the temperature variations in the streamwise direction are step-periodic for the uniform heat flux case and the mass flux is streamwise-periodic. For example, the boundary conditions for the inlet boundary were given as

$$\begin{aligned}
p_g &= p_p(0, j, k) = p_p(ni, j, k) \\
(\rho u)_g &= (\rho u)(0, j, k) = (\rho u)(ni, j, k) \\
v_g &= v(0, j, k) = v(ni, j, k) \\
w_g &= w(0, j, k) = w(ni, j, k) \\
T_g &= T(0, j, k) = T(ni, j, k) - \Delta T_x
\end{aligned} \tag{3.60}$$

where  $p_p$  is the periodic component of the pressure,  $p = p_p + \beta x$ , and  $\beta$  is the average streamwise pressure gradient. Details of the pressure gradient calculation will be discussed in the following chapter.  $\Delta T_x$  is the average temperature difference between inflow and outflow boundaries, calculation of  $\Delta T_x$  will be discussed later.

## CHAPTER 4. RESULTS FOR THREE-DIMENSIONAL ISOTHERMAL TURBULENT FLOWS IN THIN ANNULAR AND PIPE PASSAGES

The isothermal flows in the pipe and the annulus with large ratio,  $r_{inner}/r_{outer} = 0.95$ , have been chosen as the cases with which to evaluate the present finite volume formulation. In the following sections, the simulation details of annular and pipe flow are described. The channel data from the fine grid DNS results of Kim et al. (1987), the experimental measurement of Niederschulte et al. (1990) and LES results (Dailey 1997) will be compared with LES results obtained in an annulus with very large radius ratio. The results of the pipe flow simulations will be compared with DNS data (Eggels et al. 1995) and experimental data (Westerweel et al. 1996). The friction coefficient for pipe flow will also be compared with empirical correlations.

### 4.1 Annular Flow

To evaluate the finite volume formulation based on conservation equations in Cartesian coordinates with non-Cartesian hexahedral volumes, isothermal flows in an annular passage with large radius ratio (0.95) were studied. The computational domain is shown in Fig. 4.1. Very high grid resolution in the circumferential direction would be needed to resolve the energy-carrying turbulence scale if the flow in the entire annulus was simulated. To save computational resources, the computation was conducted only in a small segment of the annulus by setting periodic boundary conditions in the circumferential direction. Since the radius ratio was very large, the annular flow could be treated as channel flow and computational domain was chosen as  $2\pi\delta \times 2\delta \times \pi\delta$  in streamwise, radius and circumferential directions, respectively. This domain was found to be adequate to contain all of the turbulent structure and produce reasonable results for planar channel flow (Tafti and Vanka 1990). The half distance between the inner

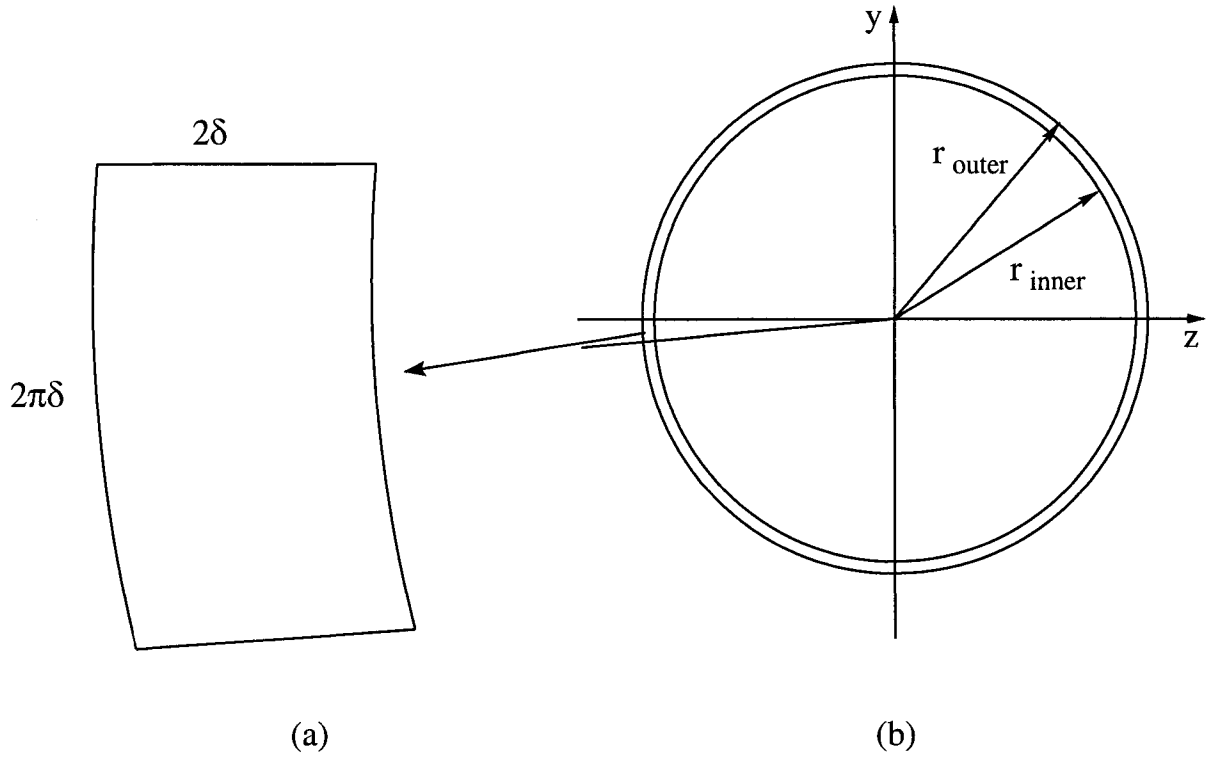


Figure 4.1 Geometry of annular: (a) cross section of computational domain, (b) cross section of annular

wall and outer wall,  $\delta$ , was used as the reference length for non-dimensionalization.

#### 4.1.1 Boundary Conditions

No-slip boundary conditions were enforced on the inner and outer walls, and the normal pressure gradient at the walls was set to zero. For the isothermal case, the temperature at the ghost cells was equal to the wall temperature which was same as the reference temperature. Periodic boundary conditions were enforced in the circumferential and streamwise directions; thus, no inflow and outflow boundary conditions were needed except for the treatment of pressure. The pressure actually was not periodic in the streamwise direction due to the negative, linear streamwise pressure gradient that drives the flow. To make the periodic assumption workable, the pressure was decomposed into periodic and aperiodic components as

$$\bar{p}(x, y, z, t) = \beta x + \bar{p}_p(x, y, z, t) \quad (4.1)$$

where  $\beta$  is the average streamwise pressure gradient. The equation of state becomes

$$\bar{\rho} = \frac{\bar{p}}{R\tilde{T}} = \frac{\beta x}{R\tilde{T}} + \frac{\bar{p}_p}{R\tilde{T}} \quad (4.2)$$

For moderate Reynolds numbers, the pressure gradient term is much smaller than periodic pressure and  $\beta x/(R\tilde{T})$  is negligible compared to  $\bar{p}_p/(R\tilde{T})$ . Therefore, the density can be approximated as

$$\bar{\rho} \approx \frac{\bar{p}_p}{R\tilde{T}} \quad (4.3)$$

By replacing  $\bar{p}$  with  $\bar{p}_p$  in the governing equation and adding the streamwise pressure gradient as a body force in the right hand side of the  $u$ -momentum equation, the periodic assumption for pressure was satisfied and the periodic pressure component was determined in the simulation by requiring that the mean mass flow rate be constant. Following the approach investigated by Benocci and Pinelli (1990), the average streamwise pressure gradient was calculated dynamically at each physical time step to provide the desired mass flow rate as

$$\beta^{n+1} = \beta^n - \frac{1}{\Delta t} \left[ \left( \frac{\dot{m}}{A_c} \right)^0 - 2 \left( \frac{\dot{m}}{A_c} \right)^n + \left( \frac{\dot{m}}{A_c} \right)^{n-1} \right] \quad (4.4)$$

where  $A_c$  is the cross-flow area of computational domain and  $\Delta t$  is the physical time step. The average mass flow rate,  $\dot{m}/A_c$  is defined as

$$\frac{\dot{m}}{A_c} = \frac{1}{A_c} \int \langle \rho u \rangle_s dA \quad (4.5)$$

where  $\langle \rangle_s$  denotes an ensemble average along the streamwise and circumferential directions.  $(\dot{m}/A_c)^0$  is the desired mass flow rate and its non-dimensional value was 1.0.

#### 4.1.2 Simulation Details

The initial flow field was constructed by superimposing random velocity fluctuations on a mean velocity that matched with the DNS channel flow results of Kim et al. (1987). The target bulk Reynolds number based on  $\delta$  is given as

$$Re_\delta = \frac{\rho_b u_b \delta}{\mu_b} = 2800 \quad (4.6)$$

where the bulk density and velocity are defined as

$$\rho_b = \frac{1}{A_c} \int \rho dA \quad (4.7)$$

$$u_b = \frac{1}{\rho_b A_c} \int \rho u dA \quad (4.8)$$

The Mach number was 0.001 and non-dimensional physical time step was 0.01. The simulation was made with  $48 \times 64 \times 48$  grid resolution in the streamwise, radial and circumferential directions, respectively. The grid was uniform in both streamwise and circumferential directions, but was clustered toward to the walls using algebraic hyperbolic tangent stretching in the radius direction, where

$$y_j = |r_j| \sin[\pi + (j - 1)\theta] \quad (j = 1, \dots, m_j) \quad (4.9)$$

$$z_j = |r_j| \cos[\pi + (j - 1)\theta] \quad (4.10)$$

$$\theta = \frac{\pi}{40(m_k - 1)} \quad (4.11)$$

$$r_j = r_a \frac{\tanh(a\xi_j)}{\tanh(a)} + r_b \quad (4.12)$$

$$\xi_j = -1 + 2 \frac{j - 1}{m_j - 1} \quad (4.13)$$

$$a = \frac{1}{2} \ln \left( \frac{1 + b}{1 - b} \right) \quad (4.14)$$

$$r_a = \frac{1}{2}(r_{outer} - r_{inner}) \quad (4.15)$$

$$r_b = \frac{1}{2}(r_{outer} + r_{inner}) \quad (4.16)$$

The parameter  $b$  is to control how far the grid will stretch to the walls, and typical values are between 0.7 and 0.95 here. The parameters  $m_i$ ,  $m_j$  and  $m_k$  are the vertex numbers in the streamwise, radius and circumferential directions, respectively. The control volume dimension in the circumferential direction varies linearly with radius and reaches the maximum value at the outer wall and minimum value at the inner wall. In the current simulation, the maximum circumferential dimension was 0.0654 with respect to  $\delta$ , or 11.73 in wall units. The minimum circumferential dimension was 0.0622 with respect to  $\delta$ , or 11.16 in wall units. The control volume dimension in the streamwise direction was 0.131 with respect to  $\delta$ , or 23.51 in wall

units. The minimum spacing in the radial direction was 0.0066 with respect to  $\delta$ , or 1.19 in wall units. The maximum spacing in the radial direction was 0.0461 with respect to  $\delta$ , or 8.26 in wall units. The dynamic SGS model was used in the simulation. The simulation was run with 5 processors on the Origin machines.

When the simulation was first started, the flow laminarized and the average turbulent kinetic energy,  $k^+$ , dropped to a small value, where  $k^+$  is normalized by the square of the friction velocity as defined later. The friction velocity  $u_\tau$  also decreased to a small value. However, after around 10,000 steps, the  $k^+$  increased sharply to maximum value near 6 and then kept on decreasing and finally fluctuated about 2.1. The  $u_\tau$  also kept on increasing and fluctuating about  $u_\tau \approx 0.064$ . Once the flow was deemed to be statistically steady, statistics were collected by running for an additional 5000-10000 time steps.

#### 4.1.3 Results for Mean Flow and Velocity Statistics

The mean velocity profiles and velocity statistics were compared with the DNS, experimental, and LES results of planar channel flow due to the very high ratio of inner radius to outer radius. The DNS results of Kim et al. (1987) were obtained by directly solving the incompressible unsteady Navier-Stokes equations with no subgrid-scale model. The nondimensional computational domain was  $4\pi \times 2 \times 2\pi$  with  $192 \times 129 \times 160$  grid point in the  $x$ ,  $y$  and  $z$  directions, respectively. The computational domain and grid for the LES of Dailey (1997) were the same as that of the present simulation. The Reynolds number of both the DNS and LES was  $Re_\delta = 2800$ , the same as the present simulation. The experiments of Niederschulte et al. (1990) were performed specifically to examine the accuracy of Kim et al.'s DNS results. Their Reynolds number was  $Re_\delta = 2457$  and  $2777$  for two different cases.

The mean streamwise velocity profile in global coordinates is shown in Fig. 4.2. The mean profile denoted by  $\langle \rangle$  was obtained by averaging in the homogeneous directions (streamwise and circumferential directions here) and in time for 10,000 time steps. In the figure, the mean velocity profile was normalized by the friction velocity as  $u^+ = u/u_\tau$ , where  $u_\tau = \sqrt{\tau_w/\rho_w}$ . The  $x$ -axis label,  $r - (r_{outer} + r_{inner})/2$ , was non-dimensionalized with respect to  $\delta$ , and was

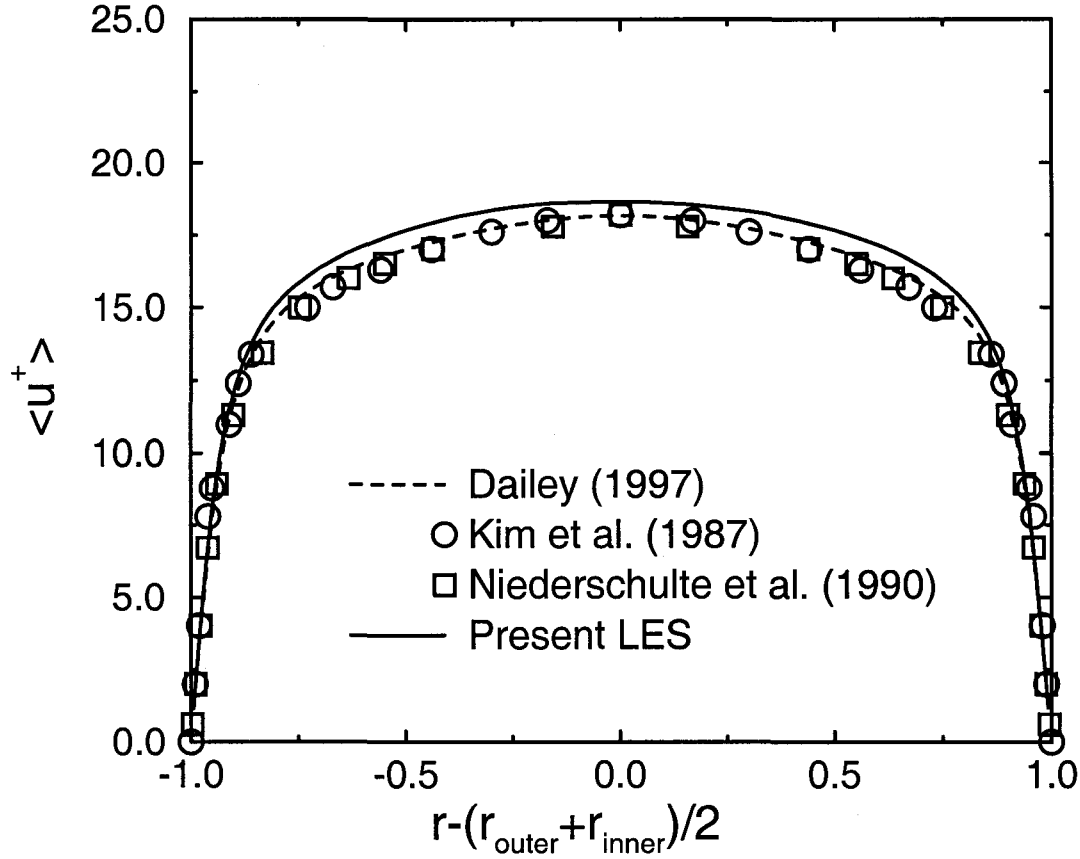


Figure 4.2 Mean velocity profile in global coordinates

defined as

$$\begin{aligned}
 r - \frac{r_{outer} + r_{inner}}{2} &= \frac{r^* - \frac{r_{outer}^* + r_{inner}^*}{2}}{\frac{r_{outer}^* - r_{inner}^*}{2}} \\
 &= \frac{r^* - \frac{r_{outer}^* + r_{inner}^*}{2}}{\delta}
 \end{aligned} \tag{4.17}$$

where the dimensional value was denoted by the superscript '\*'.

As shown, very good agreement with the DNS and experimental results was achieved in the near wall region, but the present results were slightly higher than the reference data in the central region. The mean streamwise velocity profile in wall coordinates is shown in Fig. 4.3. The dash-dot lines in the figure represent the law of the wall through the empirical correlations. The viscous sublayer was well resolved yielding the linear velocity distribution  $u^+ = y^+$ . In

the far region, where the logarithmic law of the wall is represented by  $u^+ = \frac{1}{\kappa} \ln y^+ + 5.5$  with von Kármán's constant  $\kappa = 0.4$ , the annular mean velocity profile is slightly above the DNS and experimental profiles.

Turbulent fluctuations with respect to the Reynolds average are denoted with a single prime,  $'$ , and the turbulent fluctuations with respect to the Favre ensemble average are denoted with a double prime,  $''$ . Following the nomenclature of Huang et al. (1995), the Reynolds average of a quantity is denoted as  $\langle \rangle$ , the Favre ensemble average is denoted as  $\{ \}$  and defined as

$$\{f\} = \langle \rho f \rangle / \langle \rho \rangle \quad (4.18)$$

Because this simulation case was nearly incompressible and isothermal, the density fluctuations were assumed to be small enough that the Reynolds and Favre average were essentially equivalent. The velocity fluctuations were obtained at each time step by

$$u'_i = u_i - \langle u_i \rangle_s \quad (4.19)$$

where  $\langle \rangle_s$  denotes a spatial average in the streamwise and circumferential directions in this simulation case.

The ensemble averaged root-mean-square (rms) values were calculated as, for example

$$u'_{rms} = \sqrt{\langle u'^2 \rangle} \quad (4.20)$$

where  $\langle \rangle$  denotes an average in the streamwise and circumferential directions and in time. Consequently, the average turbulent kinetic energy is given by

$$k = \frac{1}{2} \langle u'_i u'_i \rangle \quad (4.21)$$

and  $k^+ = k/u_\tau^2$ .

The  $uu_r$  velocity cross-correlation coefficient,  $R(uu_r)$ , was calculated as

$$R(uu_r) = \frac{\langle u' u'_r \rangle}{u'_{rms} u'_{r_{rms}}} \quad (4.22)$$

As shown in Fig. 4.4, very good agreement is observed between the present results, DNS and experimental results except for a slight difference near the wall.

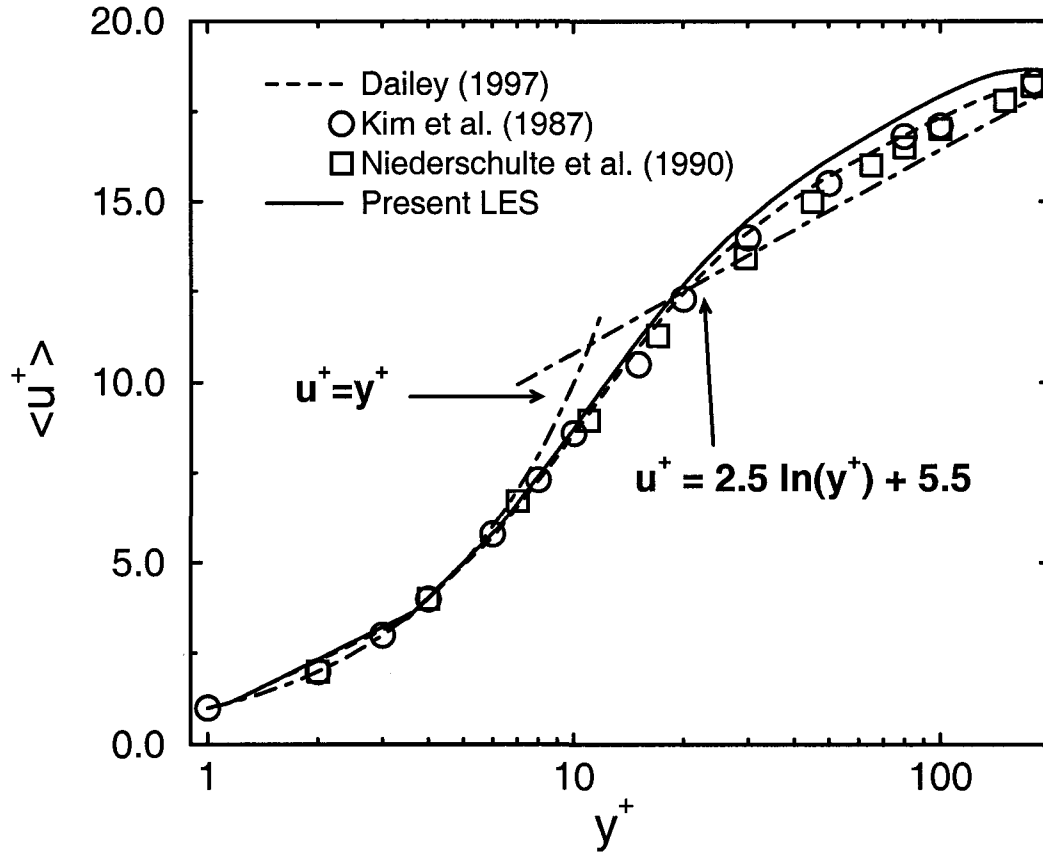


Figure 4.3 Mean velocity profile in wall coordinates

The *rms* velocity fluctuations are shown in Fig. 4.5. Excellent agreement with DNS and experimental data was achieved for both  $u_{rms}$  and  $u_{r,rms}$ , the same trend as the DNS data for  $u_{\theta,rms}$  was captured. The profiles of the *rms* velocity fluctuations are slightly asymmetric. The asymmetric profile may be due to the differing surface areas of the inner and outer walls of the annulus.

The skewness is the third order moment that represents the asymmetry of the probability density distribution for the velocity fluctuations. It is given as

$$S(u_i) = \frac{\langle u_i'^3 \rangle}{u_{i,rms}^3} \quad (4.23)$$

The resulting skewness factors for velocity fluctuations are shown in Fig. 4.6. More deviations are observed comparing with the DNS and experimental results. The tendency of skewness of

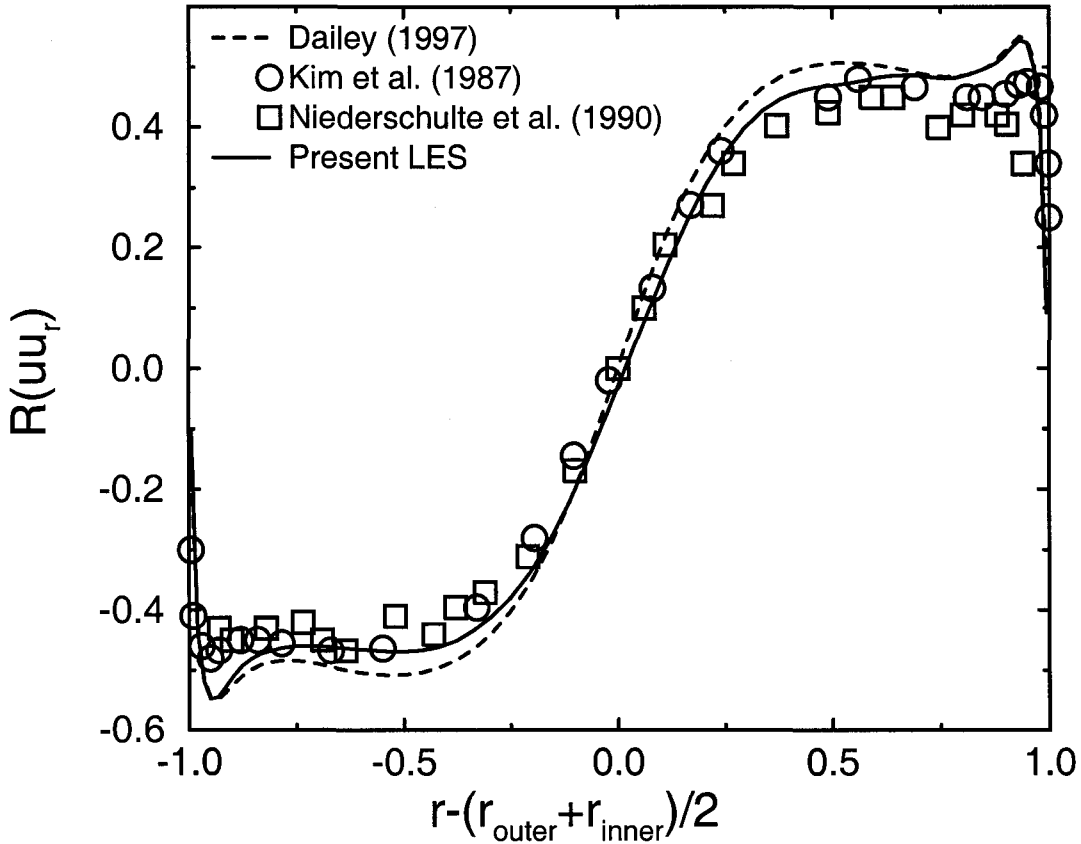


Figure 4.4 Velocity cross-correlation coefficient

the streamwise velocity fluctuations is similar to DNS and experimental data, with positive skewness near the wall and negative skewness in the other regions. The skewness factor of the circumferential component of velocity should be zero due to symmetry, but the figure shows some oscillations near zero. From the definition, the skewness factor of the normal-to-wall velocity fluctuations is related to the a normal-to-the-wall energy flux by radial velocity fluctuations. In the annular flow, this energy flux is positive ( $S > 0$ ) near the walls, thus the energy is transported away from the walls.

The fourth order moment is called flatness (or kurtosis) which is a measure of whether the probability density distribution for the velocity fluctuations is peaked or flat relative to a Gaussian distribution. The value of the flatness is large if the velocity fluctuation frequently

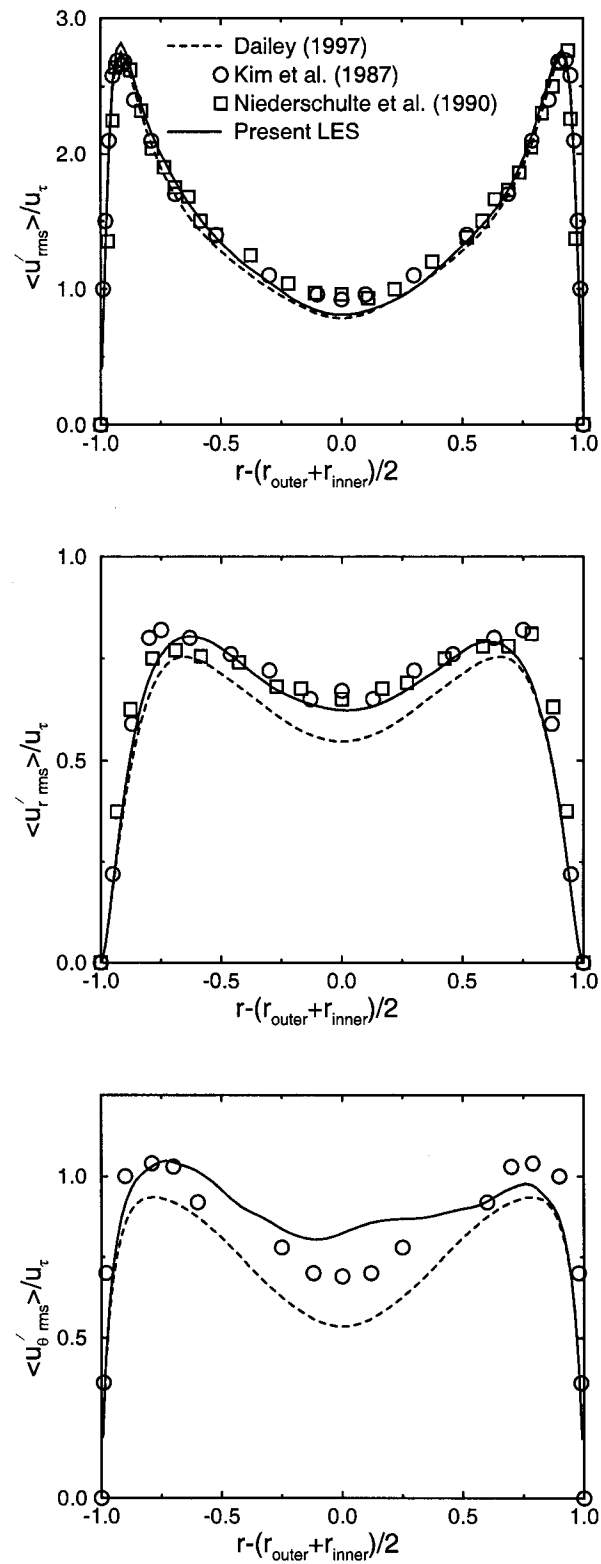


Figure 4.5 Root-mean-square of velocity fluctuations normalized by wall friction velocity

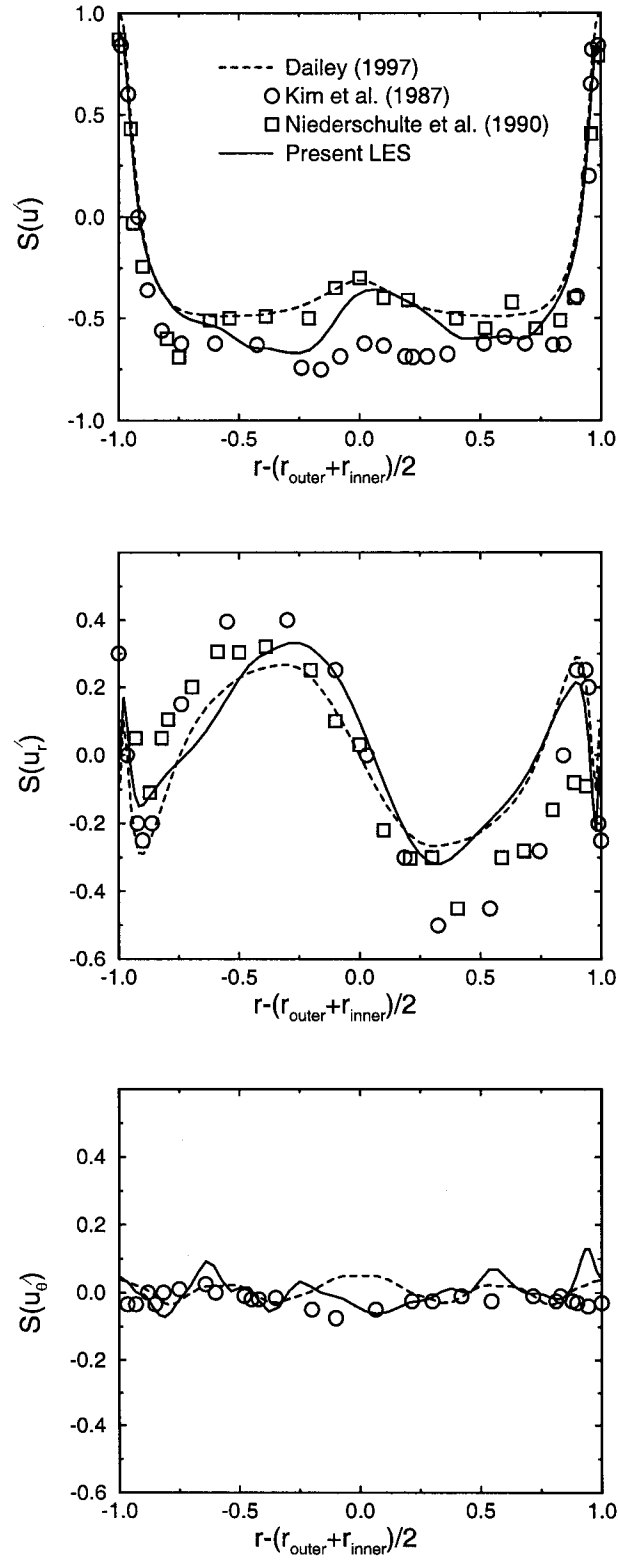


Figure 4.6 Skewness factor of the velocity fluctuations

takes on the values far away from its *rms* value. The flatness is calculated by

$$F(u_i) = \frac{\langle u_i'^4 \rangle}{u_{i,rms}'^4} \quad (4.24)$$

The flatness factors for velocity fluctuations are shown in Fig. 4.7. Large flatness values are obtained near the walls, and the flatness is a little larger than the corresponding value of 3 for a Gaussian distribution in the regions away from the walls. As for skewness, more discrepancies for flatness are found between the present results and the reference data, but the overall comparisons of the higher order statistics are reasonably good.

All the present comparisons must rely on the assumption that the subgrid-scale contributions to the statistics is much smaller than the resolved contribution, because the small scale contribution to the LES statistics is not accounted for in this calculation.

The turbulent kinetic energy is shown in Fig. 4.8 and Fig. 4.9 normalized by the square of the bulk velocity and the square of the friction velocity, respectively. The same trends were observed as for the *rms* values.

#### 4.1.4 Instantaneous Vector Plot

The instantaneous velocity vector plot in the cross section is shown in Fig. 4.10; large scale motions near the walls were captured successfully in the present simulation.

## 4.2 Pipe Flow

Before simulating turbulent pipe flows with heat transfer, fully developed isothermal turbulent pipe flows were simulated to evaluate the present finite volume formulation for this geometry. The computational domain is shown in Fig. 4.11, where the radius of the pipe is denoted by  $r$ , and the length of the computational domain by  $L$ , where  $L = 10r$ . All the dimensions were normalized by the pipe radius  $r$ . The length of the computational domain, which should be long enough to include the largest scale structures, was chosen with the guidance of DNS simulations (Unger and Friedrich 1993, Eggels 1994). The advantages of solving the conservation equations resolved in the Cartesian coordinate system include the following.

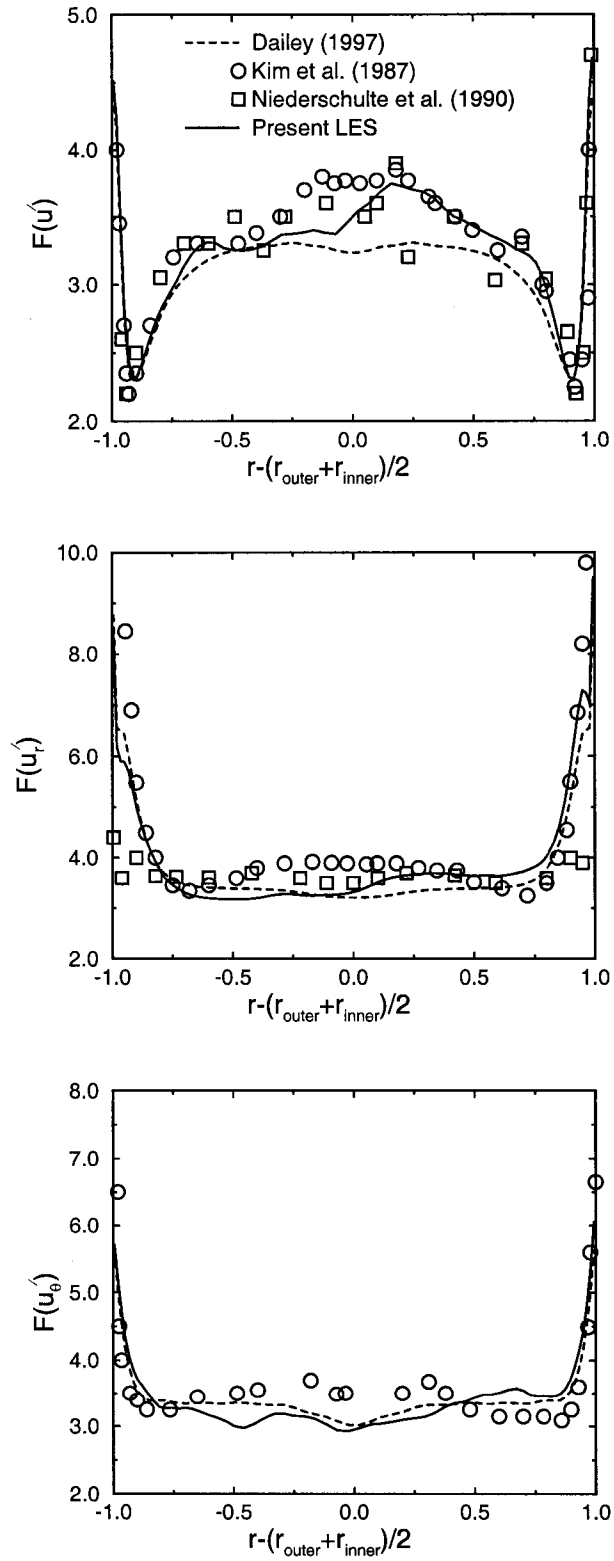


Figure 4.7 Flatness factor of the velocity fluctuations

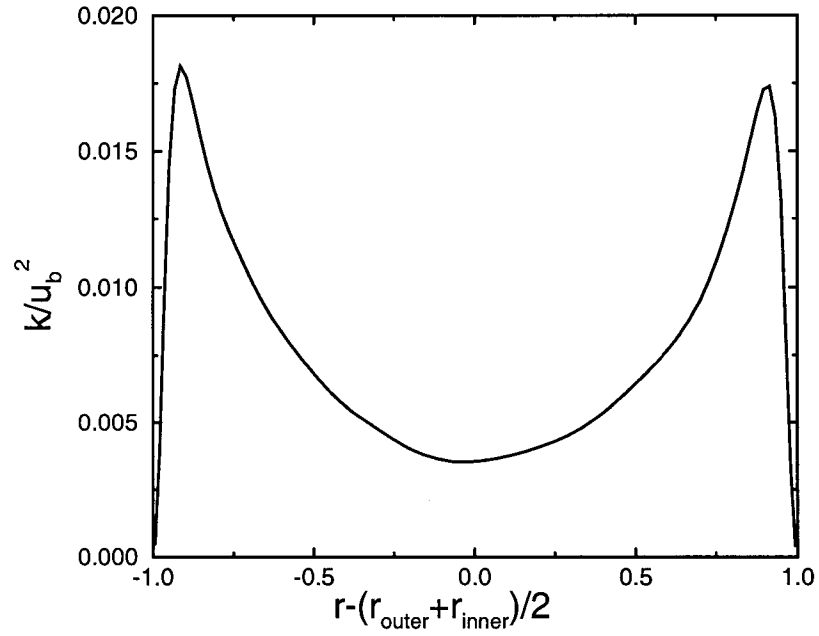


Figure 4.8 Turbulent kinetic energy scaled by bulk velocity in global coordinates

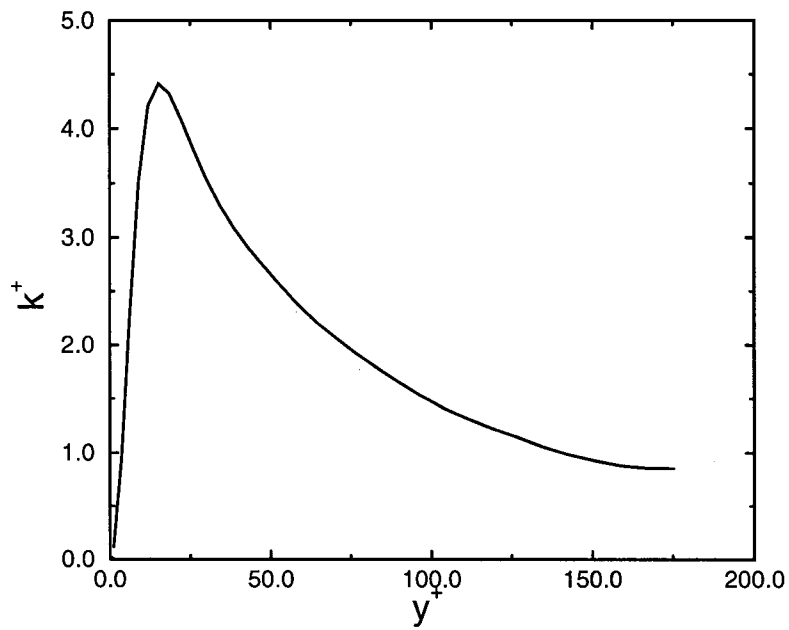


Figure 4.9 Turbulent kinetic energy in wall coordinates

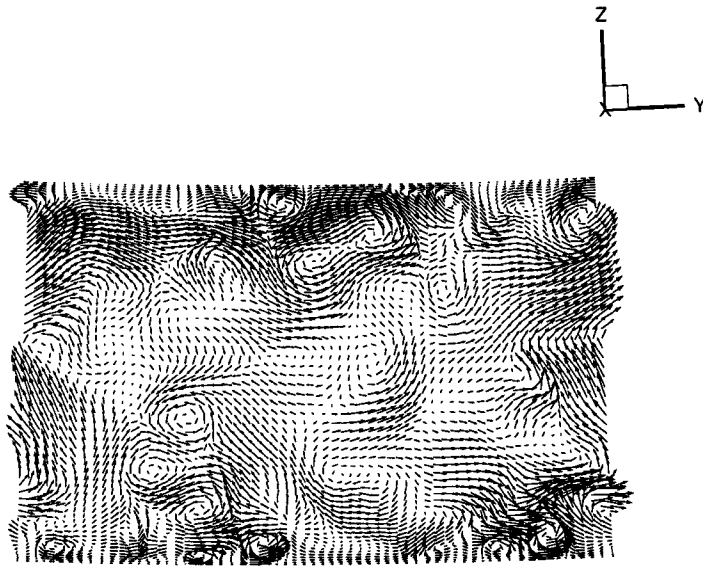


Figure 4.10 Instantaneous vector plot of  $u_r$  and  $u_\theta$  in cross section

First, the Cartesian based equations are as simple as possible and can be put in strong conservation (or divergence) form. This generally helps toward maintaining accuracy since using the alternative coordinate-oriented systems such as the cylindrical or polar systems require that the basis vectors change directions. This introduces an “apparent force” to cause the turning that is non-conservative in form and hard to represent accurately. Second, the equations in the cylindrical and polar systems contain singularities at the coordinate origin. It is true that grid-related singularities may also occur when the Cartesian-based equations are used, but these are usually easier to accommodate than singularities in the equations themselves. It is generally accepted that there is no advantage to using equations represented in the cylindrical or polar coordinate systems for numerical computations if the flows are three-dimensional in nature (Ferziger, and Peric 1996).

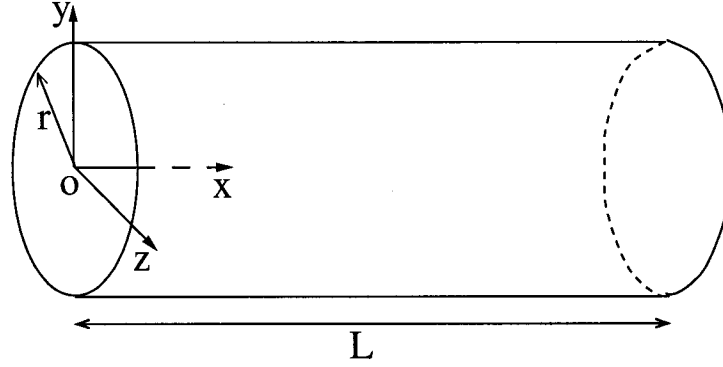


Figure 4.11 Pipe flow geometry and coordinate system

#### 4.2.1 Boundary Conditions

No-slip boundary conditions were enforced on the wall, and the normal pressure gradient at the wall was set to zero. Periodic boundary conditions were enforced in the circumferential and streamwise directions, and no boundary conditions were needed at the center line of the pipe. To simulate the isothermal flow, the temperature at the ghost cells was set equal to the wall temperature. As for annular flow, the forcing function was used to validate the periodic pressure assumption in the streamwise direction. For the fully developed pipe flow, the mean pressure gradient should equal to  $2u_\tau^2/r$  in dimensional form, and equals 2 when scaled by  $u_\tau$  and  $r$ .

#### 4.2.2 Simulation Details

The simulations were designed to match the flow conditions of the available experimental and DNS results. The DNS computations were performed by Eggels et al. (1994), and the laser Doppler anemometry (LDA) and particle image velocimetry (PIV) measurements were performed by Westerweel et al. (1996). The computations are initiated from randomly generated fields similar to the annular flow simulations. The target bulk Reynolds number based on hydraulic diameter is given as

$$Re_D = \frac{\rho_b u_b D}{\mu_b} = 5300 \quad (4.25)$$

where  $D$  is the diameter of the pipe. The Mach number was 0.001 and the non-dimensional physical time step was 0.01.

To study the grid independence, simulations were performed with three different grid resolutions,  $48 \times 32 \times 64$ ,  $64 \times 40 \times 80$  and  $48 \times 32 \times 100$  grid points in the streamwise, radial and circumferential directions, respectively. It was found that the grid resolution,  $64 \times 40 \times 100$ , was fine enough to solve the large scale field and the effect by refining the grid in the circumferential depiction was more efficient in improving the accuracy than in the other two directions. Grids were uniform in both the streamwise and circumferential directions, but clustered toward to the wall using the algebraic hyperbolic tangent stretching in the radial direction, where

$$y_j = |r_j| \sin[\pi + (j - 1)\theta] \quad (j = 1, \dots, m_j) \quad (4.26)$$

$$z_j = |r_j| \cos[\pi + (j - 1)\theta] \quad (4.27)$$

$$\theta = \frac{\pi}{m_k - 1} \quad (4.28)$$

and  $r_j$  was calculated by

$$r_j = r_a \frac{\tanh(a\xi_j)}{\tanh(a)} + r_b \quad (j = 1, \dots, 2m_j - 1) \quad (4.29)$$

$$\xi_j = -1 + 1 \frac{j - 1}{m_j - 1} \quad (4.30)$$

$$a = \frac{1}{2} \ln \left( \frac{1 + b}{1 - b} \right) \quad (4.31)$$

$$r_a = -1 \quad r_b = 1 \quad (4.32)$$

The parameter  $b$  is to control how far the grid will stretch to the wall, and a typical value was between 0.7 and 0.95 here. The parameters  $m_i$ ,  $m_j$  and  $m_k$  are the vertex numbers in the streamwise, radial and circumferential directions, respectively. The two types of control volumes, hexahedral and tetrahedral, are shown in Fig. 3.3 and Fig. 3.5, respectively. The control volume dimensions in the streamwise and radial directions are given in Table 4.1 with respect to the radius and in wall coordinates. The superscript,  $+$  represents a quantity in wall units, where in terms of nondimensional variables,  $x^+ = Re_{ref} u_{\tau} x / \nu_w$ , where  $Re_{ref}$  is the reference Reynolds number and is defined as  $Re_{ref} = \rho_{ref} u_{ref} L_{ref} / \mu_{ref}$ . The control volume

Table 4.1 Control volume dimensions in streamwise and radial directions

Grid	Streamwise spacing		Radius spacing			
	$\Delta x$	$\Delta x^+$	$\Delta r_{min}$	$\Delta r_{min}^+$	$\Delta r_{max}$	$\Delta r_{max}^+$
$48 \times 32 \times 64$	0.208	34.715	0.0087	1.45	0.0539	8.981
$64 \times 40 \times 80$	0.1563	26.955	0.0063	1.087	0.0446	7.694
$64 \times 40 \times 100$	0.1563	27.85	0.0063	1.123	0.0446	7.948

dimension in the circumferential direction varied linearly with radius and the maximum and minimum spacings are given in Table 4.2.

Table 4.2 Control volume dimensions in circumferential direction

Grid	Circumferential spacing			
	$(r\Delta\theta)_{min}$	$(r\Delta\theta)_{min}^+$	$(r\Delta\theta)_{max}$	$(r\Delta\theta)_{max}^+$
$48 \times 32 \times 64$	0.0053	0.8818	0.0982	16.359
$64 \times 40 \times 80$	0.0035	0.6038	0.0785	13.549
$64 \times 40 \times 100$	0.0028	0.4994	0.0628	11.197

All the simulations were run with dual time stepping and preconditioning with the LU-SGS scheme using 9 processors on the Origin machines. The dynamic SGS model was used in the simulations. When the simulations were first started, the viscous dissipation was large which removed the initial velocity fluctuations and laminarized the flow. The average turbulent kinetic energy,  $k^+$ , dropped to a small value, and the friction velocity  $u_\tau$  also decreased to a small value. However, after several thousand steps, the  $k^+$  increased sharply to a maximum value, then kept on decreasing and finally fluctuated about a constant value. Also, the fluctuating increment of  $u_\tau$  finally fluctuated around a constant value too. The total shear stress profile versus  $r/D$  was almost a straight line when the flow became statistically steady; after that, statistics could be collected by running for an additional 5000-10000 time steps.

Table 4.3 Mean flow properties of LES, DNS and experiments

	LES(Coarser)	LES(Coarse)	LES(Fine)	DNS	PIV	LDA
$Re_\tau = u_\tau D/\nu$	333	345	356	360	366	371
$u_b/u_\tau$	15.9	15.36	14.86	14.73	14.88	14.68
$u_c/u_\tau$	20.47	19.95	19.14	19.31	19.38	19.39

### 4.2.3 Results of Turbulence Statistics

In this section, ensemble averaged results are presented and compared with the DNS and experimental results. The DNS results of Eggels et al. (1994) were obtained by directly solving the incompressible unsteady Navier-Stokes equations using cylindrical coordinates. The equations were discretized by means of the finite volume technique with a staggered grid. The computational domain was  $10r \times r \times 2\pi$  with grid resolution  $256 \times 96 \times 128$  in the streamwise, radial and  $\theta$  directions, respectively. The same bulk Reynolds number, 5300, as in the present simulation was used in the DNS. The bulk Reynolds number of the experiments performed by Westerweel et al. (1996) was 5450.

#### 4.2.3.1 Mean Flow Properties

Some mean flow properties of the LES, DNS, and experiments are listed in the Table 4.3, where  $u_c$  is the centerline velocity. As shown, the friction velocity of the two coarse grids was under-predicted, while the agreement between the results of fine grid and DNS and experimental results was within a few percent. The mean streamwise velocity profile normalized by friction velocity is show in Fig. 4.12. The linear velocity distribution  $u^+ = y^+$  for  $y^+ < 5$  was well resolved with all the coarse and fine grids. For the region where  $y^+ > 30$ , the logarithmic velocity distribution represented by  $u^+ = 2.5 \ln y^+ + 5.5$  was not exactly followed by both the numerical simulations and experiments. Patel and Head (1969) also observed that the flow in pipe fails to conform to the accepted law of the wall even at Reynolds number considerably above 3000. Laufer (1954) and Lawn (1971) demonstrated that only for a Reynolds number much larger than the present one, does the turbulent pipe flow exhibit a logarithmic velocity

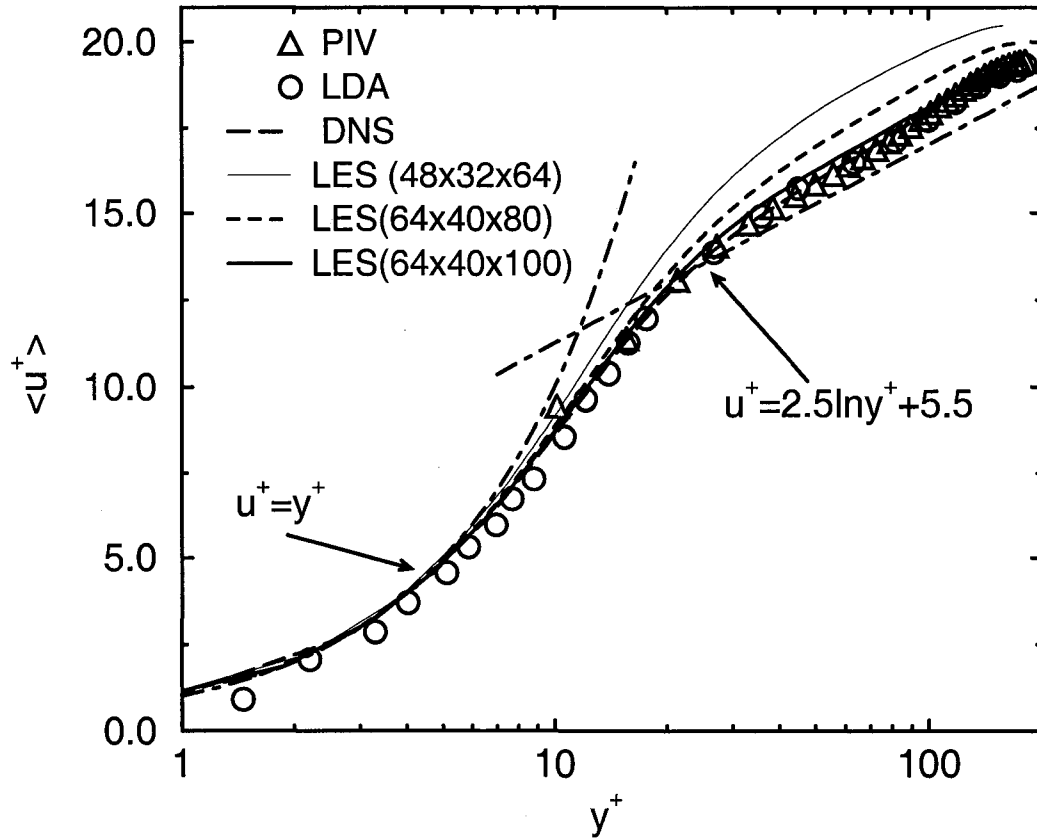


Figure 4.12 Mean streamwise velocity profile in wall coordinates

distribution, at least in part of the cross section. However, the fine grid results agreed very well with the DNS and experimental results. Large differences were observed between the results of both coarse grids and the DNS and experimental results.

#### 4.2.3.2 Turbulent Intensities and High Order Statistics

The root-mean-square (*rms*) values of fluctuating velocities, normalized by the friction velocity, are shown in Fig. 4.13 and are compared with the DNS and experimental data. The measurements of circumferential velocity fluctuations from PIV and LDA are not available. Use of both coarse grids resulted in overprediction of  $u_{rms}$  and underprediction of  $u_{r,rms}$  and  $u_{\theta,rms}$ . For the fine grid, good agreement was achieved near the wall region, but both DNS and LES data underpredicted the  $u_{rms}$  near the core region. According to Tennekes and Lumley

(1972), the turbulent intensities should drop to about  $0.8u_\tau$  in the core region which is evident in the present *rms* profiles.

The skewness and flatness factors for the velocity fluctuations are shown in Fig. 4.14 and Fig. 4.15, respectively. The discrepancies between the LES and DNS results and experiments are larger than before; however, reasonable overall agreement between present data and DNS and experimental statistics was obtained.

#### 4.2.3.3 Shear Stress

The shear stress contributions were calculated by

$$\tau_{res} = - \langle \rho u' u_r' \rangle \quad (4.33)$$

$$\tau_{vis} = - \langle \frac{\mu}{Re} \frac{\partial u}{\partial r} \rangle \quad (4.34)$$

$$\tau_{sgs} = - \langle \mu_t \frac{\partial u}{\partial r} \rangle \quad (4.35)$$

where  $\tau_{res}$  is the resolvable Reynolds shear stress,  $\tau_{vis}$  is the viscous shear stress, and  $\tau_{sgs}$  is the modeled SGS stress. The shear stress contributions are shown in Fig. 4.16. The viscous shear stress is small near the core region and hence the Reynolds shear stresses with all three grid resolutions is similar near the core region. The viscous shear stress becomes important near the wall and the different Reynolds shear stress distributions are induced by the different grid resolutions. As shown, the coarse grids gave underprediction of the resolvable Reynolds shear stress and overprediction of the viscous shear stress near the wall. No DNS and experimental data are available for the modeled SGS stress. In the present simulations, the coarse grids result in larger modeled SGS stress than the fine grid in the near wall region. The profiles of Reynolds shear stress and the viscous shear stress with the fine grid matched very well with the DNS and experimental data.

The sum of the three shear stress contributions is the total shear stress and is shown in Fig. 4.17. Since the flow is fully developed and in a statistically steady state, the total shear stress must be linear, which was observed in the present simulations. It should be noted here that the linear distribution is independent of the grids, because the normal-to-the-wall gradient

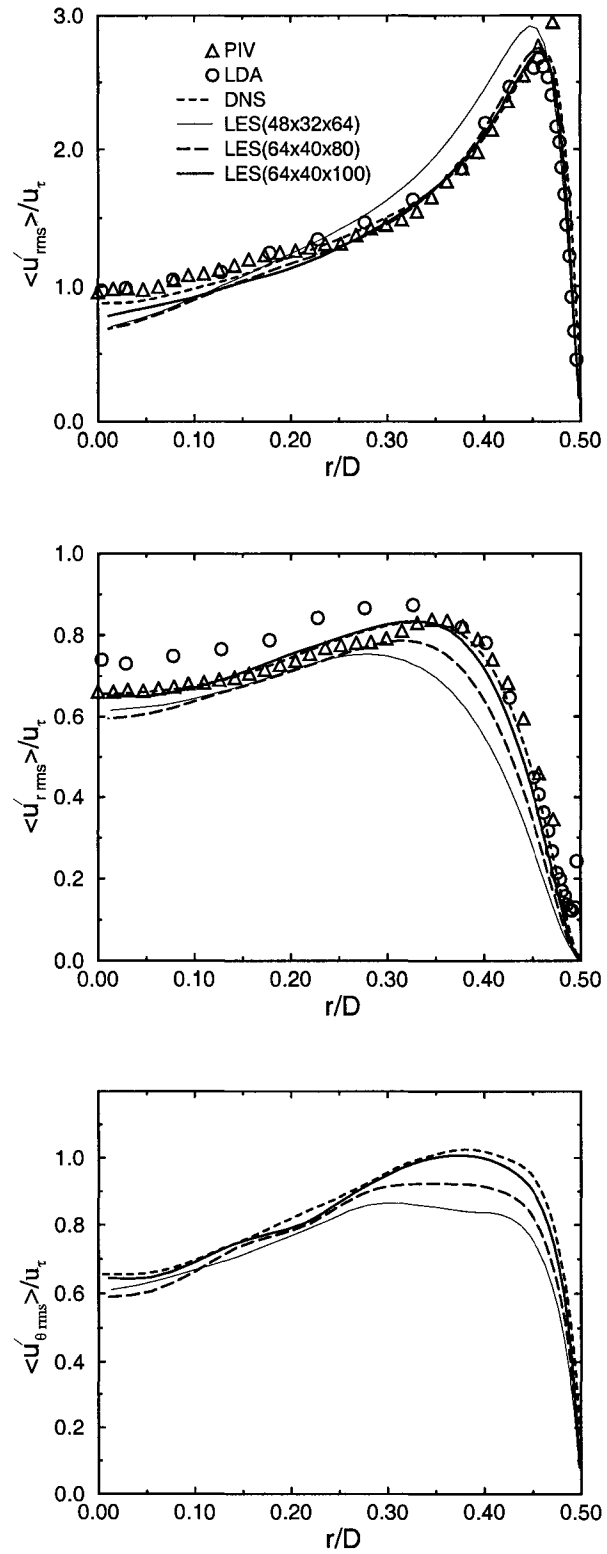


Figure 4.13 RMS velocity fluctuations normalized by wall friction velocity

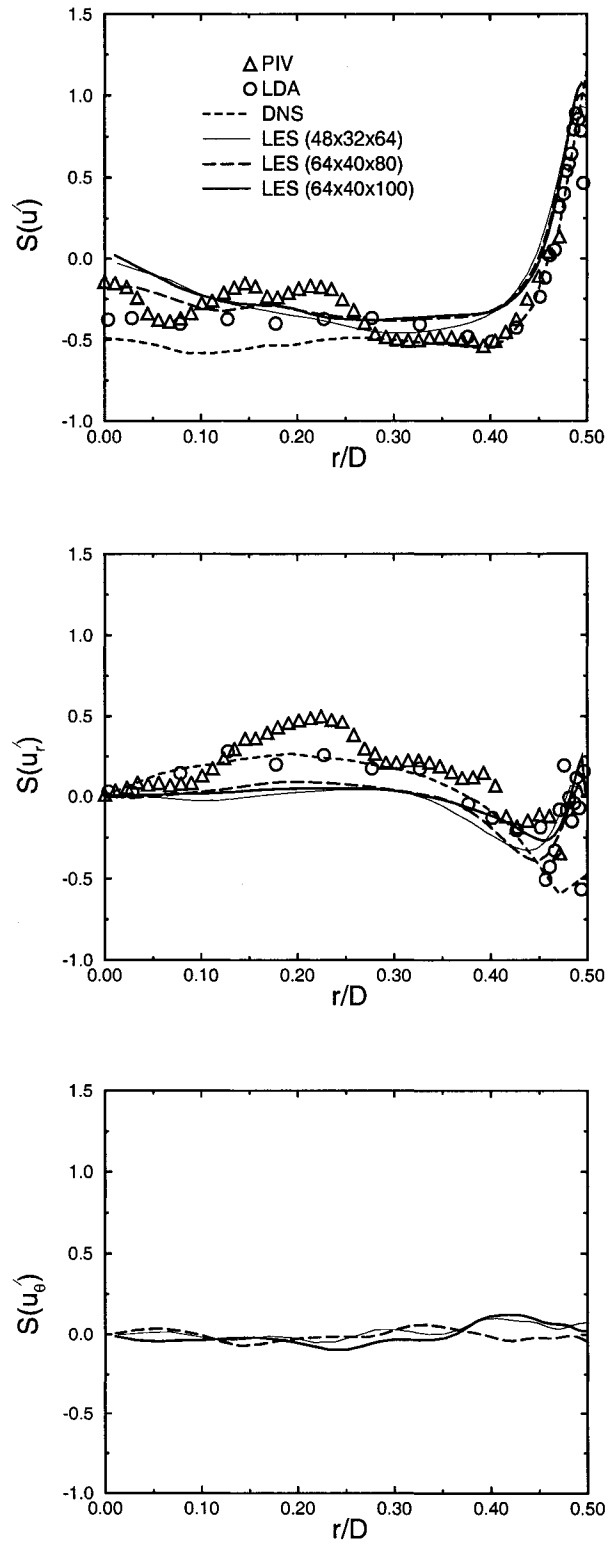


Figure 4.14 Skewness factor of the velocity fluctuations

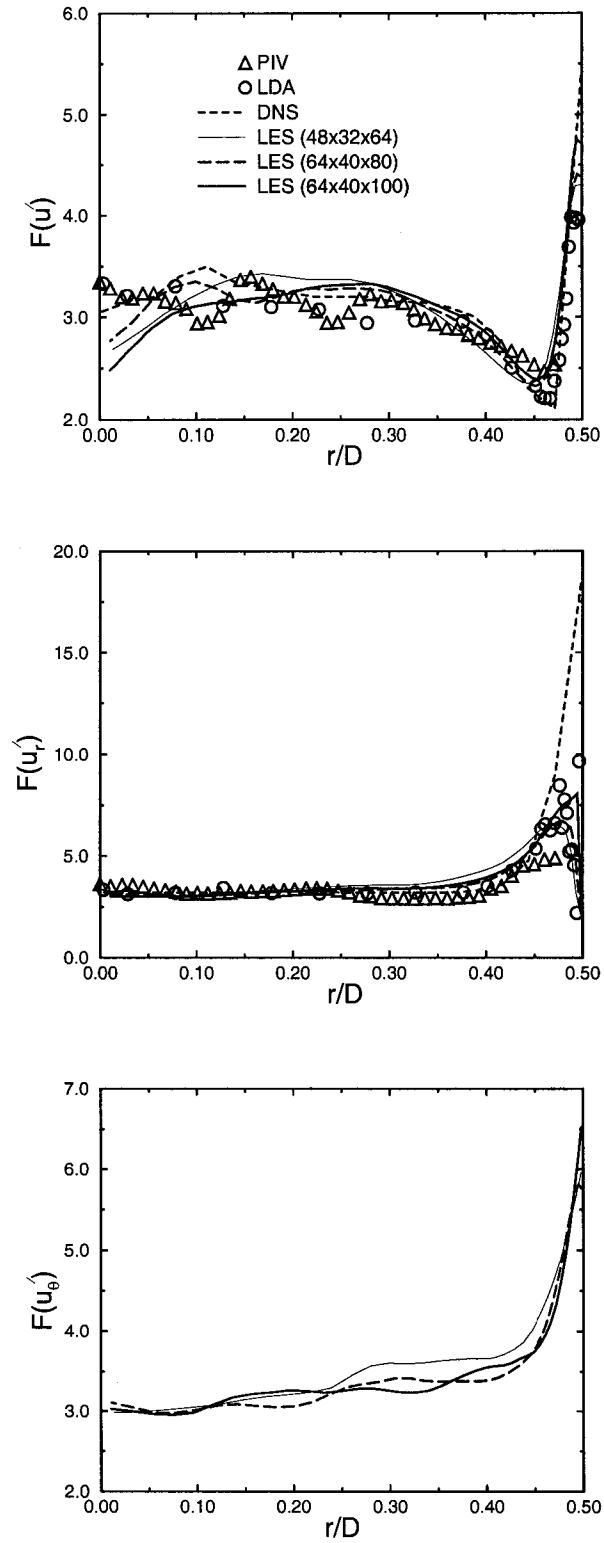


Figure 4.15 Flatness factor of the velocity fluctuations

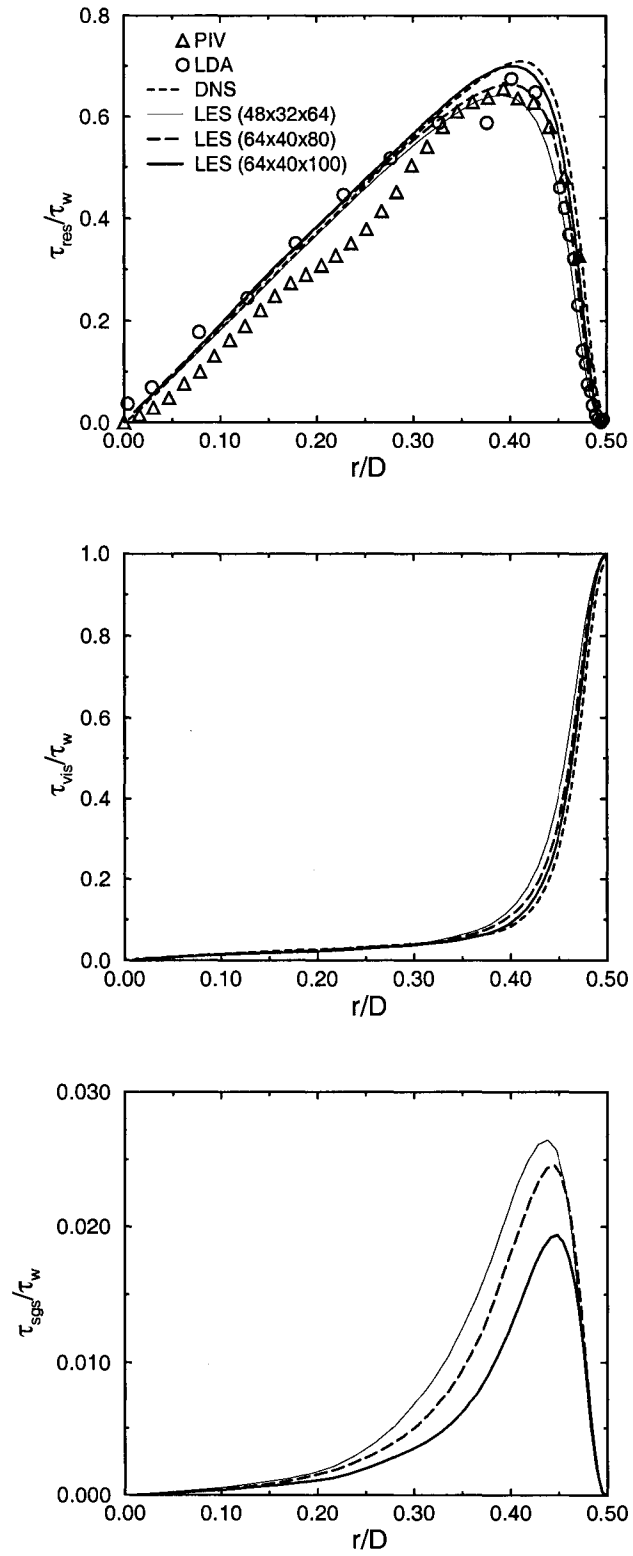


Figure 4.16 Shear stress distributions scaled by wall shear stress

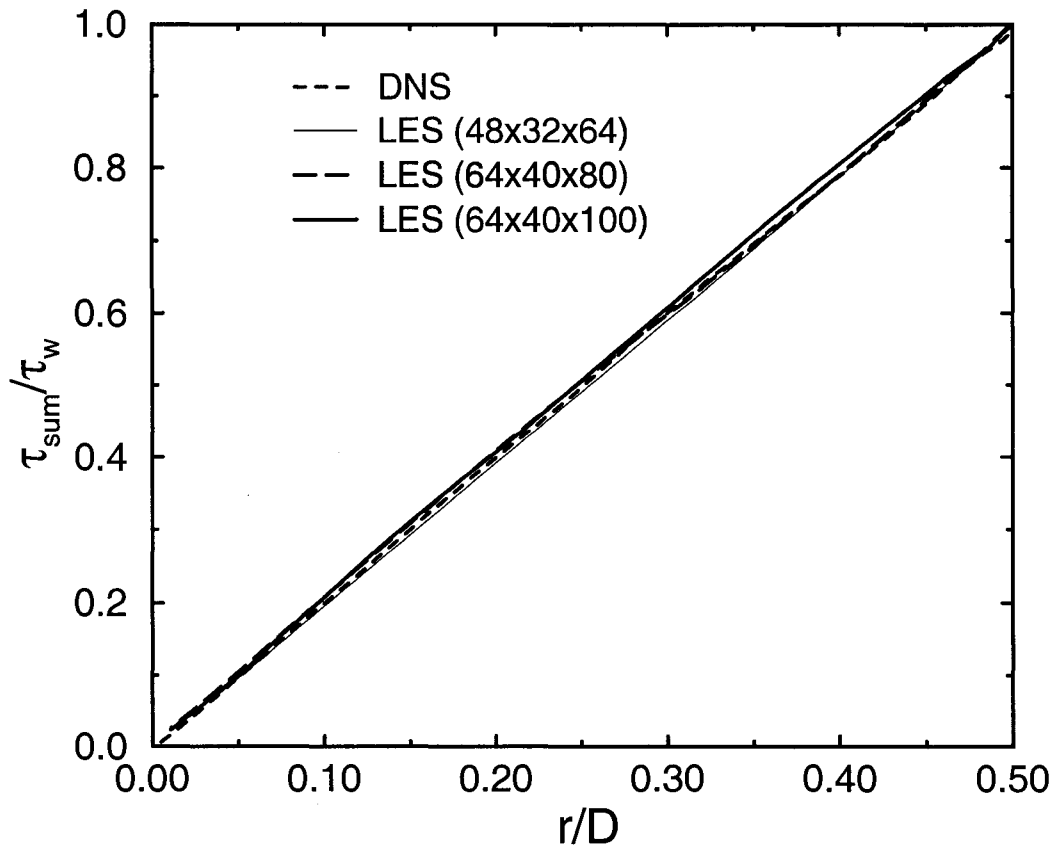


Figure 4.17 Total shear stress distribution scaled by wall shear stress

of total shear stress must balance the pressure gradient, which is a fixed value for the fully developed flow.

#### 4.2.4 Instantaneous Results

In this section, all the results were obtained using the fine grid. The nondimensional instantaneous velocity vector plot is shown in Fig. 4.18. Large scale eddies were successfully captured near the wall. The contours of nondimensional instantaneous streamwise velocity in the cross section are shown in Fig. 4.19. The figure shows more isotropic structures near the core region of the pipe. The low-speed streaky structure in the near wall region,  $y^+ = 4.7$ , is clearly evident in Fig. 4.20.

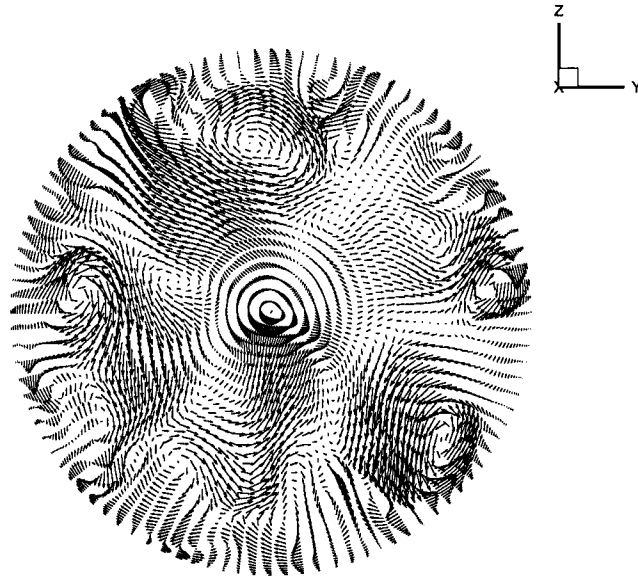


Figure 4.18 Instantaneous velocity vector plot in the cross section of pipe

#### 4.2.5 Friction Coefficient

In this section, the average friction coefficients are compared to DNS results, experimental data and various empirical correlations. The friction coefficient is defined as

$$C_f = f = \frac{\tau_w}{\frac{1}{2}\rho_b u_b^2} \quad (4.36)$$

In addition to Blasius's law  $C_f = 0.079 Re_D^{-0.25}$ , various empirical correlations for the friction coefficient with constant properties have been developed in the literature. Petukhov and Popov (1963) performed theoretical calculations for fully developed turbulent flow with constant properties in circular tubes with constant heat flux boundary conditions and obtained the correlation

$$f = (3.64 \log_{10} Re_D - 3.28)^{-2} \quad (4.37)$$

where  $Re_D$  is the bulk Reynolds number based on hydraulic diameter,  $Re_D = u_b D_h / \nu_b$ . This correlation is valid for  $10^4 < Re_D < 5 \times 10^5$ . Gnielinski (1976) modified the above correlation to cover a lower Reynolds number range ( $2300 < Re_D < 5 \times 10^6$ ) yielding

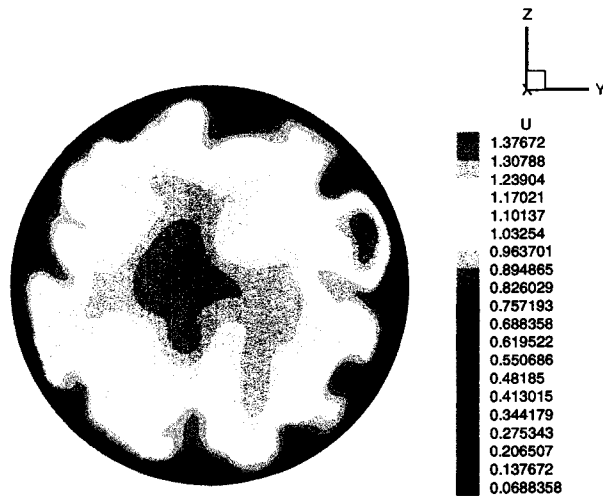


Figure 4.19 Contours of instantaneous streamwise velocity in the  $yz$  plane

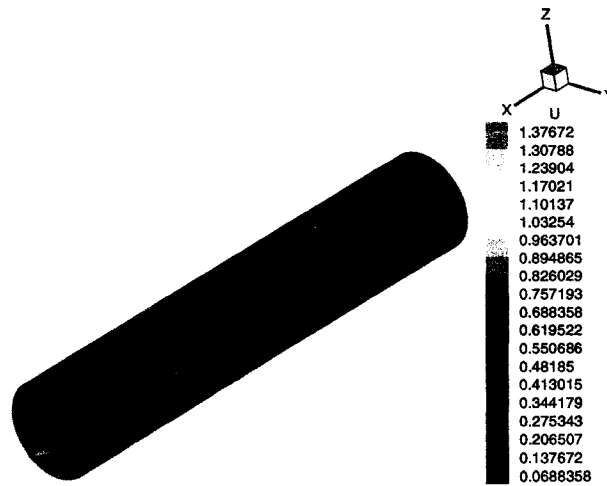


Figure 4.20 Contours of instantaneous streamwise velocity in the near wall region

$$f = (1.58 \ln Re_D - 3.28)^{-2} \quad (4.38)$$

An explicit form that agrees with the Prandtl correlation (Prandtl, 1944),  $1/\sqrt{f} = 1.7272 \ln(Re\sqrt{f}) - 0.3946$ , within  $\pm 0.1\%$  was developed by Techo, Tickner, and James (Kakac, 1987) as

$$\frac{1}{f} = \left( 1.7272 \ln \frac{Re_D}{1.964 \ln Re_D - 3.8215} \right)^2 \quad (4.39)$$

Kays and Crawford (1993) recommend the correlation given by

$$f = 0.046 Re_d^{-0.2} \quad (4.40)$$

The comparisons to DNS, experiments, and the above correlations with three different grid resolutions,  $48 \times 32 \times 64$ ,  $64 \times 40 \times 80$  and  $64 \times 40 \times 100$ , are presented in Table 4.4, Table 4.5 and Table 4.6, respectively. In the tables, the difference between present results and DNS, experimental data or correlations, *diff*, is defined as

$$diff = \frac{Present \text{ results} - Comparison \text{ data}}{Comparison \text{ data}} \quad (4.41)$$

Both coarse grids resulted in underprediction of the friction coefficient. Excellent agreement with DNS and experimental data was obtained with fine grid, and also good agreement when compared with the correlations.

### 4.3 Summary

The simulations of the turbulent flow in a high ratio annulus at a low Reynolds number  $Re_s = 2800$  and in a pipe at  $Re_D = 5300$  were performed to evaluate the finite volume formulation with hexahedral and tetrahedral volumes in the axisymmetric geometry. For the annular flow, very good agreement in the mean velocity and root-mean-square velocity fluctuations was obtained when compared with the DNS and experimental results for the planar channel flow. Slightly asymmetric profiles of the *rms* results were found, probably due to the differing inner and outer areas. The higher order statistics were also found to be in reasonably good agreement with the DNS and experimental results.

Table 4.4 Comparison of friction coefficient with  $48 \times 32 \times 64$  grid

Correlation	Equation	$C_f$	% diff
Present simulation ( $48 \times 32 \times 64$ grid)	–	0.00791	–
DNS	–	0.00922	-14.2
PIV	–	0.00903	-12.4
LDA	–	0.00928	-14.8
Blasius Law	$C_f = 0.079Re_D^{-0.25}$	0.00926	-14.6
Petukhov and Popov (1963)	Eq. 4.37	0.00947	-16.5
Gnielinski (1976)	Eq. 4.38	0.00948	-16.6
Techo, Tickner and James (1987)	Eq. 4.39	0.00928	-14.8
Kays and Crawford (1993)	Eq. 4.40	0.00828	-4.5

Table 4.5 Comparison of friction coefficient with  $64 \times 40 \times 80$  grid

Correlation	Equation	$C_f$	% diff
Present simulation ( $64 \times 40 \times 80$ grid)	–	0.00848	–
DNS	–	0.00922	-8.7
PIV	–	0.00903	-6.1
LDA	–	0.00928	-8.6
Blasius Law	$C_f = 0.079Re_D^{-0.25}$	0.00926	-8.4
Petukhov and Popov (1963)	Eq. 4.37	0.00947	-10.5
Gnielinski (1976)	Eq. 4.38	0.00948	-10.5
Techo, Tickner and James (1987)	Eq. 4.39	0.00928	-8.6
Kays and Crawford (1993)	Eq. 4.40	0.00828	+2.4

Table 4.6 Comparison of friction coefficient with  $64 \times 40 \times 100$  grid

Correlation	Equation	$C_f$	% diff
Present simulation ( $64 \times 40 \times 100$ grid)	–	0.00905	–
DNS	–	0.00922	-1.8
PIV	–	0.00903	+0.2
LDA	–	0.00928	-2.5
Blasius Law	$C_f = 0.079Re_D^{-0.25}$	0.00926	-2.3
Petukhov and Popov (1963)	Eq. 4.37	0.00947	-4.4
Gnielinski (1976)	Eq. 4.38	0.00948	-4.5
Techo, Tickner and James (1987)	Eq. 4.39	0.00928	-2.5
Kays and Crawford (1993)	Eq. 4.40	0.00828	+9.3

For the turbulent pipe flow, a grid study was performed which determined that a grid resolution of  $64 \times 40 \times 100$  in the streamwise, radial and circumferential directions was necessary and sufficient to produce satisfactory results. With this fine grid, very good agreement with DNS and experimental data was obtained in mean velocities, *rms* velocity fluctuations, and shear stress distributions. The overall agreement with DNS and experimental high order statistics was reasonable. For the friction coefficient, excellent agreement was obtained with DNS and experimental data and good agreement was observed when compared with correlations.

The results from the turbulent annulus and pipe flow demonstrated that the present second-order accurate finite volume formulation based on Cartesian coordinates is capable of performing accurate LES for the flow through the axisymmetric geometry using hexahedral and tetrahedral control volumes with moderate grid resolution. The grid resolution,  $64 \times 40 \times 100$ , was used in all the following simulations in the next chapter.

## CHAPTER 5. TURBULENT PIPE FLOW WITH LOW HEAT TRANSFER

It is appropriate that the LES formulation be examined for fully developed turbulent pipe flow with very small property variation before it is used in cases with significant property variations. This chapter will evaluate the LES formulation for turbulent pipe flow with very low constant heat flux. The present formulation accounts for variable properties, but with very low heat flux, these variations will be very small. The results of temperature mean profile and statistics will be compared with DNS results which were obtained with the constant properties idealization. Comparisons will also be made to empirical correlations for the friction coefficient and Nusselt number.

### 5.1 Problem Description

The problem of interest is a fully developed turbulent pipe flow with constant wall heat flux, as depicted in Fig 5.1. In order to compare with the passive scalar DNS results, the wall heat flux was set low enough to ensure the temperature and density variations were small.

For the fully developed turbulent pipe flow with constant fluid properties, the time averaged streamwise velocity and temperature no longer change in the streamwise direction. Consequently, the average local, wall, and bulk streamwise temperature gradients are all equal to a constant and only depend on the amount of heat being added to the flow, as

$$\frac{\partial T}{\partial x} = \frac{\partial T_w}{\partial x} = \frac{\partial T_b}{\partial x} = \text{constant} \quad (5.1)$$

where the bulk temperature is defined as

$$T_b = \frac{1}{\rho_b u_b A_c} \int \rho u T dA \quad (5.2)$$

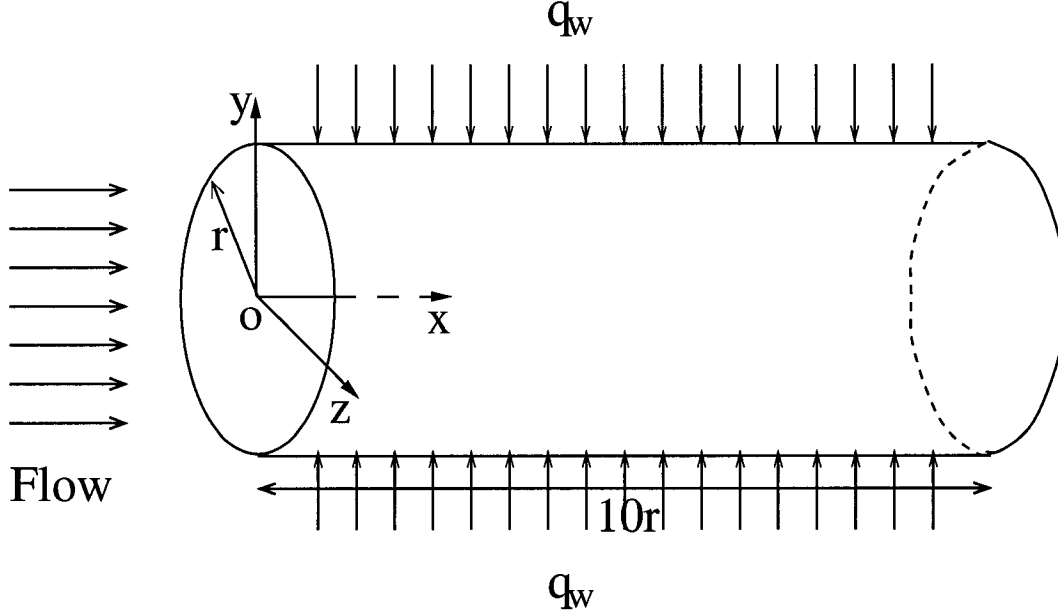


Figure 5.1 Schematic of pipe flow with constant wall heat flux,  $q_w$

## 5.2 Boundary Conditions

Nonslip wall conditions and zero normal pressure gradient boundary conditions were enforced at the wall. Since fully developed pipe flow is considered in this study, the periodic boundary conditions were used in the streamwise directions. The primitive variables,  $\tilde{u}_i$  could be assumed to be periodic, but the pressure and temperature were not periodic in the streamwise direction. As discussed in Chapter 4, the periodic pressure assumptions was enforced by decomposing the pressure into periodic and aperiodic components. The temperature was also decomposed into periodic and aperiodic components, as

$$\tilde{T}(x, y, z, t) = \phi x + \tilde{T}_p(x, y, z, t) \quad (5.3)$$

where  $\phi$  are the average streamwise temperature gradient. The periodic component of temperature satisfies

$$\tilde{T}_p(0, y, z, t) = \tilde{T}_p(L_x, y, z, t) \quad (5.4)$$

where  $L_x$  is the length of the pipe in the streamwise direction. Consequently, the temperature was treated in a step periodic manner as

$$\begin{aligned}\tilde{T}(0, y, z, t) &= \tilde{T}(L_x, y, z, t) - \Delta\tilde{T}_x \\ \tilde{T}(L_x, y, z, t) &= \tilde{T}(0, y, z, t) + \Delta\tilde{T}_x\end{aligned}\quad (5.5)$$

Assuming that the axial conduction and viscous dissipation were negligible, the bulk streamwise temperature difference,  $\Delta\tilde{T}_b$ , was obtained by integrating the energy equation around the boundaries of the solution domain giving

$$\Delta\tilde{T}_b = \frac{4q_w L_x}{(\frac{\dot{m}}{A_c})D} \quad (5.6)$$

where  $\dot{m}/A_c$  is the nondimensional mass flow rate per unit cross-sectional area, and  $D$  is the nondimensional pipe diameter. The constant nondimensional heat flux desired at the wall,  $q_w$ , is defined as

$$q_w = \frac{q_w^*}{\rho_{ref} U_{ref} T_{ref} C_p^*} \quad (5.7)$$

According to the condition given by Eq. 5.1, the local streamwise temperature difference,  $\Delta\tilde{T}_x$ , equals the bulk streamwise temperature difference, yielding

$$\Delta\tilde{T}_x = \frac{4q_w L_x}{(\frac{\dot{m}}{A_c})D} \quad (5.8)$$

Given  $q_w$ , the isoflux thermal boundary condition at the wall could be implemented by setting

$$\left(-k^* \frac{\partial T^*}{\partial y^*}\right) = q_w^* \quad (5.9)$$

However, Kasagi et al. (1989) and Dailey (1997) reported that implementing the above condition for DNS and LES gives near wall fluctuations larger than observed experimentally because the simulations do not take into account the heat capacity of the wall. The wall temperature fluctuations should be negligibly small so that the wall could be regarded as isothermal.

In order to obtain small wall temperature fluctuations and achieve the desired heat flux, a fixed wall temperature which varied linearly in the streamwise direction could be enforced as follows,

$$T_w(x) = T_w(0) + \left(\frac{\partial T_w}{\partial x}\right)x \quad (5.10)$$

where  $T_w(0)$  is the wall temperature at the first location of the simulation domain, and  $\partial T_w/\partial x$  is the wall temperature gradient along the stream wise direction.

In the current simulations, both ways of imposing the isoflux boundary condition were studied. Unreasonable large temperature fluctuations near the wall were observed when using Eq. 5.9, while more realistic near wall temperature fluctuations were obtained with Eq. 5.10.

### 5.3 Simulation Details

The flow field of isothermal fully developed pipe flow was used as the initial flow field for this simulation. The nondimensional wall heating rate was set as  $q_w = 4.0 \times 10^{-4}$ . The nondimensional pipe dimensions were  $10 \times 1 \times 2\pi$  in the streamwise, radial and circumferential directions, respectively. The reference Mach number was set as  $M_r = 0.001$  to ensure nearly incompressible results. The nondimensional time step was 0.01.

According to the grid independence study in Chapter 4, the same fine grid,  $64 \times 40 \times 100$  in the streamwise, radial, and circumferential directions, was used in this study. As discussed in Chapter 4, the grid was uniformly spaced in the streamwise and circumferential directions, but clustered towards the wall using algebraic hyperbolic tangent stretching in the radial direction.

The simulations were run with the dual time stepping, preconditioned LU-SGS scheme using 9 processors on the Origin machines, and the tolerance value (see Eq. 3.55) was  $TOL = 1.0 \times 10^{-7}$ . The turbulence statistics were collected using about  $N_{stat} = 10,000$  time steps when the flow was statistically stationary.

### 5.4 Results for Temperature Statistics

The temperature statistics were compared to the passive scalar DNS results of Satake and Kunugi (1999). The nondimensional DNS computational domain was  $15 \times 1 \times 2\pi$  with a grid of  $256 \times 128 \times 128$  points in the streamwise, radial, and circumferential directions, respectively. The bulk Reynolds number was  $Re_D = 5286$ . A finite difference method was adopted in the DNS with a 2nd-order central scheme for the non-linear and viscous terms. The dimensionless temperature parameter,  $\theta^+$  is defined as

$$\theta^+(x, y, z, t) = \frac{\langle T_w^* \rangle(x) - T^*(x, y, z, t)}{T_\tau^*} \quad (5.11)$$

where  $\langle T_w^* \rangle$  is the averaged wall temperature and  $T_\tau^*$  is the friction temperature. The friction temperature was calculated by

$$T_\tau^* = \frac{q_w^*}{\rho_w^* c_p^* u_\tau^*} \quad (5.12)$$

For the present simulations, very low heat flux resulted in a wall-to-bulk temperature ratio of  $T_w/T_b = 1.08$ . Since the variation of the temperature parameter,  $\theta^+$  in the streamwise direction was negligibly small due to very low heat transfer, the ensemble averages of the temperature statistics were performed in the streamwise and circumferential directions and in time. The mean temperature profiles are plotted in wall coordinates in Fig. 5.2. Linear profile,  $\theta^+ = Pr y^+$  was solved exactly in the conductive sublayer with both isoflux and fixed linear wall temperature gradient thermal boundary conditions. The results also agree well with DNS data and the empirical log-law ( $\theta^+ = 2.853 \ln y^+ + 2.347$ ) formula in the logarithmic region except for a little underprediction near the center.

The *rms* of the temperature fluctuations in the near wall region is shown in Fig. 5.3. The isoflux thermal boundary condition resulted in large overprediction when compared with the DNS results, and unrealistically large temperature fluctuations at the wall. However, the *rms* temperature fluctuations obtained with the fixed wall temperature distribution boundary condition matched with the DNS data very well in the near wall region.

The streamwise and wall-normal turbulent heat fluxes normalized by friction velocity and temperature are shown in Fig. 5.4 and Fig. 5.5. A large overprediction of streamwise turbulent heat flux was observed for the isoflux thermal boundary condition, while very good agreement was obtained with the fixed wall temperature distribution boundary condition. It should be noted that although the temperature fluctuations didn't agree very well with DNS results, fairly good agreement was obtained for the turbulent heat fluxes between the present simulations and DNS data. This may be because the velocity fluctuations dominate the temperature fluctuations here.

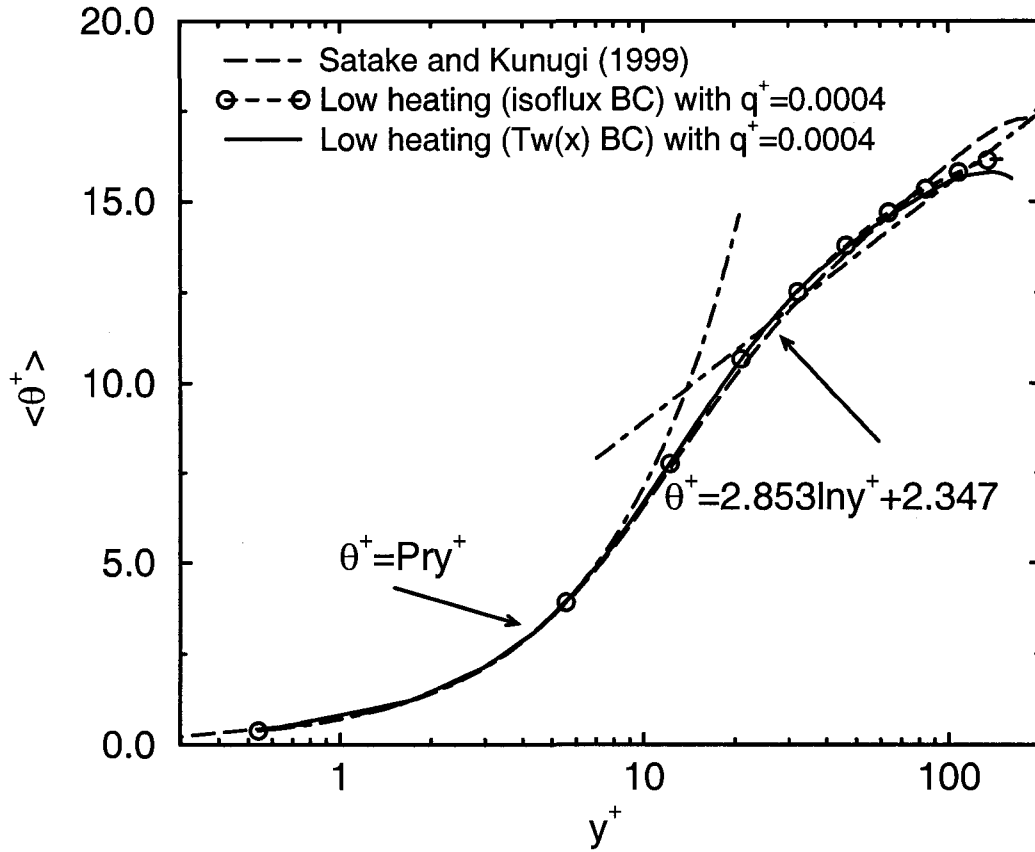


Figure 5.2 Mean temperature distribution in wall coordinates for very low heat flux case

The  $u\theta$  and  $u_r\theta$  cross-correlation coefficients were calculated by

$$R(u\theta) = \frac{\langle u'\theta' \rangle}{u'_{rms}\theta'_{rms}} \quad (5.13)$$

$$R(u_r\theta) = \frac{\langle u'_r\theta' \rangle}{u'_{r,rms}\theta'_{rms}} \quad (5.14)$$

As shown in Fig. 5.6 and Fig.5.7, again, the fixed wall temperature distribution boundary condition resulted in better agreement than the isoflux thermal boundary condition. Good agreement with DNS results was observed in the near wall region; however, a large underprediction was observed in the core region. This is most likely because of the large over prediction of the temperature fluctuations in the core region at a low heating level. This is possibly a nu-

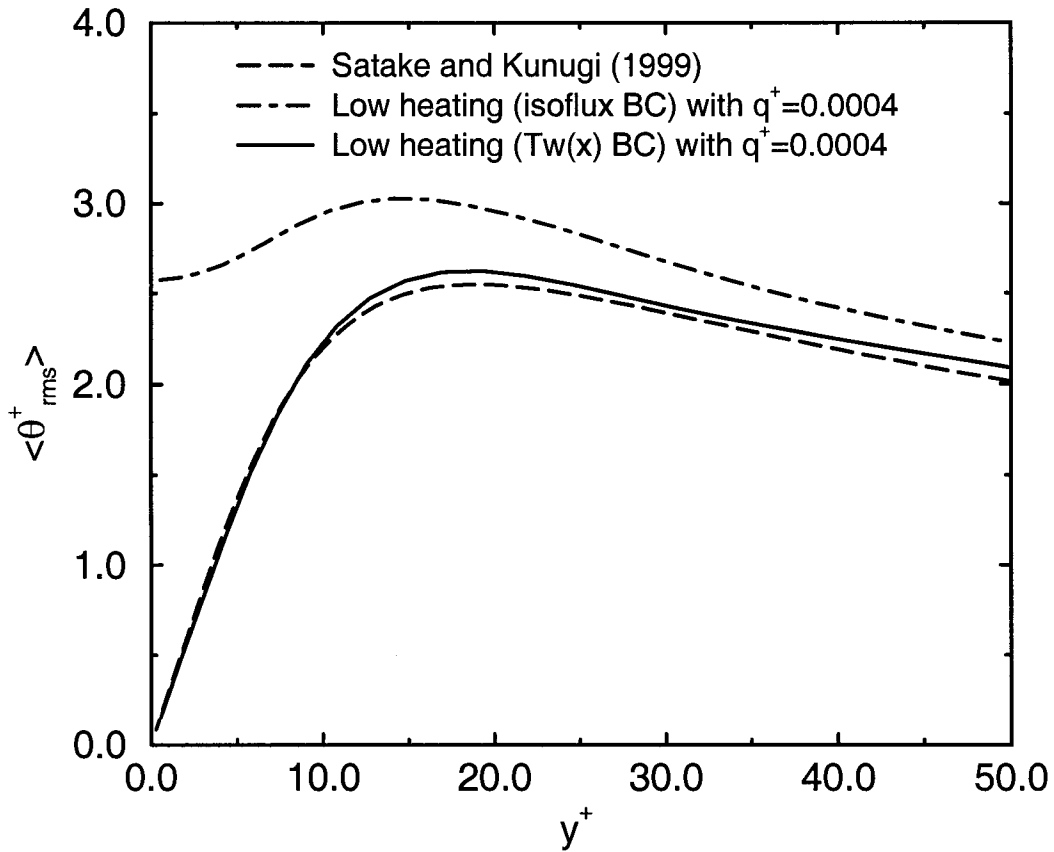


Figure 5.3 RMS of the temperature fluctuations normalized by friction temperature

merically shortcoming because a very small temperature difference is being distributed among 40 control volumes.

#### 5.4.1 Friction Coefficients and Nusselt Numbers

In this section, the friction coefficients and Nusselt numbers are compared with empirical correlations. The friction coefficient,  $C_f$ , is defined by Eq. 4.36. The Nusselt number based on bulk properties and the pipe hydraulic diameter,  $D_h = D$ , is defined as

$$Nu_D = \frac{hD_h}{k_b} \quad (5.15)$$

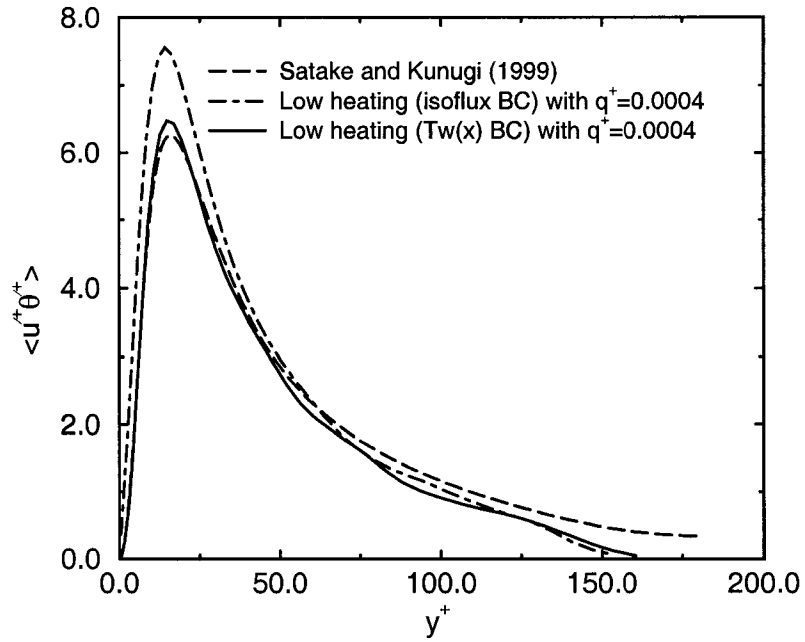


Figure 5.4 Streamwise turbulent heat flux normalized by friction velocity and temperature

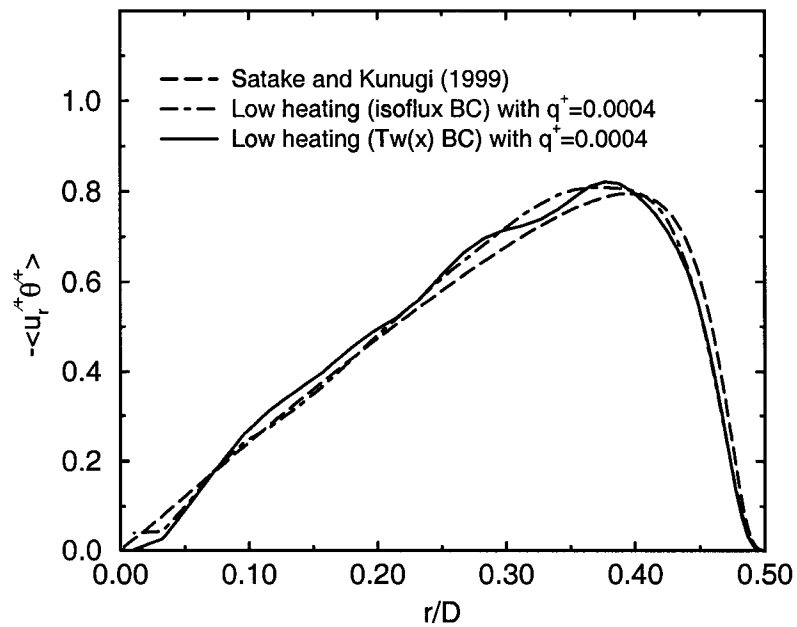


Figure 5.5 Wall-normal turbulent heat flux normalized by friction velocity and temperature

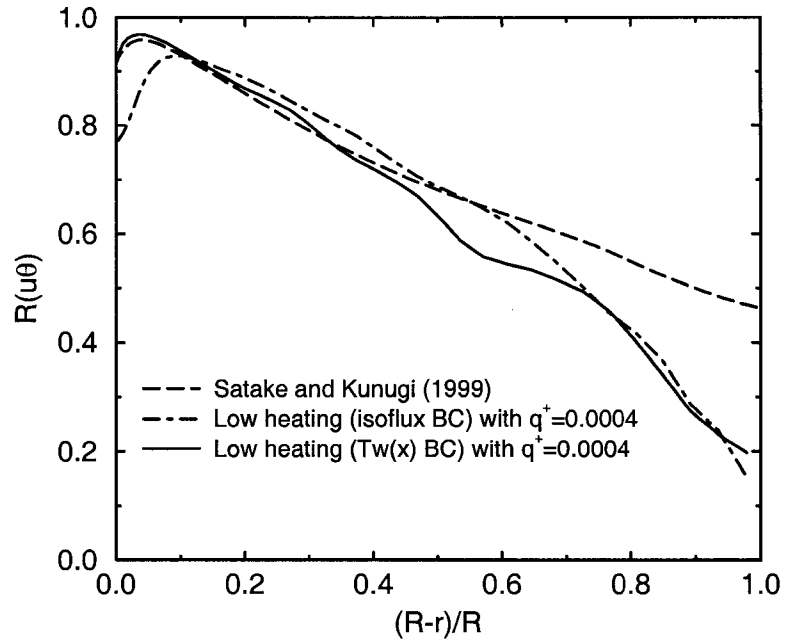


Figure 5.6 Cross-correlation coefficient between normal-to-wall velocity and temperature

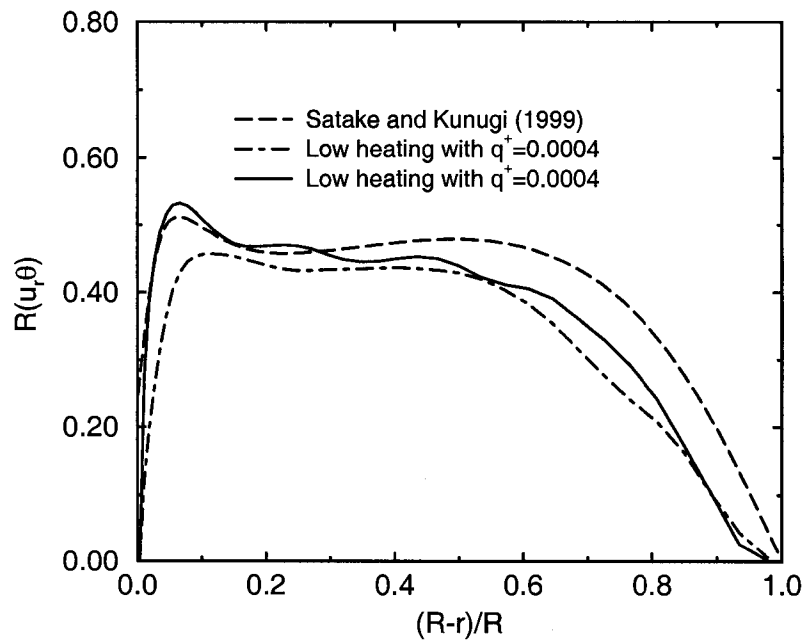


Figure 5.7 Cross-correlation coefficient between streamwise velocity and temperature

Table 5.1 Nusselt numbers and friction factors for the present simulations

Case	$Re_D$	$Nu_D$	$C_f$
Isoflux thermal boundary condition	5197.82	16.3	0.01
Fixed wall temperature distribution	5488.9	17	0.0085

The constant property empirical correlations for friction coefficients were listed in the section 4.2.5 of Chapter 4. Also, various empirical correlations for Nusselt numbers with constant properties were developed in the literature. McAdams (1954) provided a simple correlation as

$$Nu_D = 0.021 Re_D^{0.8} Pr^{0.4} \quad (5.16)$$

based on data for common gases and  $Pr \approx 0.7$ . Petukhov and Popov (1963) performed theoretical calculations for fully developed turbulent flow with constant properties in circular tubes with constant heat flux boundary conditions and obtained the correlation

$$Nu_D = \frac{(f/2) Re_D Pr}{(1 + 13.6f) + (11.7 + 1.8 Pr^{-1/3})(f/2)^{1/2}(Pr^{2/3} - 1)} \quad (5.17)$$

where  $f$  is the friction coefficient calculated by Eq. 4.37. However, this correlation is valid for high Reynolds number  $10^4 < Re_D < 5 \times 10^5$  and  $0.5 < Pr < 2000$  with 1% error. To cover the lower Reynolds numbers, Gnielinski (1976) modified the above correlation as

$$Nu_D = \frac{(f/2)(Re_D - 1000)Pr}{1 + 12.7(f/2)^{1/2}(Pr^{2/3} - 1)} \quad (5.18)$$

where  $Re_D$  is the Reynolds number based on bulk properties and hydraulic diameter. The friction coefficient was calculated by Eq. 4.38. This correlation is valid for  $2300 < Re_D < 5 \times 10^6$ . Kays and Crawford (1993) recommend a correlation given by

$$Nu_D = 0.022 Re_D^{0.8} Pr^{0.5} \quad (5.19)$$

The friction coefficients and Nusselt numbers for the present simulations with two different thermal boundary conditions are listed in Table 5.1. The comparisons to various empirical constant property correlations are shown in Tables 5.2, 5.3, 5.4 and 5.5. The difference between present results and DNS data or correlations, *diff*, in the tables is defined in the section 4.2.5

Table 5.2 Comparison to constant property correlations for friction coefficient with isoflux thermal boundary condition

Correlation	Equation	$C_f$	% diff
Present simulation	–	0.01	–
Blasius Law	$C_f = 0.079Re_D^{-0.25}$	0.0093	+7.5
Petukhov and Popov (1963)	Eq. 4.37	0.0095	+4.75
Gnielinski (1976)	Eq. 4.38	0.0095	+4.75
Techo, Tickner and James (1987)	Eq. 4.39	0.0093	+7.5
Kays and Crawford (1993)	Eq. 4.40	0.0083	+20.4

Table 5.3 Comparison to constant property correlations for friction coefficient with fixed wall temperature condition

Correlation	Equation	$C_f$	% diff
Present simulation	–	0.0085	–
Blasius Law	$C_f = 0.079Re_D^{-0.25}$	0.0091	-6.6
Petukhov and Popov (1963)	Eq. 4.37	0.0093	-8.6
Gnielinski (1976)	Eq. 4.38	0.0093	-8.6
Techo, Tickner and James (1987)	Eq. 4.39	0.0092	-7.6
Kays and Crawford (1993)	Eq. 4.40	0.0082	+3.7

Table 5.4 Comparison to constant property correlations for Nusselt number with isoflux thermal boundary condition

Correlation	Equation	$Nu_D$	% diff
Present simulation	–	16.3	–
McAdams (1954)	Eq. 5.16	17.1	-4.7
Petukhov and Popov (1963)	Eq. 5.17	18.72	-12.9
Gnielinski (1976)	Eq. 5.18	17.23	-5.4
Kays and Crawford (1993)	Eq. 5.19	17.4	-6.32

Table 5.5 Comparison to constant property correlations for friction coefficient with fixed wall temperature condition

Correlation	Equation	$Nu_D$	% diff
Present simulation	–	17	–
McAdams (1954)	Eq. 5.16	17.96	-5.6
Petukhov and Popov (1963)	Eq. 5.17	19.37	-12.23
Gnielinski (1976)	Eq. 5.18	18.0	-5.5
Kays and Crawford (1993)	Eq. 5.19	18.18	-6.5

of Chapter 4. For the specified wall heat flux boundary condition, the friction coefficient was overpredicted and Nusselt number was underpredicted. Both friction coefficient and the Nusselt number for the fixed wall temperature boundary condition were underpredicted compared with correlations. Compared to the isothermal case, a larger difference between the present simulations and correlations were observed. This is most likely because the properties were not exactly constant in the present simulations. Overall, agreement with correlations was good for both friction coefficients and Nusselt numbers.

## 5.5 Summary

The simulations of turbulent pipe flow with low constant wall heating were performed using two different wall boundary conditions: fixed wall heat flux,  $q_w$ , and fixed wall temperature,  $Tw(x)$ . The  $64 \times 40 \times 100$  fine grid and a dynamic SGS model was used in the simulations. The temperature statistics were compared with DNS passive scalar results. The mean temperature matches with DNS data very well with both boundary conditions. In the near wall region, the temperature fluctuations compares well with DNS results for the fixed wall temperature boundary condition, while it was over predicted with isoflux wall boundary conditions. Also, good agreement was obtained with fixed wall temperature boundary conditions in the near wall region for the turbulent heat fluxes and  $u\theta$  and  $u_r\theta$  cross-correlation coefficients. However, because it is difficult to propagate the temperature differences from the boundaries to pipe

center when  $\Delta T_x$  is very small, the present results didn't match with the DNS data very well in the core region of pipe. This problem didn't occur in the later simulations in Chapter 6 with larger temperature differences. The friction coefficients and Nusselt numbers also compared well with various empirical correlations. Consequently, the finite volume formulation with fixed wall temperature condition could be used to predict the fully developed turbulent pipe flows with property variations.

## CHAPTER 6. LES OF MIXED CONVECTION IN A VERTICAL TURBULENT PIPE FLOW

This chapter deals with LES of turbulent mixed convection in a vertical pipe with significant property variations resulting from constant heat flux. Six cases with three different constant wall heat fluxes were considered. The compressible filtered Navier-Stokes equations including body force terms were solved using a second order accurate finite volume method. Low Mach number preconditioning was used to enable the compressible code to work efficiently at low Mach numbers. A dynamic subgrid-scale stress model accounted for the subgrid-scale turbulence. The simulated mean profiles were compared with experimental results; friction factors and Nusselt numbers were compared with both experimental and empirical correlations. The effects of high heating and buoyancy were also investigated.

### 6.1 Introduction

Due to the advantages of safety, chemical inertness, and high thermal efficiency, gas coolants have been considered for nuclear reactors and heat exchangers for both fission and fusion. These applications commonly operate with turbulent flow with significant heat transfer resulting in large property variations. However, most experiments have been conducted in tubes too small to permit measurements of detailed velocity and temperature profiles. In most cases, only integral measurements like heat transfer coefficient and/or friction factor were determined (McEligot, 1986). Many proposed analytical and computational models provide poor predictions for convective heat transfer even when the properties can be idealized as a constant (Mikielewicz, 1994), and it is very clear that the level of difficulty will be increased significantly if property variations and buoyancy forces are considered.

When a gas flowing in a pipe is strongly heated, the turbulent flow may revert to a laminar like state where wall parameters approach the appropriate laminar values at local Reynolds numbers where turbulent flow is normally expected (McEligot, 1986). This is referred to as laminarization (Torii and Yang (1997), Bankston (1970), and Ezato et al. (1999)). Numerous investigators have reported the criteria for the occurrence of laminarization and the heat transfer characteristics of the phenomenon (Coon and Perkins (1970), McEligot et al. (1970), and Ogawa et al. (1982)). This laminarization phenomenon is thought to be promoted by two effects.

(1) the local Reynolds number,  $Re_x$ , is reduced significantly with increasing temperature, particularly near the heated wall since the viscous sublayer would be thicker than in an unheated flow. (Bates et al. (1974)). (Properties like local density and viscosity would decrease and increase with temperature, respectively).

(2) the flow associated with buoyancy may be accelerated due to the local density reduction (McEligot et al. (1998)).

A system for which the buoyancy force acts in the same direction as the flow is called an aiding flow. Nakajima and Fukui (1979) studied a mixed convection flow experimentally and showed that the buoyancy force reduced the velocity fluctuations in the aiding flow case. Polyakov (1973) reported that the buoyancy forces modified the friction factor, the Nusselt number, and the velocity and temperature wall laws for turbulent heated flow in a vertical circular pipe.

Direct numerical simulation (DNS) and large eddy simulation (LES) have provided means for obtaining detailed information about turbulent flows (Kim and Moin (1989), Nicoud and Poinot (1999), Iida and Kasagi (1997), Wang and Pletcher (1996), and Dailey and Pletcher (1998)). The goal of the present study is to investigate turbulent pipe flow with particular attention being paid to the effects of heat transfer and buoyancy on the mean and instantaneous structures. It is very expensive to perform LES for a developing pipe flow with strong heating. The region of interest in this research is the “quasi-developed” region (McEligot et al., 1965), where thermal entry effects are no longer important.

## 6.2 Governing Equation

To consider the buoyancy effects in the vertical turbulent pipe flow, the body forces were included into the Navier-Stokes equations.

### 6.2.1 Compressible Nondimensional Navier-Stokes (N-S) Equations

The non-dimensional compressible N-S equations, Eq. 2.10 - Eq. 2.12, are changed to

- Conservation of mass

$$\frac{\partial \rho}{\partial t} + \frac{\partial(\rho u_i)}{\partial x_i} = 0 \quad (6.1)$$

- Conservation of momentum

$$\frac{\partial(\rho u_i)}{\partial t} + \frac{\partial(\rho u_i u_j)}{\partial x_j} = -\frac{\partial p}{\partial x_i} + \frac{\partial \sigma_{ij}}{\partial x_j} - \frac{Ra}{(2\epsilon Pr Re_{ref}^2)} \rho \delta_{1i} \quad (6.2)$$

- Conservation of energy

$$\frac{\partial(\rho E)}{\partial t} + \frac{\partial(\rho E u_j)}{\partial x_j} = -\frac{\partial(p u_j)}{\partial x_j} - \frac{\partial q_j}{\partial x_j} + \frac{\partial(\sigma_{ij} u_i)}{\partial x_j} - \frac{Ra}{(2\epsilon Pr Re_{ref}^2)} \rho u_i \delta_{1i} \quad (6.3)$$

where  $\delta_{1i}$  is the Kronecker function.  $\epsilon$  is the temperature difference defined by

$$\epsilon = (T_w - T_b)/T_b \quad (6.4)$$

where  $T_w$  and  $T_b$  represent the wall and bulk temperatures, respectively.

And the Rayleigh number,  $Ra$ , is,

$$Ra = \frac{2g\epsilon\rho_{ref}^2 L_{ref}^3 Pr}{\mu_{ref}^2} \quad (6.5)$$

### 6.2.2 Favre Filtered Equations

The compressible N-S equations, Eq 6.1 - 6.3, are filtered to separate the large-scale motions from small-scale motions and become

$$\frac{\partial \bar{\rho}}{\partial t} + \frac{\partial(\bar{\rho}\tilde{u}_j)}{\partial x_j} = 0 \quad (6.6)$$

$$\frac{\partial(\bar{\rho}\tilde{u}_i)}{\partial t} + \frac{\partial(\bar{\rho}\tilde{u}_i\tilde{u}_j)}{\partial x_j} = -\frac{\partial \bar{p}}{\partial x_i} + \frac{\partial \bar{\sigma}_{ij}}{\partial x_j} - \frac{Ra}{(2\epsilon Pr Re_{ref}^2)} \bar{\rho} \delta_{1i} - \frac{\partial \tau_{ij}}{\partial x_j} \quad (6.7)$$

$$\frac{\partial(\bar{\rho}\hat{E})}{\partial t} + \frac{\partial[(\bar{\rho}\hat{E} + \bar{p})\tilde{u}_j]}{\partial x_j} = \frac{\partial(\tilde{u}_i\bar{\sigma}_{ij})}{\partial x_j} - \frac{\partial \bar{q}_j}{\partial x_j} - \frac{Ra}{(2\epsilon Pr Re_{ref}^2)} \bar{\rho}\tilde{u}_i\delta_{1i} - \frac{\partial q_{tj}}{\partial x_j} - \alpha - \pi - \varepsilon \quad (6.8)$$

where

$$\alpha = \tilde{u}_i \frac{\partial \tau_{ij}}{\partial x_j} \quad (6.9)$$

$$\pi = \overline{p \frac{\partial u_j}{\partial x_j}} - \bar{p} \frac{\partial \tilde{u}_j}{\partial x_j} \quad (6.10)$$

$$\varepsilon = \overline{\sigma_{ij} \frac{\partial u_i}{\partial x_j}} - \bar{\sigma}_{ij} \frac{\partial \tilde{u}_j}{\partial x_j} \quad (6.11)$$

For the present work,  $\alpha$ ,  $\pi$  and  $\varepsilon$  were neglected since only low Mach number flows were considered, which is an appropriate assumption for Mach numbers below 0.2 (Vreman et al. 1995). The filtered viscous stress tensor and heat flux vector are approximated as

$$\bar{\sigma}_{ij} \approx \frac{\bar{\mu}}{Re_{ref}} \left[ \left( \frac{\partial \tilde{u}_i}{\partial x_j} + \frac{\partial \tilde{u}_j}{\partial x_i} \right) - \frac{2}{3} \frac{\partial \tilde{u}_k}{\partial x_k} \delta_{ij} \right] \quad (6.12)$$

$$\bar{q}_j \approx -\frac{C_p \bar{\mu}}{Re_{ref} Pr} \frac{\partial \tilde{T}}{\partial x_j} \quad (6.13)$$

the turbulent stress tensor and heat flux vector are

$$\tau_{ij} = \bar{\rho}(\overline{\tilde{u}_i \tilde{u}_j} - \tilde{u}_i \tilde{u}_j) \quad (6.14)$$

$$q_{tj} = \bar{\rho} C_v (\overline{\tilde{u}_j \tilde{T}} - \tilde{u}_j \tilde{T}) \quad (6.15)$$

and modeled using the dynamic SGS model.

Consequently, the nondimensional integral-vector form of Favre filtered equations are written as follows:

$$\int_{\Omega} [T] \frac{\partial \mathbf{W}}{\partial t} d\Omega + \int_{\partial\Omega} (\mathbf{E}\vec{i} + \mathbf{F}\vec{j} + \mathbf{G}\vec{k}) \cdot d\vec{S} = \int_{\Omega} \mathbf{B} d\Omega \quad (6.16)$$

where

$$\mathbf{B} = \begin{bmatrix} 0 \\ -\frac{Ra}{(2\epsilon Pr Re_{ref}^2)} \frac{\bar{p}}{T} \\ 0 \\ 0 \\ -\frac{Ra}{(2\epsilon Pr Re_{ref}^2)} \frac{\bar{p}\tilde{u}}{T} \end{bmatrix} \quad (6.17)$$

### 6.3 Boundary Conditions

The governing equations require specification of boundary conditions at the wall, inlet and outlet due to the elliptic nature of the equations. Nonslip wall conditions are imposed at the wall. Referring to the studies of isoflux thermal boundary conditions in Chapter 5, the fixed wall temperature distribution, Eq. 5.10, which resulted in reasonable near wall temperature fluctuations was used in all following simulations. Since quasi-developed pipe flow is considered in this study, step periodic boundary conditions are used at the inlet and outlet as follows,

$$\begin{aligned} p_p(0, y) &= p_p(L_x, y) \\ \rho u(0, y) &= \rho u(L_x, y) \\ v(0, y) &= v(L_x, y) \\ w(0, y) &= w(L_x, y) \\ T(0, y) &= T(L_x, y) - \Delta T_x \end{aligned} \quad (6.18)$$

where  $p_p$  is the periodic component of the pressure, and  $L_x$  is the length of the pipe in the streamwise direction. With small property variations, the temperature difference,  $\Delta T_x$ , can be approximated by the streamwise change in the bulk temperature as

$$\Delta T_x \approx \Delta T_b = \frac{4q_w L_x}{(\frac{\dot{m}}{A_c})D} \quad (6.19)$$

where  $D$  is the pipe diameter,  $q_w$  is the wall heat flux, and  $\dot{m}/A_c$  is the average mass flow rate per unit area. However,  $\Delta T_x$  is a function of  $r$  when the property variations are significant. Referring to the experimental data, the profile of  $\Delta T_x$  in the cross section of a pipe could be a function with different exponents at different locations. In this work, it was assumed as

$$\Delta T_x(r) = c_1 r^n + c_2 \quad (6.20)$$

It is very difficult to decide the value of the exponent,  $n$ , to obtain a desired state. Several trials were required to obtain the proper exponent and wall temperature distribution to match with the experimental data. By specifying the wall streamwise temperature difference,  $\Delta T_w$ , and bulk temperature rise,  $\Delta T_b$ , for the pipe, the constants  $c_1$  and  $c_2$  were calculated as discussed in Appendix B, yielding

$$c_1 = \frac{\Delta T_b - \Delta T_w}{I_{\rho ur} - 1} \quad (6.21)$$

$$c_2 = \frac{I_{\rho ur} \Delta T_w - \Delta T_b}{I_{\rho ur} - 1} \quad (6.22)$$

where

$$I_{\rho ur} = \frac{1}{\rho_b u_b A_c} \int \rho u r^n dA \Big|_{x=L_x} \quad (6.23)$$

## 6.4 Simulation Details

Simulations were conducted for air flowing upwards in a vertical pipe as shown in Fig. 6.1. The experiments for air flowing upward in a vertical pipe flow were conducted by Shehata and McEligot (1998) at high heating rates causing significant property variations in mixed convection in which the forced convection was dominant. Three characteristic cases, “turbulent”, “sub-turbulent” and “laminarizing”, were studied by Shehata and McEligot (1998) at different nondimensional heating rates of  $q_{in} \approx 0.0018, 0.0035$  and  $0.0045$ .

In this research, the simulations with different constant heat fluxes were performed to match with the experimental data of Shehata and McEligot (1998). The constant heat flux conditions

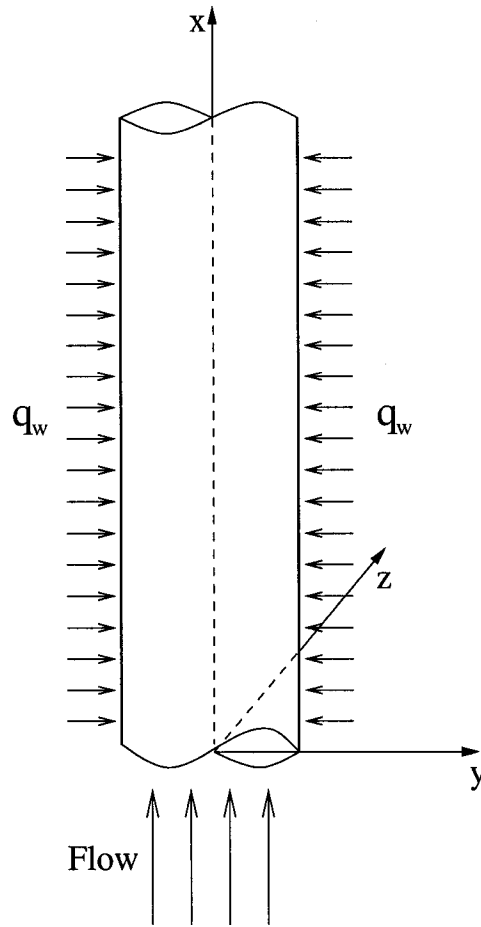


Figure 6.1 The configuration of vertical pipe flow

were achieved by specifying a proper fixed wall temperature distribution and  $\Delta T_x$  profile referring to experimental values. The wall temperature varied linearly along the streamwise direction. Since the step-periodic boundary condition was used in this research, it was very difficult to set up proper thermal boundary conditions without referring to experimental data, especially for the flows with very high heat transfer. The simulation conditions are tabulated in Table 6.1. In this table,  $x/D$  is the location of the experimental data used to set up the corresponding simulation,  $q_{in}$  is the nondimensional heat flux with the reference temperature based on the inlet temperature of experiments. The values of  $T_w(0)$ ,  $dT_w/dx$  and  $dT_b/dx$  are all nondimensionalized with respect to the experimental inlet temperature.

All cases were simulated with a same computational domain and grid resolution as used

Table 6.1 Conditions for cases

Cases	$x/D$	$n$	$q_{in}$	$T_w(0)$	$dT_w/dx$	$dT_b/dx$
1	14.195	2	$1.8 \times 10^{-3}$	1.47	$3.973 \times 10^{-3}$	$3.6 \times 10^{-3}$
2	19.87	2	$3.5 \times 10^{-3}$	2.18	$1.05 \times 10^{-2}$	$7.0 \times 10^{-3}$
3	14.195	2	$4.5 \times 10^{-3}$	2.17	$1.385 \times 10^{-2}$	$9.0 \times 10^{-3}$
4	24.54	3	$1.8 \times 10^{-3}$	1.67	$4.17 \times 10^{-3}$	$3.6 \times 10^{-3}$
5	24.54	3	$3.5 \times 10^{-3}$	2.49	$1.199 \times 10^{-2}$	$7.0 \times 10^{-3}$
6	24.54	4	$4.5 \times 10^{-3}$	2.587	$1.639 \times 10^{-2}$	$9.0 \times 10^{-3}$

for the low heating case. The grid spacing was uniform in the streamwise and circumferential directions, but was stretched towards the wall using the hyperbolic tangent algorithm as mentioned in Chapter 4. Turbulence statistics were collected using about  $N_{stat} = 10,000$  time steps once the flow was deemed to be statistically stationary. The simulations were all run with 9 processors on the Origin 3800 machine and required about 14-15 hours of wall clock time per 5000 time steps. The tolerance level (see section 3.4) was set as  $TOL = 1.0 \times 10^{-7}$ .

### 6.5 Investigation of $\Delta T_x$

It is very important to chose a proper function for  $\Delta T_x$  to match with the experimental data for high heat flux cases. In this section, a numerical experiment is discribed that was conducted using different distributions of  $\Delta T_x$  to investigate the effect of the  $\Delta T_x$  distribution on the velocity and temperature profiles. All the other conditions were the same as in case 4.

Figure Fig. 6.2 shows the velocity profiles in wall coordinates. The linear velocity distribution was well resolved with all four different functions. However, the velocity values in the logarithmic region were underpredicted. The condition,  $\Delta T_x = c_1 r^3 + c_2$ , resulted in the best agreement with experimental data. The effects on the mean temperature profiles are shown in Fig. 6.3. The condition,  $\Delta T_x = c_1 r^3 + c_2$ , also resulted in the best temperature profile. Therefore, to obtain the best agreement in temperature profiles, it is important to set up a proper  $\Delta T_x$  distribution when using the step-periodic boundary condition to simulate flows

with significant property variations. However, it should be noted that the differences in Nusselt number were less than 2% due to different functions of  $\Delta T_x$ .

## 6.6 Results

In this section, the LES results of case 1-6 are compared with experimental data of case 618 at the location  $x/D = 14.195$ , case 635 at the location  $x/D = 19.87$ , case 445 at the location  $x/D = 14.195$ , case 618 at the location  $x/D = 24.54$ , case 635 at the location  $x/D = 24.54$  and case 445 at the location  $x/D = 24.54$ , respectively. The averaged flow parameters are given in subsection 6.6.1. Then the results are validated by comparing the mean profiles with experimental results in 6.6.2. The fluctuation profiles are presented in the subsection 6.6.3. Finally, shear stress and heat transfer flux profiles are provided in the last subsection.

### 6.6.1 Averaged Flow Parameters

Since the high heat flux, flows are nonhomogeneous in the streamwise direction, all the averages in the following sections were made only in the circumferential direction and in time at a single streamwise location. The bulk parameters of the current simulations and the corresponding experimental data (Shehata and McEligot, 1998) are shown in Tables 6.2 and 6.3, respectively. Although the buoyancy parameter for case 3 is a little smaller than that for experimental case 445, the comparison should still be of interest since forced convection effects are still dominant. Generally, the simulation parameters matched the experimental conditions well.

The Grashof number in the tables is defined as specified in the experiments, giving

$$Gr = \frac{g(D_h^*)^4 q_w^*}{(\nu_b^*)^2 k_b^* T_b^*} \quad (6.24)$$

The local acceleration parameter,  $K_v$ , is defined as

$$K_v = \frac{\nu_b^*}{(u_b^*)^2} \frac{du_b^*}{dx^*} \quad (6.25)$$

where ‘\*’ indicates dimensional value. Kline et al. (1967) found that turbulent bursts appeared to cease when  $K_v$  reached a critical value of  $3.7 \times 10^{-6}$ , and Chambers et al. (1983) indicated

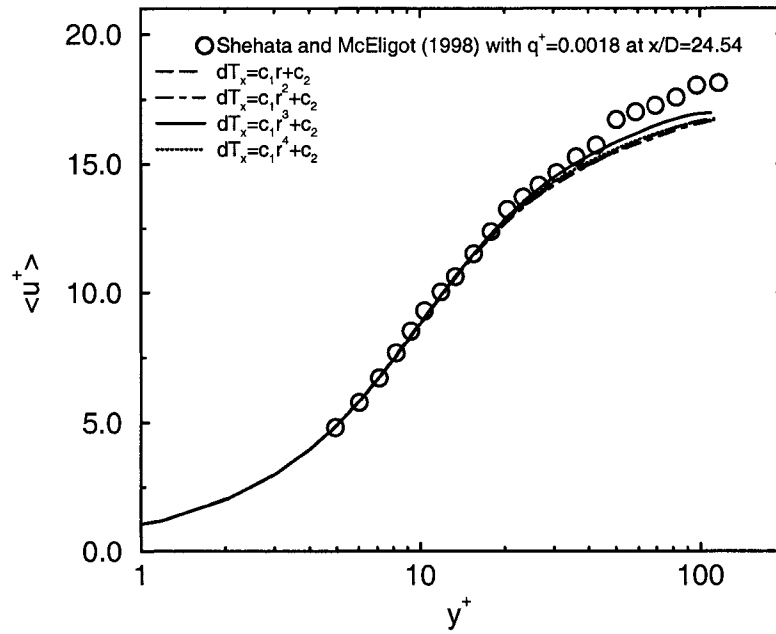


Figure 6.2 Effects of different  $\Delta T_x$  distributions on mean velocity profiles in case 4

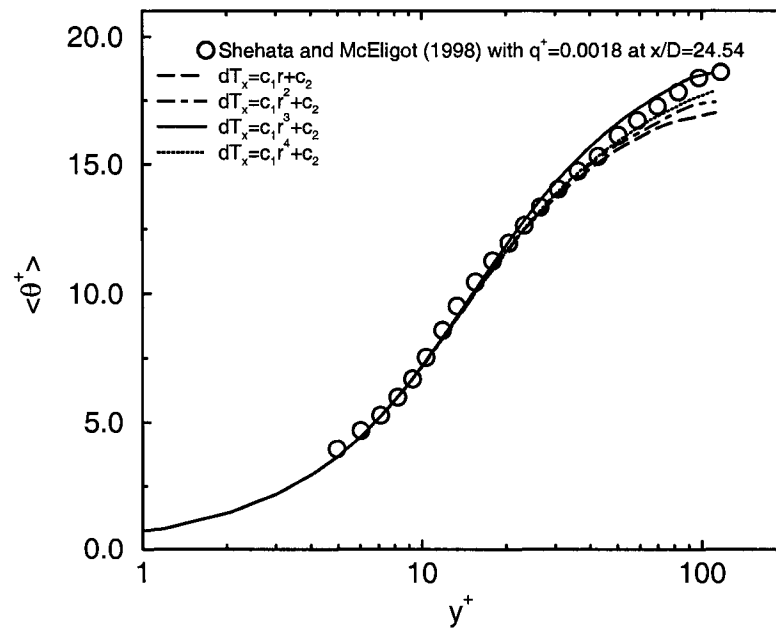


Figure 6.3 Effects of different  $\Delta T_x$  distributions on mean temperature profiles in case 4

Table 6.2 Local bulk properties for LES

Cases	$Re_b$	$T_w/T_b$	$Gr/Re_b^2$	$Nu_b$	$K_v$
1	5728.28	1.40	0.116	15.55	$9.9 \times 10^{-7}$
2	5130.51	1.91	0.15	11.04	$2.03 \times 10^{-6}$
3	3683.37	2.02	0.202	8.86	$4.6 \times 10^{-6}$
4	5401.89	1.44	0.04	13.70	$1.097 \times 10^{-6}$
5	4820.86	1.84	0.073	9.49	$2.12 \times 10^{-6}$
6	3270.6	2.09	0.246	7.32	$4.8 \times 10^{-6}$

Table 6.3 Local bulk properties for corresponding experiments

Cases	$Re_b$	$T_w/T_b$	$Gr/Re_b^2$	$Nu_b$	$K_v$
618 (x/D=14.195)	5653	1.42	0.11	15.57	$1.2 \times 10^{-6}$
635 (x/D=19.87)	5037	1.88	0.13	11.40	$2.2 \times 10^{-6}$
445 (x/D=14.195)	3595	1.96	0.3	9.5	$4 \times 10^{-6}$
618 (x/D=24.54)	5408	1.43	0.09	13.6	$1.15 \times 10^{-6}$
635 (x/D=24.54)	4894	1.89	0.12	10.21	$2.1 \times 10^{-6}$
445 (x/D=24.54)	3280	1.97	0.19	7.45	$3.56 \times 10^{-6}$

that the bursting rate remained approximately constant at the turbulent value when  $K_v$  was about  $1.5 \times 10^{-6}$ . Therefore, by these criteria, the current simulations were located in the region from fully turbulent to “laminarizing”.

### 6.6.2 Mean Profile

To further validate the present approach, the mean streamwise velocity and temperature distributions were compared with the experimental results obtained by Shehata and McEligot (1998). Profiles of the mean streamwise velocity in the wall coordinates (indicated by the ‘+’ superscripts for y and u) where

$$u^+ = \frac{u^*}{u_\tau^*}, \quad u_\tau^* = \sqrt{\frac{\tau_w^*}{\rho_w^*}}, \quad y^+ = \frac{(R^* - r^*)u_\tau^*}{\nu_w^*} \quad (6.26)$$

are plotted in Fig. 6.4-6.9 for cases 1-6, respectively. The superscript, ‘\*’, in Eq. 6.26 denotes the dimensional value. The results agree well with the experimental profiles.

By putting the profiles of these cases together with that of the low heating case, as shown in Fig. 6.10, the viscous velocity layer is getting thicker with the increasing of heat transfer. The viscous layer used here follows the definition suggested by Bradshaw (1971), which includes both the so-called ‘linear’ layer, where molecular effects dominate, and the next region where molecular effects are still significant but not dominant. According to Vogel and Eaton (1984), the viscous velocity layer is responsible for the main thermal resistance in the flow and the Nusselt number falls if the viscous velocity layer thickens. The same trend was observed in this research.

For flows with significant property variations, using semi-local coordinates (indicated by the ‘\*’ superscripts for  $y$  and  $u$ ) where

$$u^* = \frac{u^*}{(u_\tau^*)^*}, \quad (u_\tau^*)^* = \sqrt{\frac{\tau_w^*}{\rho^*(r)}}, \quad y^* = \frac{(R^* - r^*)(u_\tau^*)^*}{(\nu(y))^*} \quad (6.27)$$

is recommended by Huang et al. (1995) for removing property variation effects. The superscript, ‘\*’, in Eq. 6.27 indicates the dimensional value. The mean velocity profiles in semi-local coordinates are plotted in Fig. 6.11 for cases 1-6 and the low heating case. The velocity profiles have nearly collapsed to the profile for incompressible case, but some discrepancies are still observed in the logarithmic region.

The mean temperature difference is given in wall coordinates as

$$\theta^+ = \frac{T^* - T_w^*}{T_\tau^*}, \quad T_\tau^* = \frac{q_w^*}{\rho_w^* c_p^* u_\tau^*} \quad (6.28)$$

and the distributions of  $\theta^+$  for cases 1-6 are shown in Fig. 6.12-6.17, respectively. The figures show good agreement between experimental results and the LES simulations. The trend toward laminarization can be observed in Fig. 6.18 where the temperature profiles for all seven cases are compared with a temperature profile for a laminar flow. The result for the highest heating case, 6, is seen to fall close to the laminar profile. The log-linear region has nearly vanished for case 6.

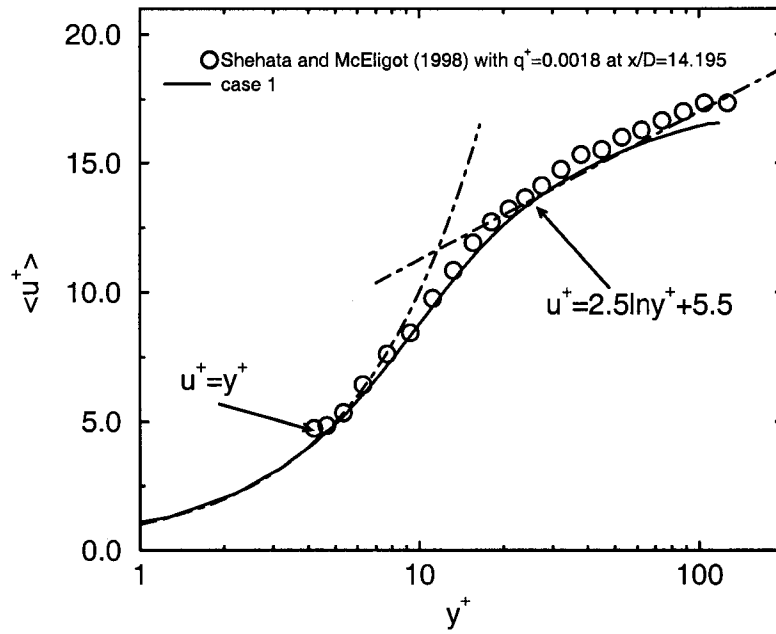


Figure 6.4 Comparison of mean velocity between case 1 and experimental case 618

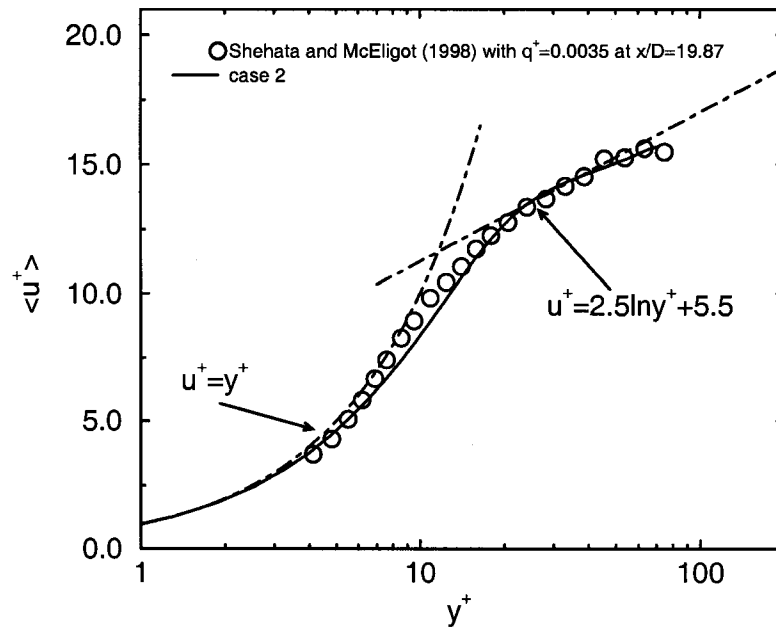


Figure 6.5 Comparison of mean velocity between case 2 and experimental case 635

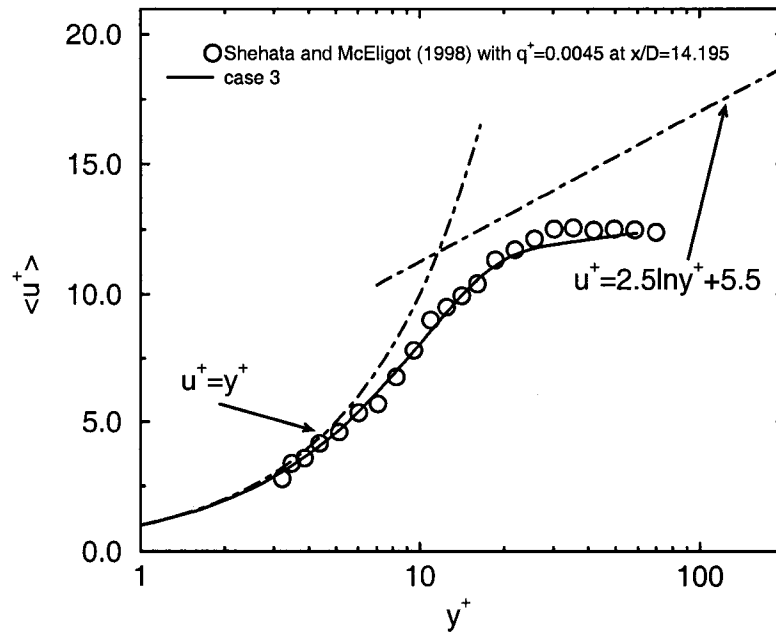


Figure 6.6 Comparison of mean velocity between case 3 and experimental case 445

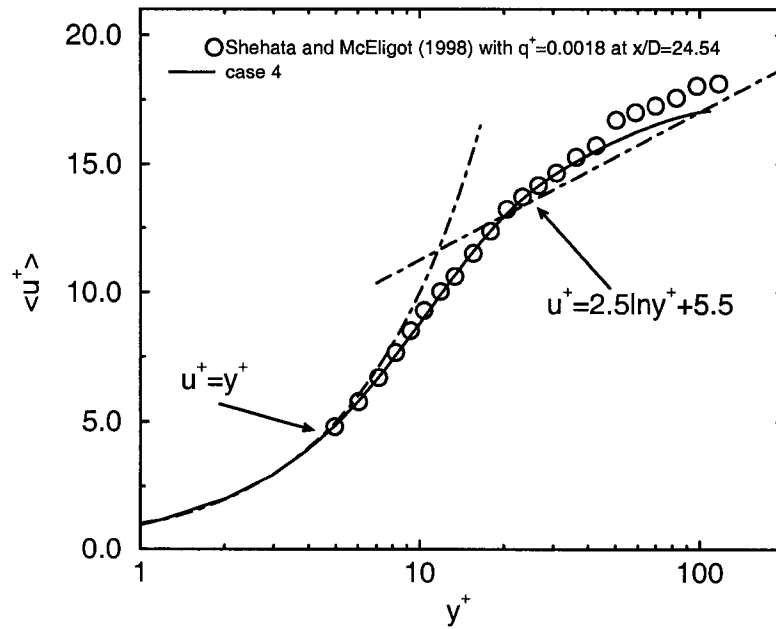


Figure 6.7 Comparison of mean velocity between case 4 and experimental case 618

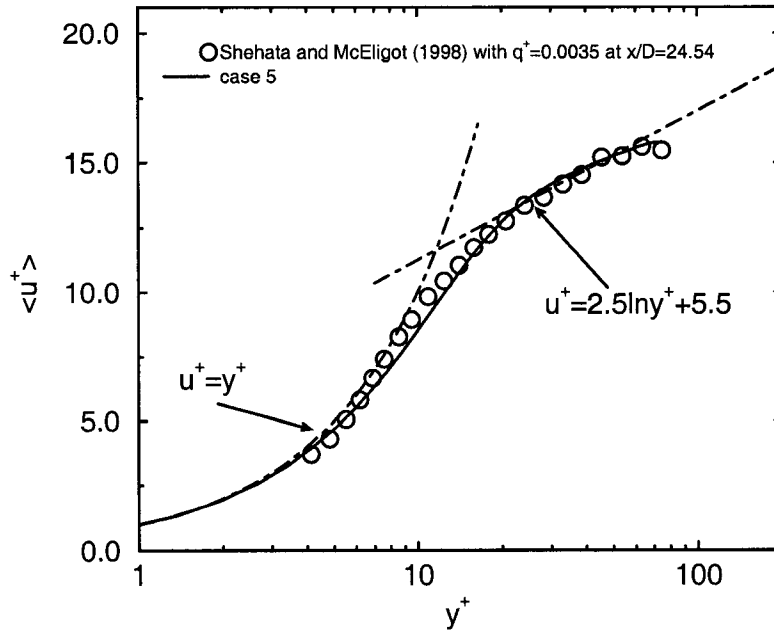


Figure 6.8 Comparison of mean velocity between case 5 and experimental case 635

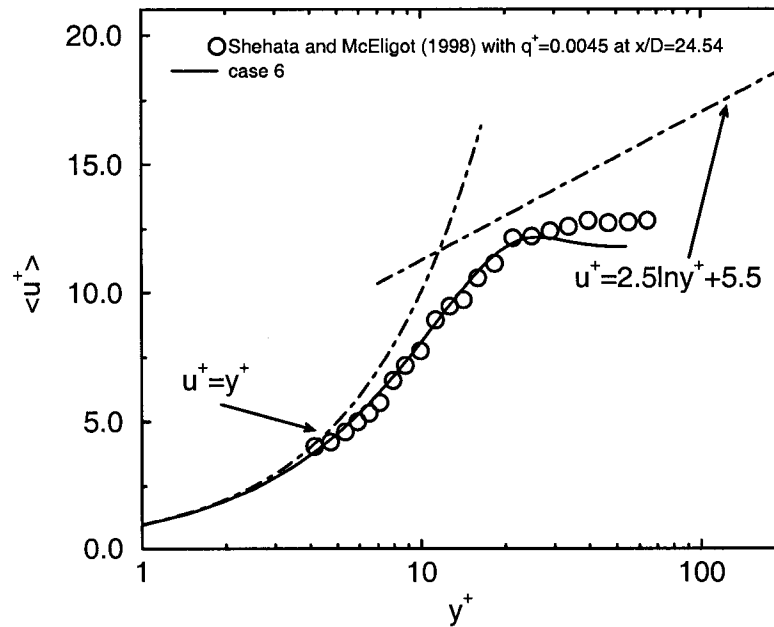


Figure 6.9 Comparison of mean velocity between case 6 and experimental case 445

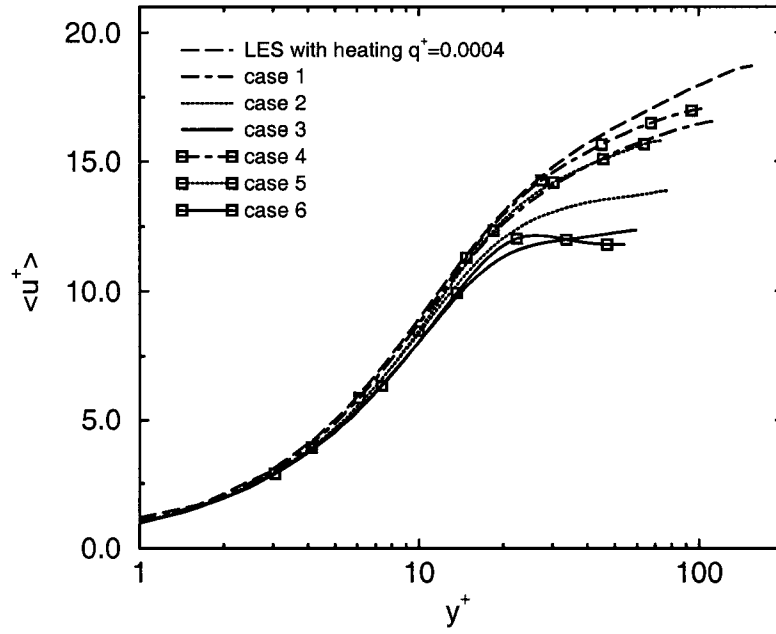


Figure 6.10 Mean velocity profiles in wall coordinates

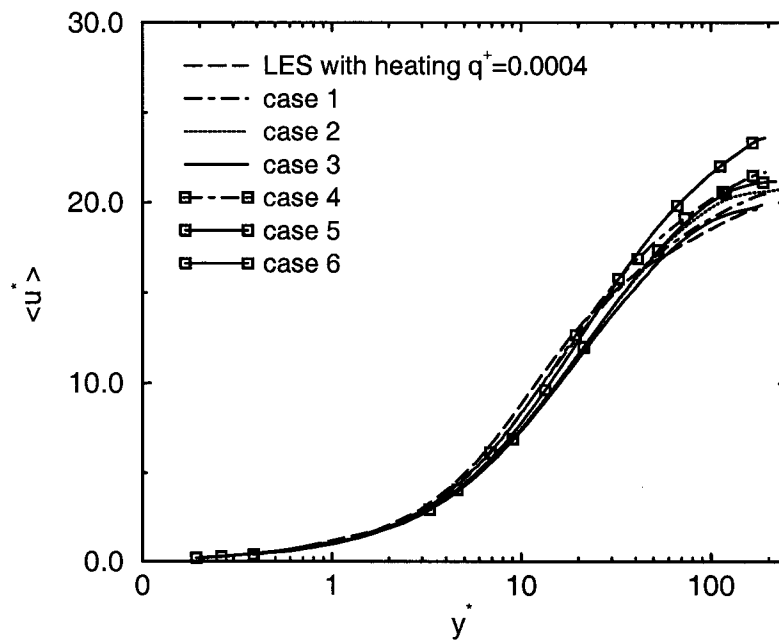


Figure 6.11 Mean velocity profiles in semi-local coordinates

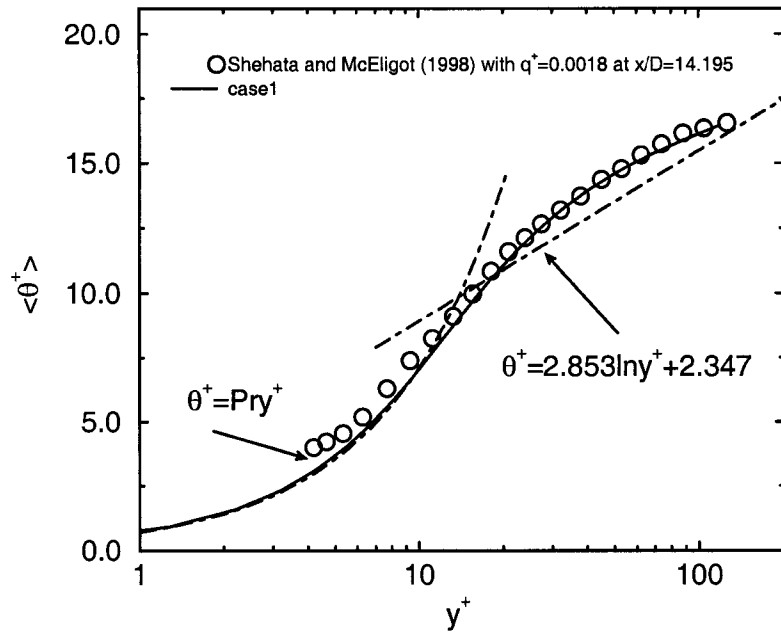


Figure 6.12 Comparison of simulated mean temperature profile of case 1 and experimental case 618

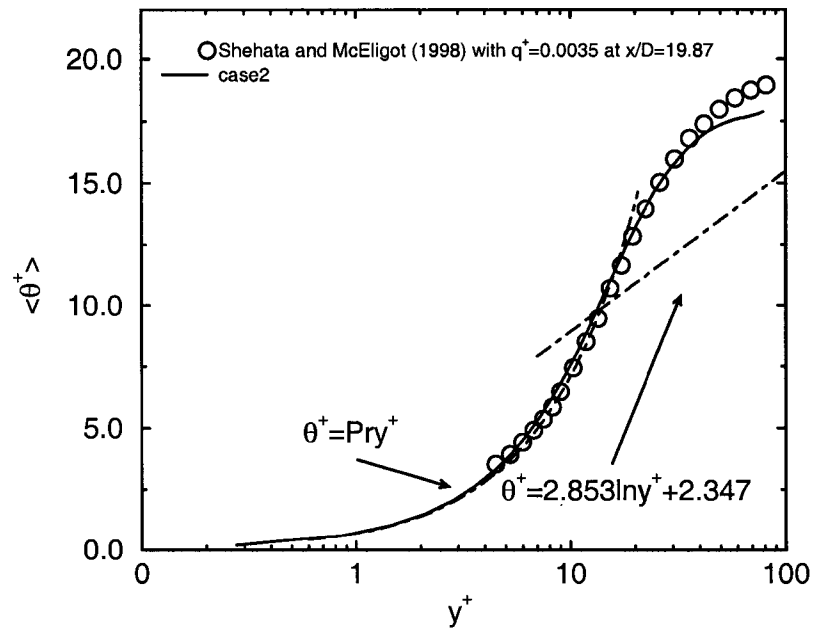


Figure 6.13 Comparison of simulated mean temperature profile of case 2 and experimental case 635

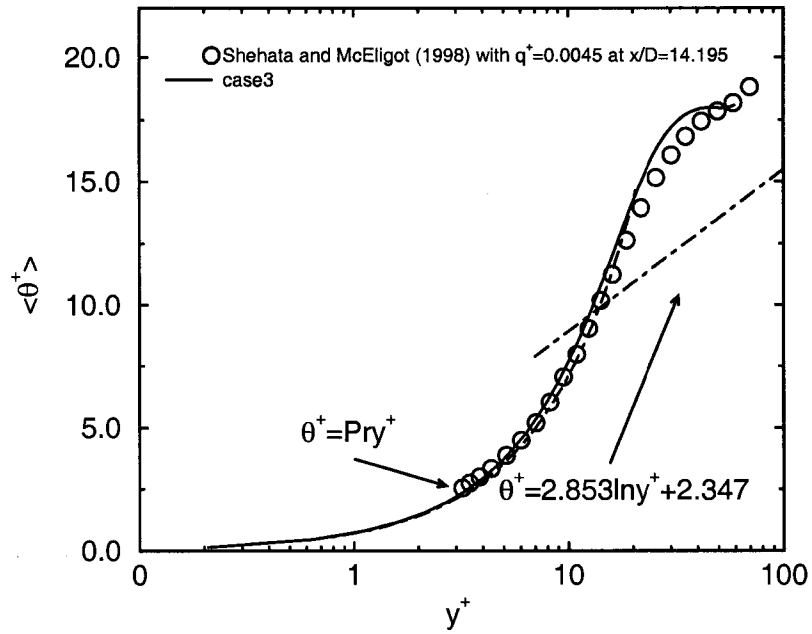


Figure 6.14 Comparison of simulated mean temperature profile of case 3 and experimental case 445

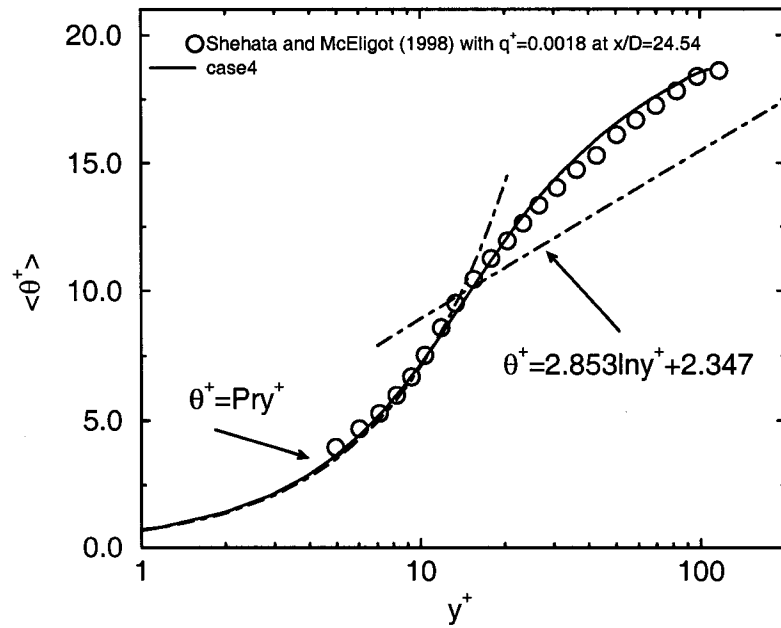


Figure 6.15 Comparison of simulated mean temperature profile of case 4 and experimental case 618

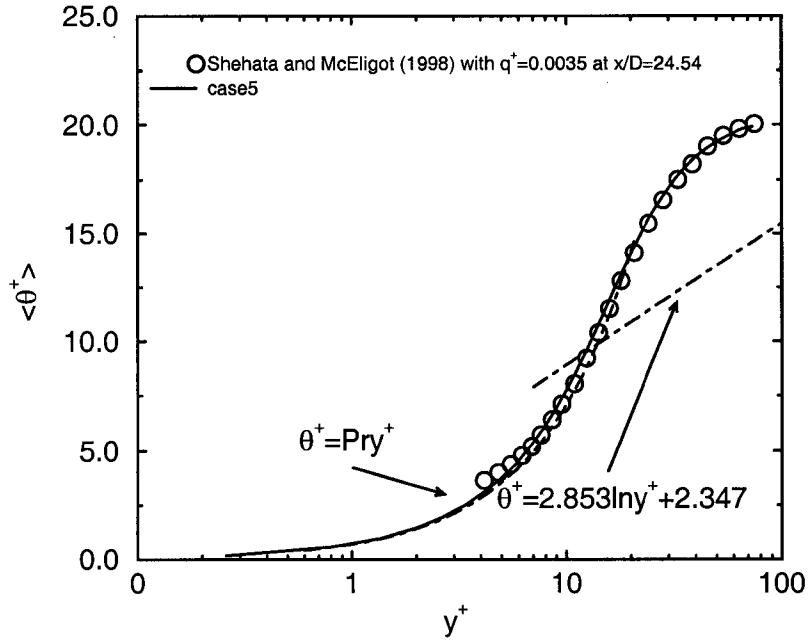


Figure 6.16 Comparison of simulated mean temperature profile of case 1 and experimental case 635

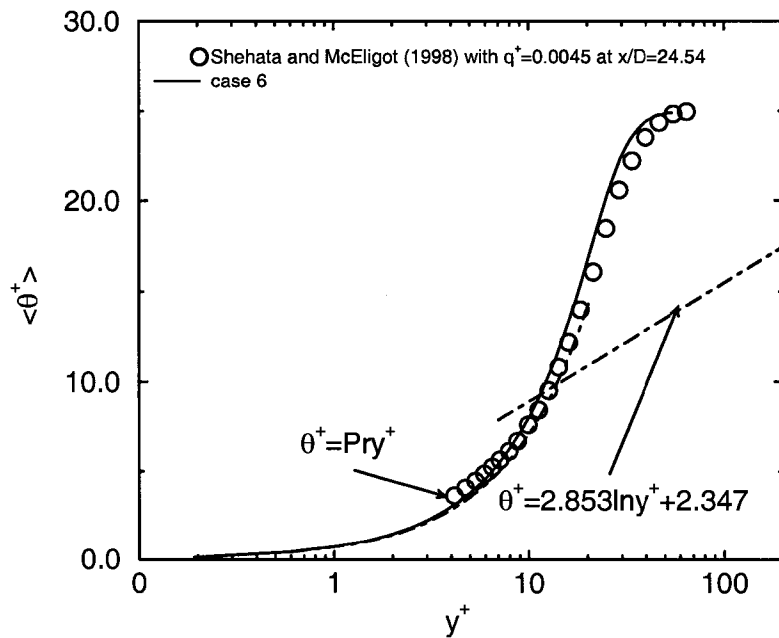


Figure 6.17 Comparison of simulated mean temperature profile of case 2 and experimental case 445

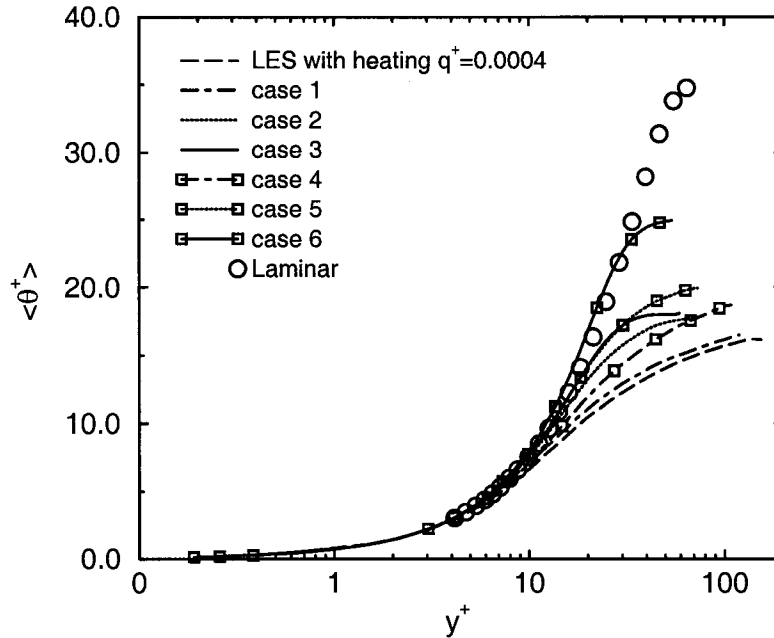


Figure 6.18 Mean temperature in wall coordinates

The mean temperature profiles normalized by the bulk temperature and the mean density profiles normalized by bulk density are shown in Fig. 6.19 and Fig. 6.20, respectively. It was observed that significant variations of temperature led to significant variations in density. The distributions of the mean streamwise momentum,  $\langle \rho u \rangle$ , in cases 1-6 are plotted in Fig. 6.21, which shows that the profile was fairly flat when the heating rate was small. However, the profile became really parabolic when the nondimensional heating rate was  $q^+ = 0.0045$ . The mass flow was redistributed toward the center of pipe due to the high heating.

### 6.6.3 Fluctuation Profiles

The velocity fluctuations in the streamwise, radial, and circumferential directions for the low heating case and cases 1-6 are plotted against  $y^+$  in Fig. 6.22. A comparison of these indicates that the turbulent intensities decrease as the nondimensional heating rate is increasing. This tendency is due to the fact that the local Reynolds number,  $Re_{b_x}$ , is lower for the higher heating cases. McEligot (1986) also observed that the acceleration of a turbulent flow reduces

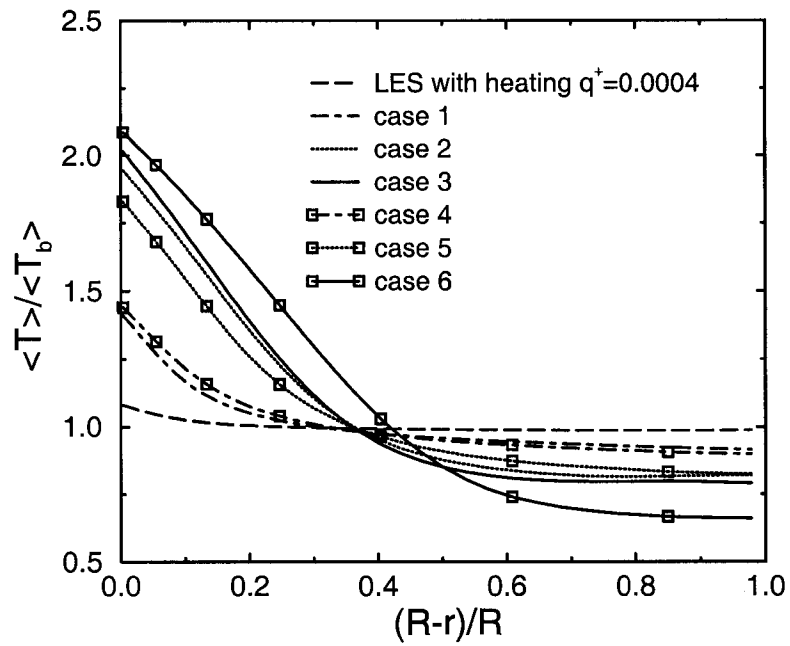


Figure 6.19 Mean temperature profiles normalized by bulk temperature

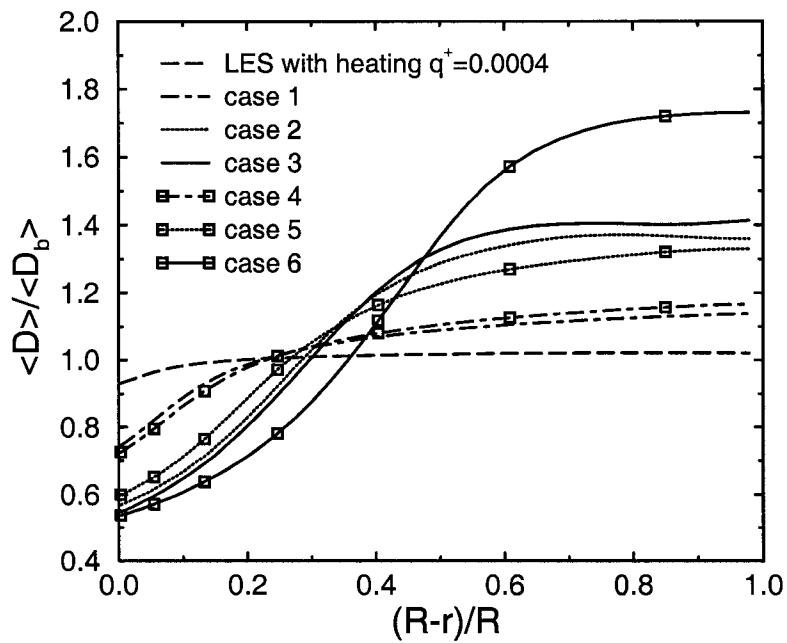


Figure 6.20 Mean density profiles normalized by bulk density

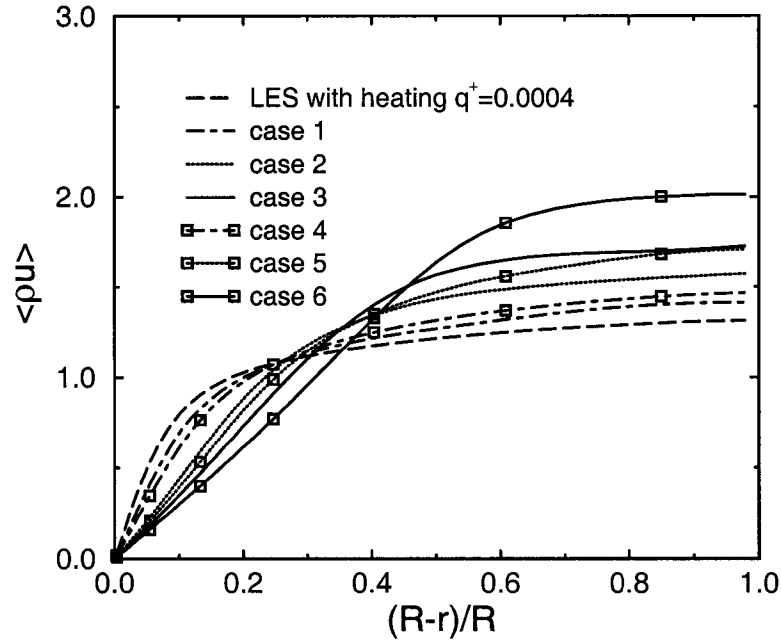


Figure 6.21 Mean streamwise momentum profiles

the apparent turbulent bursting rate near the wall, which will lead to the suppression of velocity fluctuations. Consequently, the larger acceleration parameter,  $K_v$ , results in lower turbulence intensities. The same trend was found in this research. The velocity fluctuations in semi-local coordinates are plotted in Fig. 6.23. A smaller departure from the results of the low heating case is observed.

The turbulent kinetic energy (TKE) in wall coordinates is plotted for the low heating case and cases 1-6 in Fig. 6.24. The turbulent kinetic energy was attenuated dramatically when the heat flux was high. Such a decrease in TKE corresponds to the effectively thickened viscous layers, where molecular momentum transport dominated. The attenuation in the TKE profiles is quite evident for case 3 and case 6 as it was for the *rms* profiles. Figure 6.25 shows the turbulent kinetic energy in semi-local coordinates; the same trend was observed as for the *rms* profiles in semi-local coordinates.

#### 6.6.4 Shear Stress and Heat Flux Profiles

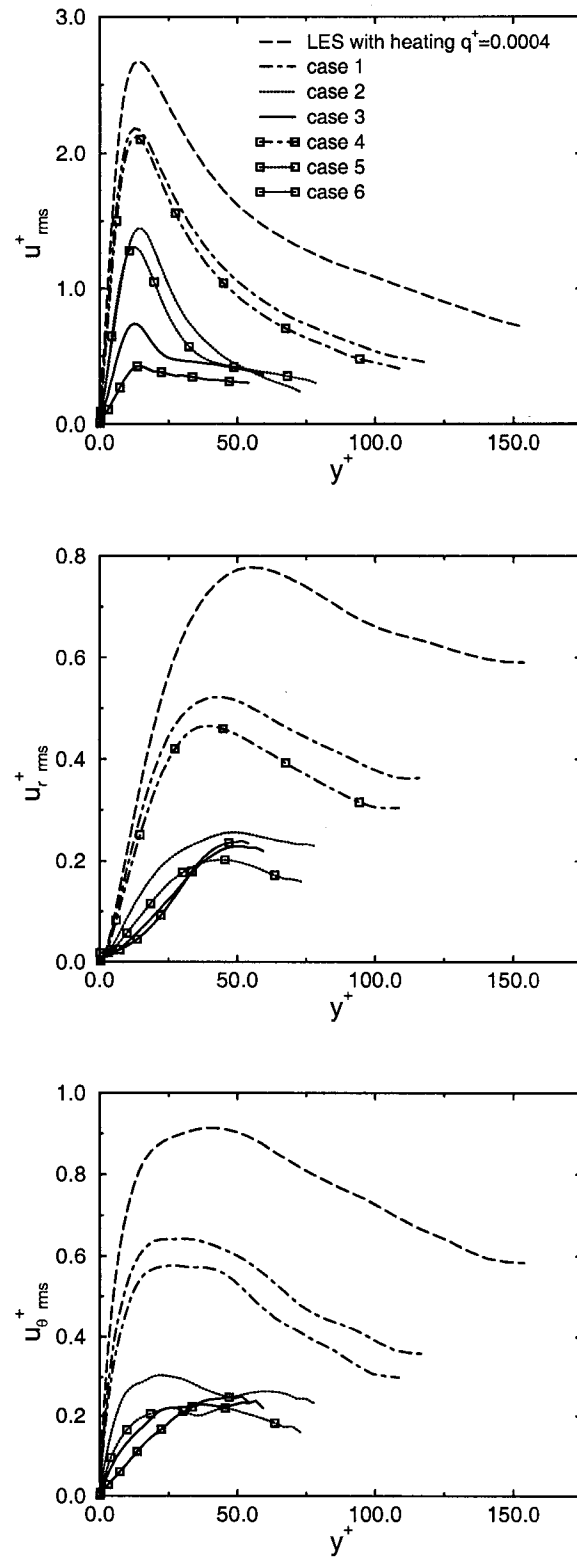


Figure 6.22 Velocity fluctuations in wall coordinates

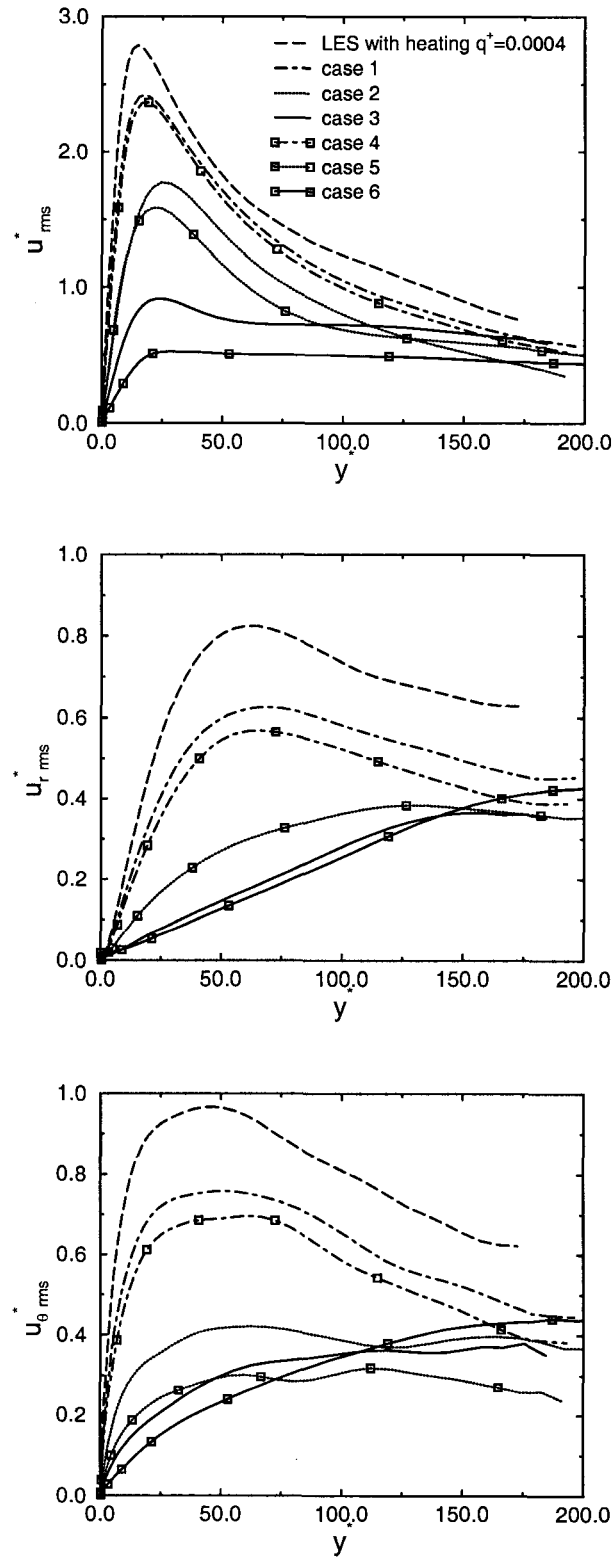


Figure 6.23 Velocity fluctuations in semi-local coordinates

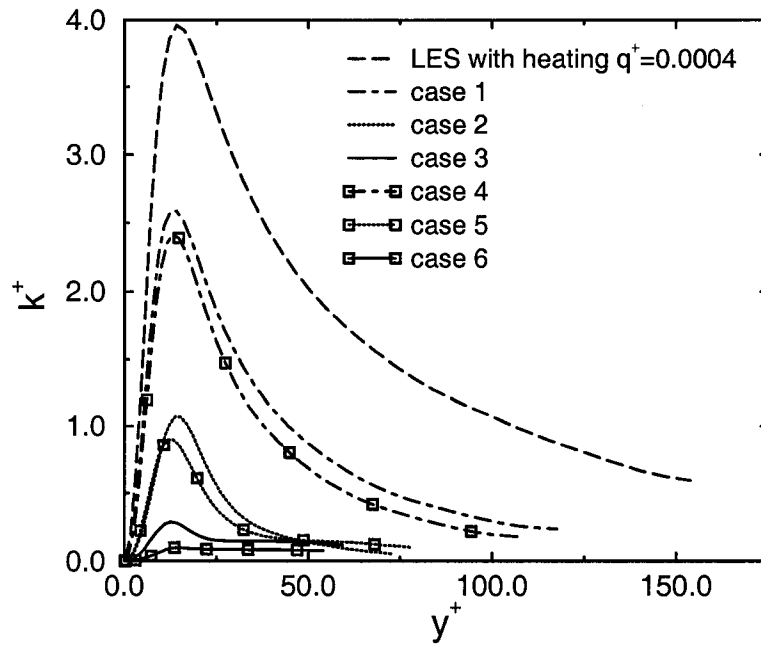


Figure 6.24 Turbulent kinetic energy in wall coordinates

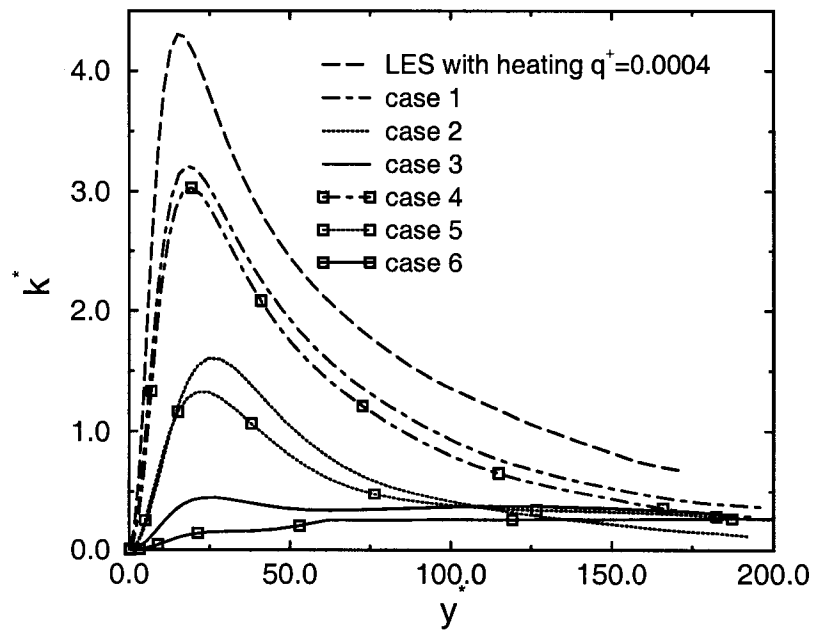


Figure 6.25 Turbulent kinetic energy in semi-local coordinates

Figure 6.26 shows the resolved, viscous, and SGS shear stress profiles normalized by the wall shear stress. The shear stresses are defined as

$$\tau_{res} = - \langle \rho u'' u_r'' \rangle \quad (6.29)$$

$$\tau_{vis} = - \langle \frac{\mu}{Re} \frac{\partial u}{\partial r} \rangle \quad (6.30)$$

$$\tau_{sgs} = - \langle \mu_t \frac{\partial u}{\partial r} \rangle \quad (6.31)$$

where  $''$  denotes the Favre average. As shown in the figure, shear stresses were decreasing when the heat fluxes were increasing. Very small resolved shear stress and modeled SGS shear stress were observed for case 3 and case 6, which may indicate that laminarization has occurred.

The resolved heat flux, heat conduction, and modeled SGS heat flux distributions normalized by the wall heat flux are shown in Fig. 6.27, where

$$q_{res} = - \langle \rho u_r'' T'' \rangle \quad (6.32)$$

$$q_{con} = - \langle \frac{\mu c_p}{Re Pr} \frac{\partial T}{\partial r} \rangle \quad (6.33)$$

$$q_{sgs} = - \langle \frac{\mu_t c_p}{Pr_t} \frac{\partial T}{\partial r} \rangle \quad (6.34)$$

The same trends were observed as for shear stresses.

The sum of the three shear stress contributions and the sum of three heat flux contributions are shown in Fig.6.28 and Fig.6.29, respectively. For fully developed turbulent flow, the sum of shear stresses or heat fluxes represents the complete contributions to the total shear stress or total heat flux, which is linear distribution as shown in Chapter 4. The linear distribution was observed in low heating case due to the very small property variation and the flow could be approximately fully developed as incompressible turbulent pipe flow. However, for the high heating cases, no truly fully developed conditions are reached because the temperature increases lead to continuous axial and radial property variations. Other terms could be contributing to the shear stress and heat flux balance for the quasi-developed flows computed. Consequently, large departures from the linear distribution were observed for high heating cases, especially for cases with nondimensional heating rates of  $3.5 \times 10^{-3}$  and  $4.5 \times 10^{-3}$ .

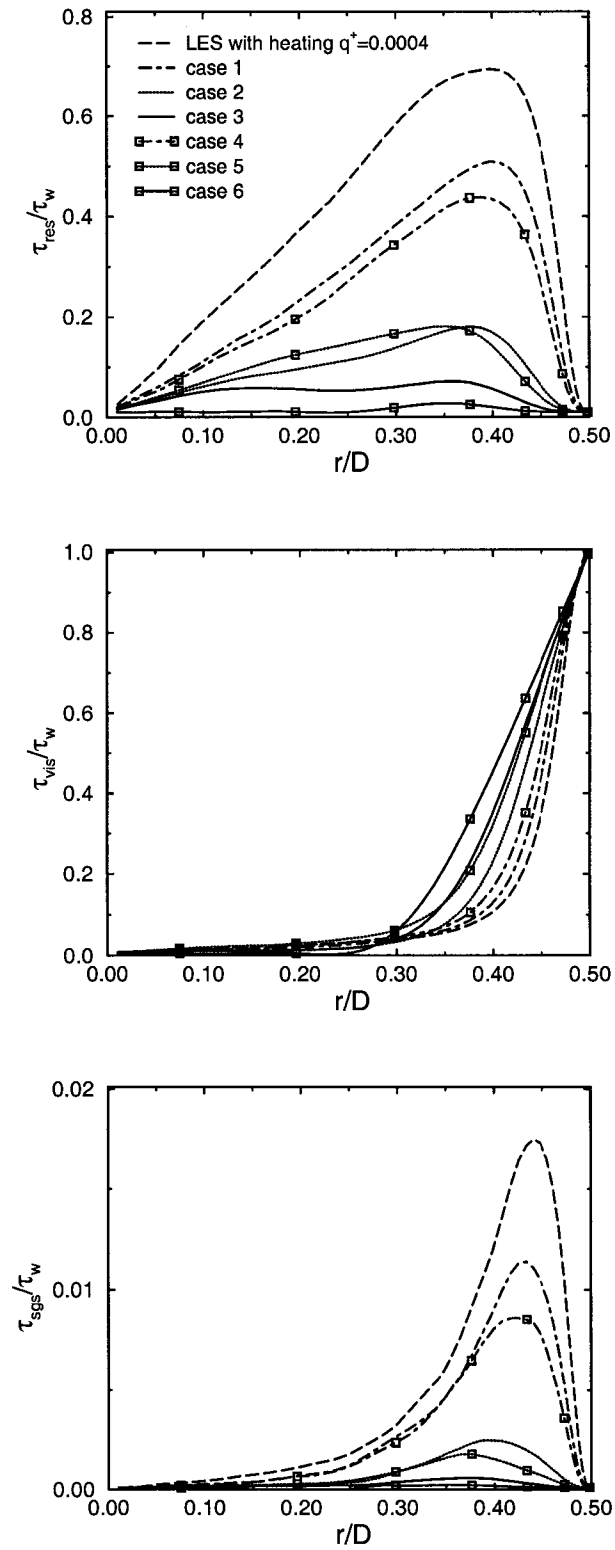


Figure 6.26 Shear stress distributions normalized by wall shear stress

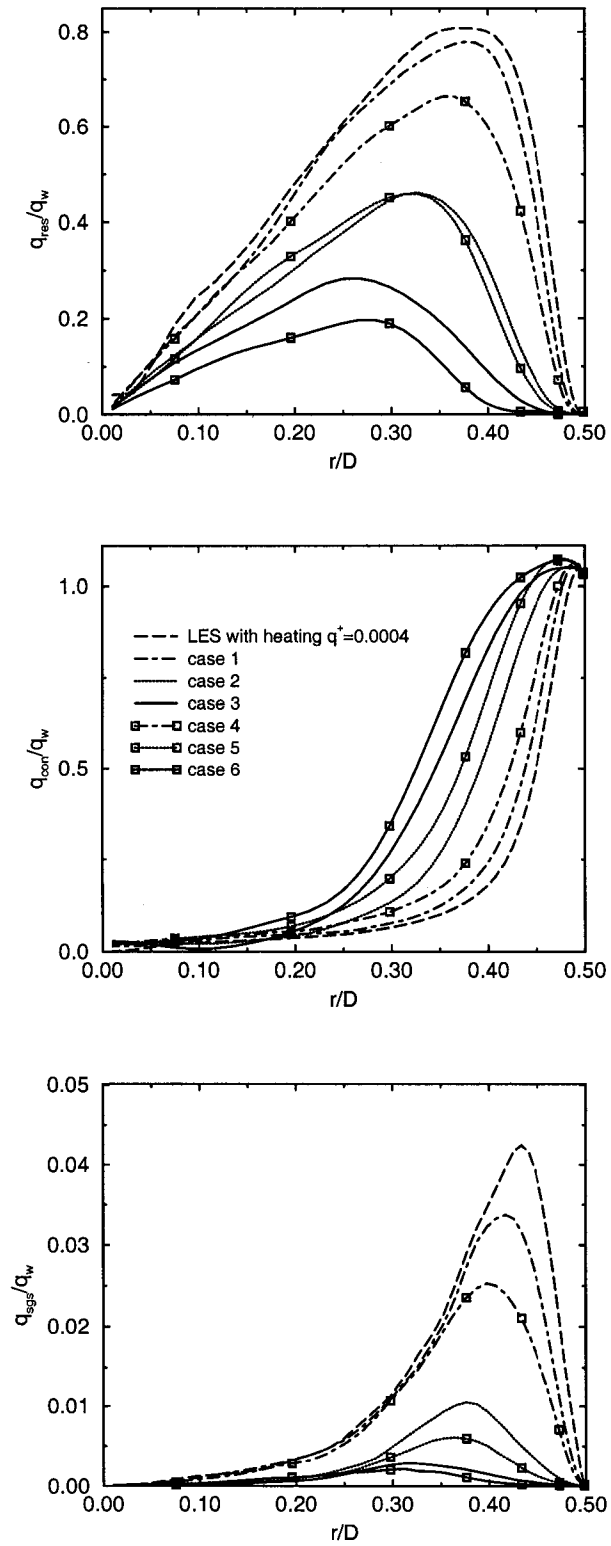


Figure 6.27 Heat flux distributions normalized by wall heat flux

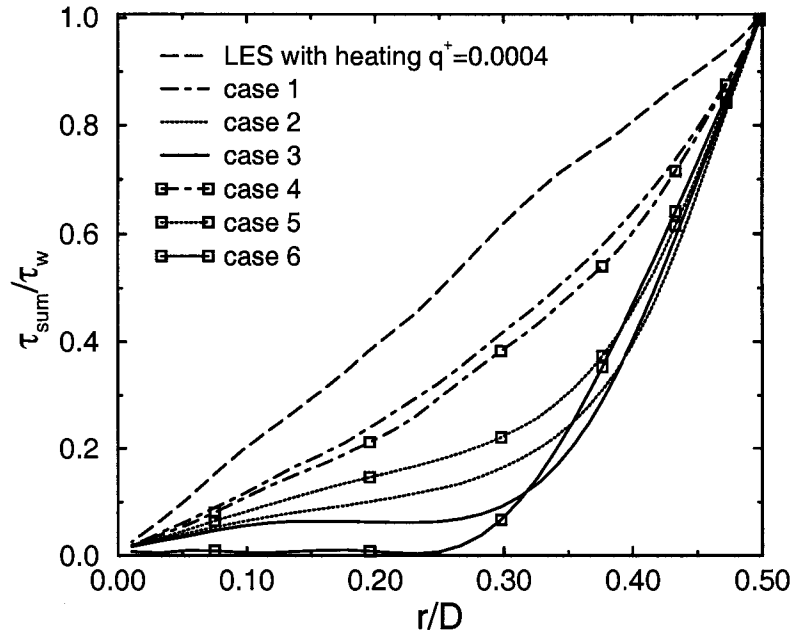


Figure 6.28 Sum of resolved, viscous, and SGS shear stresses contributions normalized by wall shear stress

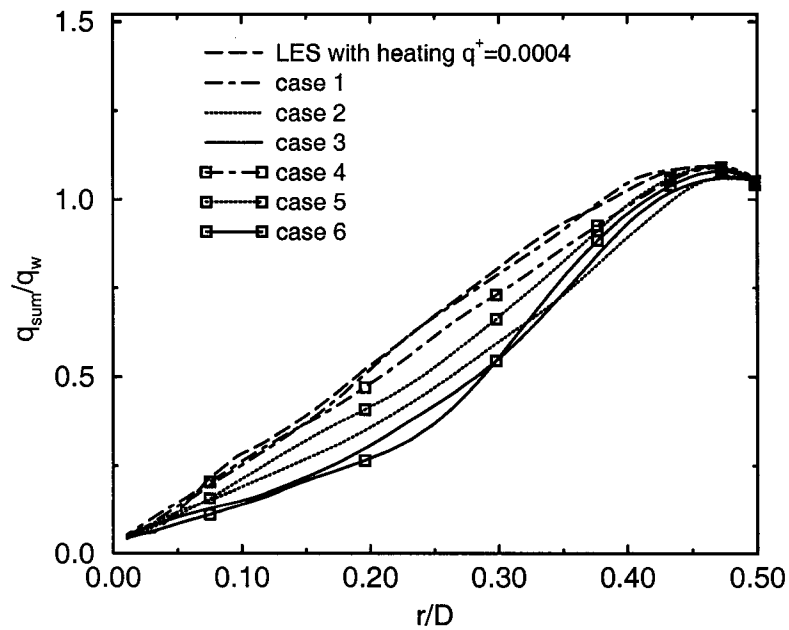


Figure 6.29 Sum of resolved, conductive, and SGS heat flux distributions normalized by wall heat flux

## 6.7 Instantaneous Results

The nondimensional instantaneous velocity and temperature contours of cases 1-6 are presented in this section to help explain some of the trends observed in the ensemble averaged results.

The nondimensional instantaneous streamwise velocity contours for cases 1-6 are plotted in Fig. 6.30 through Fig. 6.35, respectively. The  $y$ - $z$  plane is located at the middle of the pipe; the plane in the circumferential direction is at  $r/R = 0.96$ . The low-speed streaky structure is clearly evident in the near wall region ( $y^+ < 5$ ) in cases 1 and 4, which reveals that very strong turbulence “bursting action” exists in the near wall region leading in turn to high turbulent kinetic energy. However, the streaky structure is not obvious for cases 2 and 5 and no streaky structure can be seen for cases 3 and 6, which may be evidence of “laminarization”. More isotropic structures were observed in the core region of the pipe for all cases.

Figures 6.36 through Fig. 6.41 show the nondimensional instantaneous temperature contours of cases 1-6, respectively. The locations of the  $y$ - $z$  plane and circumferential plane are the same as that for the velocity contours plots. The bursting phenomenon is also evident in the near wall region for cases 1 and 4, which indicates the ejection of hotter fluid into the regions away from the wall.

The nondimensional velocity vector plots in the middle plane of the pipe for cases 1-6 are shown in Fig. 6.42 through Fig. 6.47, respectively. Figure 6.42 and 6.45 clearly show the large scale motions near the wall region in cases 1 and 4. For cases 2 and 5, the large eddies moved toward center of the pipe and the eddies are smaller and not obvious compared to those in cases 1 and 4. The vector plots for cases 3 and 6 are similar to that of laminar pipe flow, almost no large scale motion was observed, which may suggest that “laminarization” has occurred.

## 6.8 Friction Coefficient and Nusselt Number

In this section, the friction coefficients and Nusselt numbers are compared to several correlations with property variations. The property ratio method is used here to correct the constant property correlations for variable property effects. For gases, the property ratio method is

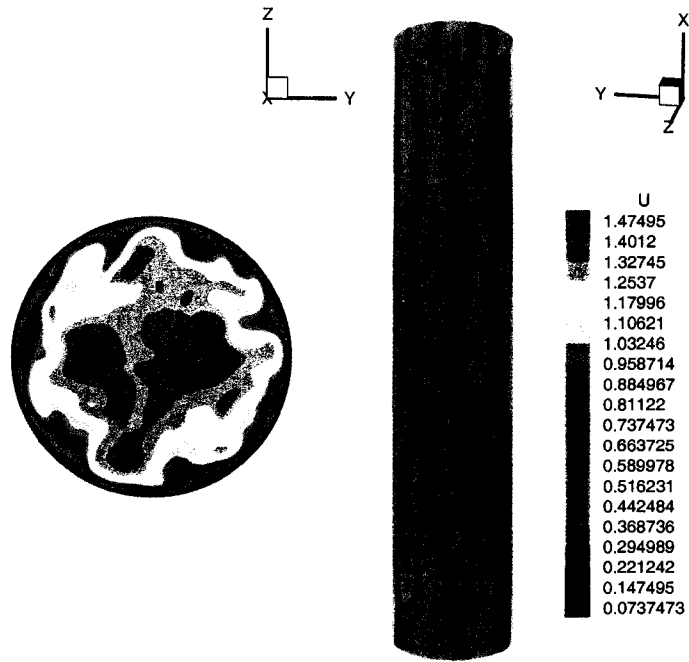


Figure 6.30 Instantaneous streamwise velocity for case 1

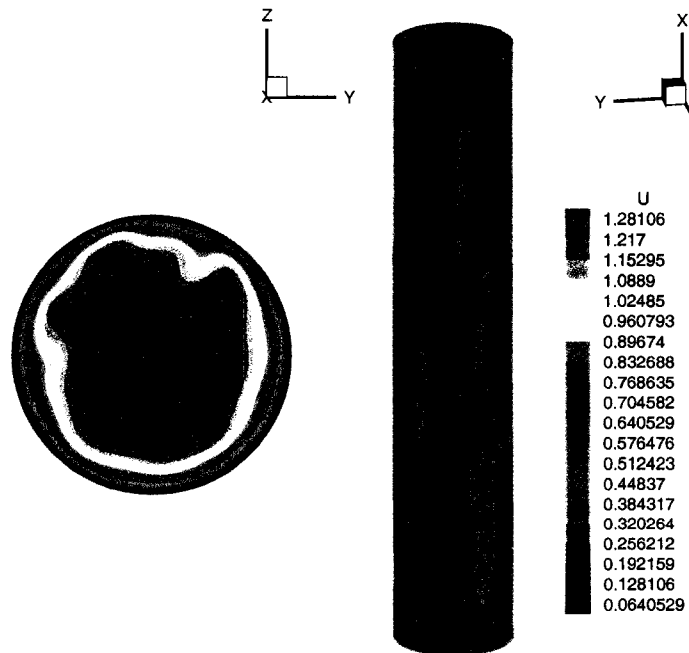


Figure 6.31 Instantaneous streamwise velocity for case 2

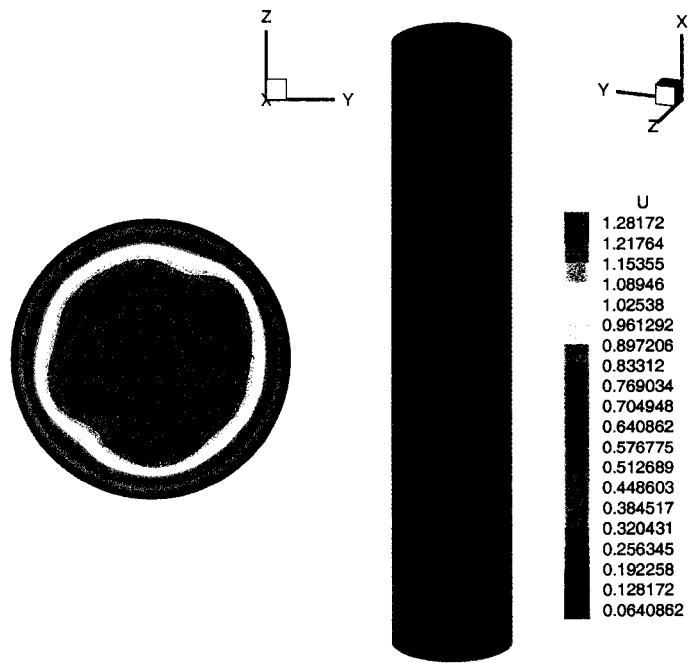


Figure 6.32 Instantaneous streamwise velocity for case 3

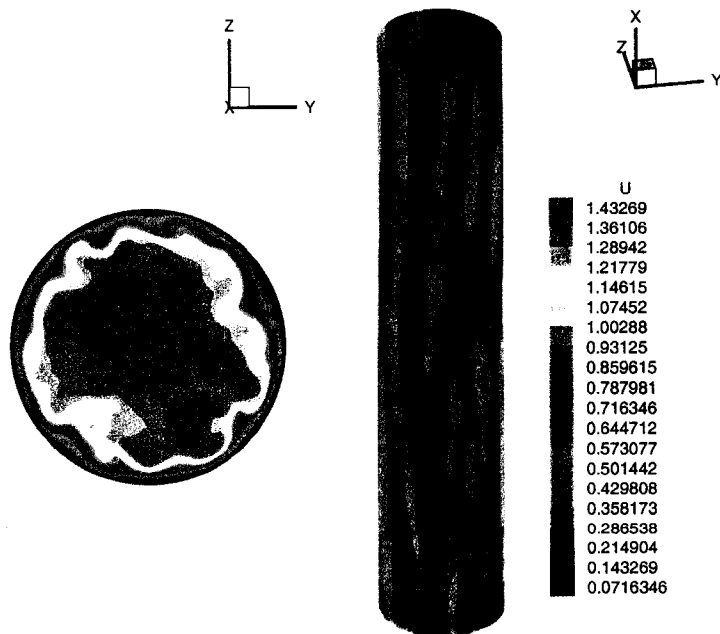


Figure 6.33 Instantaneous streamwise velocity for case 4

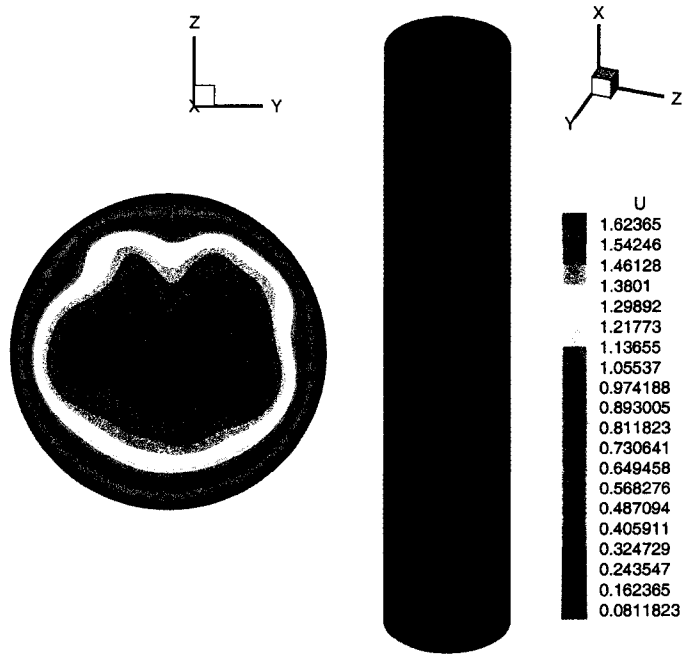


Figure 6.34 Instantaneous streamwise velocity for case 5

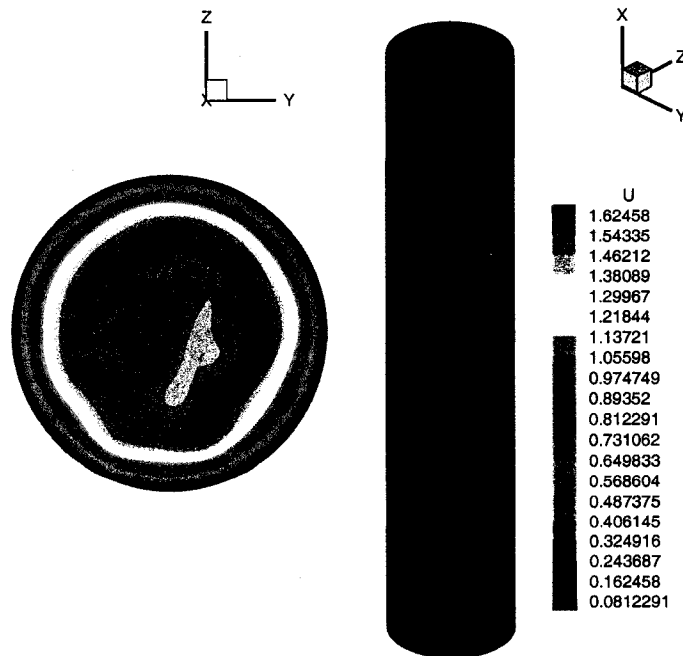


Figure 6.35 Instantaneous streamwise velocity for case 6

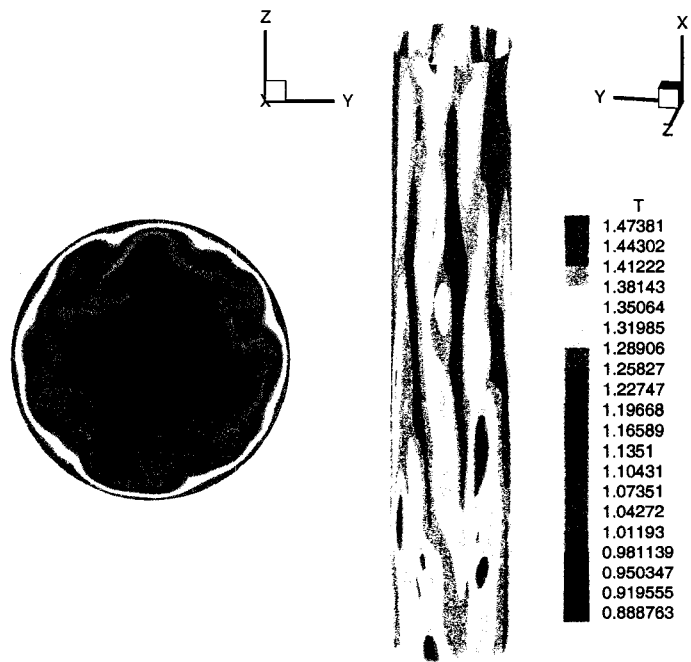


Figure 6.36 Instantaneous temperature for case 1

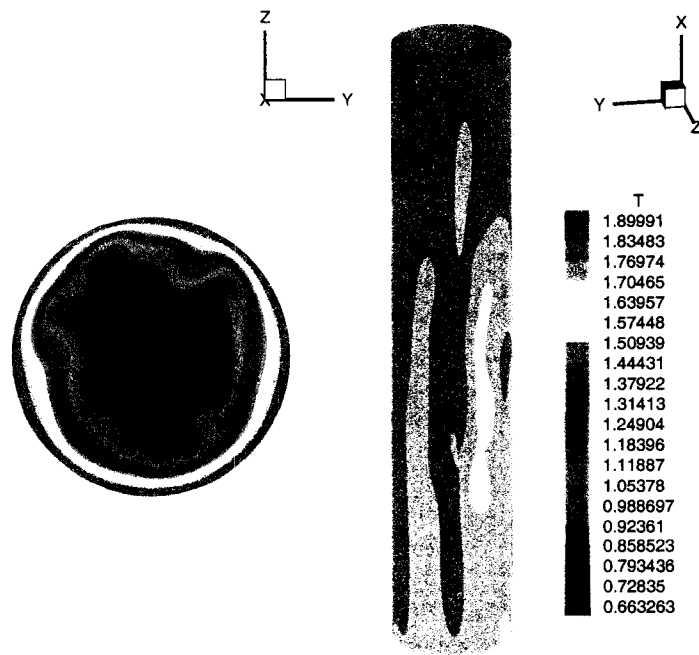


Figure 6.37 Instantaneous temperature for case 2

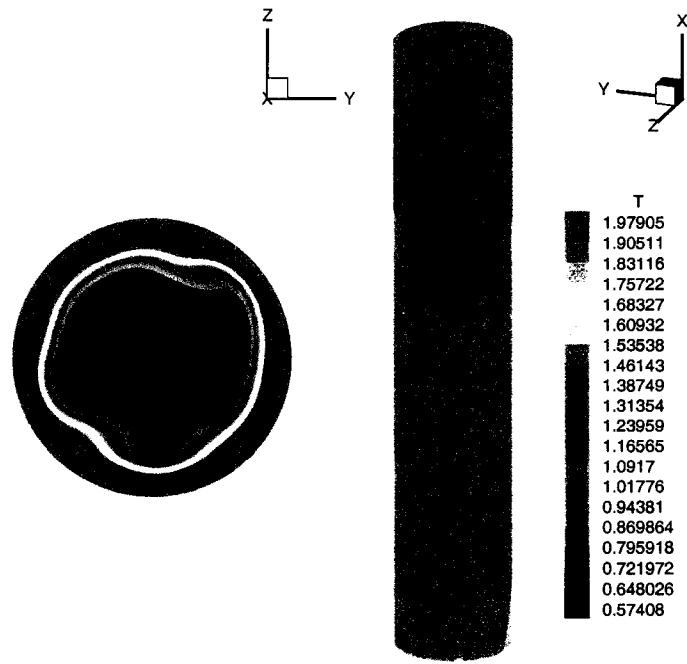


Figure 6.38 Instantaneous temperature for case 3

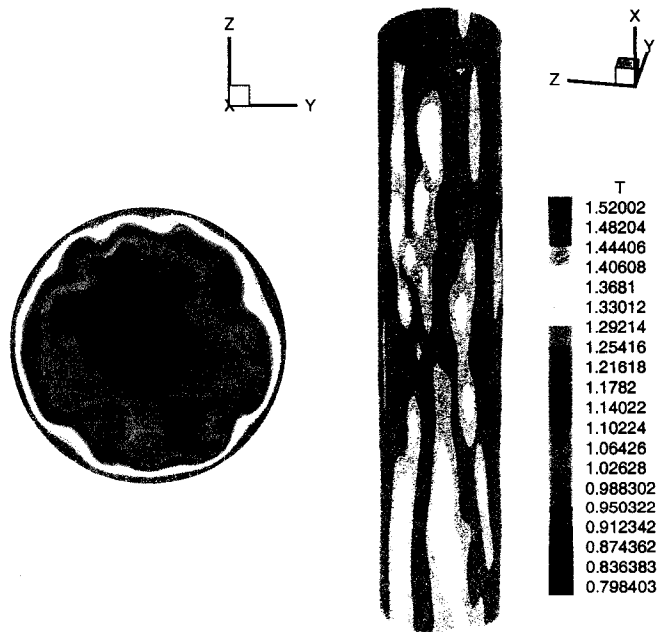


Figure 6.39 Instantaneous temperature for case 4

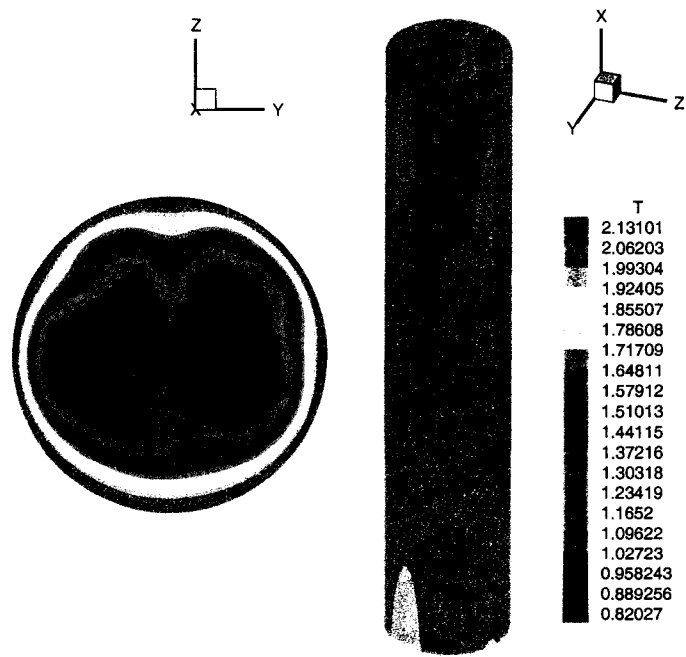


Figure 6.40 Instantaneous temperature for case 5

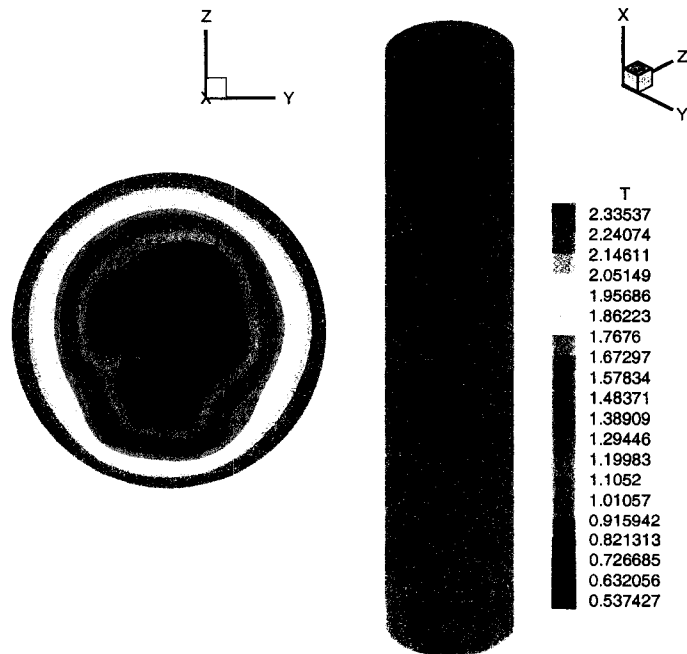


Figure 6.41 Instantaneous temperature for case 6

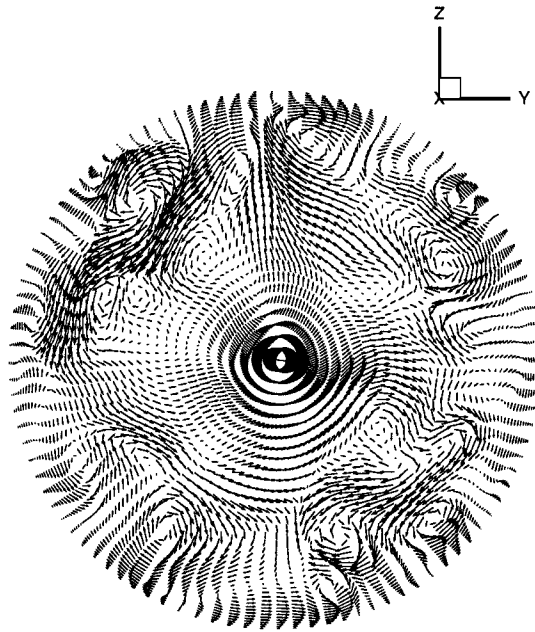


Figure 6.42 Instantaneous velocity vector plot for case 1

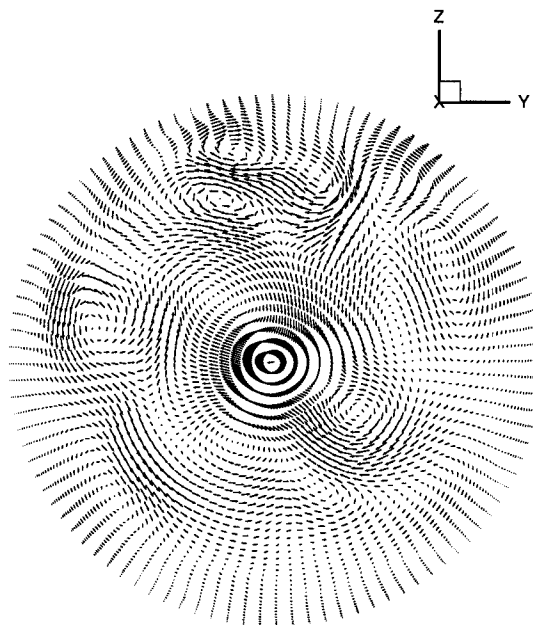


Figure 6.43 Instantaneous velocity vector plot for case 2

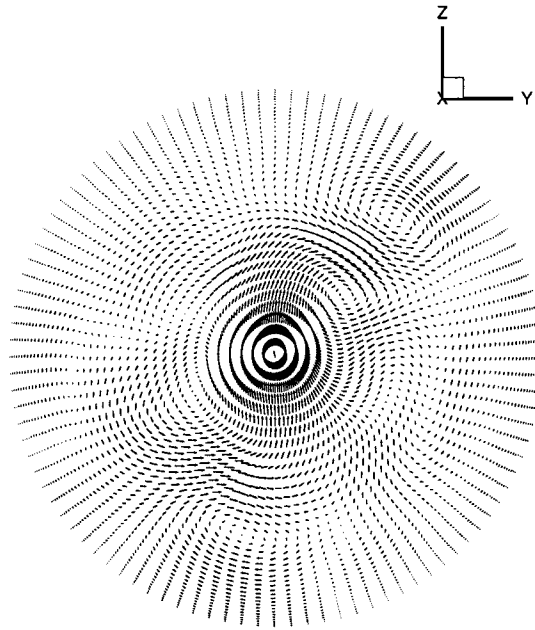


Figure 6.44 Instantaneous velocity vector plot for case 3

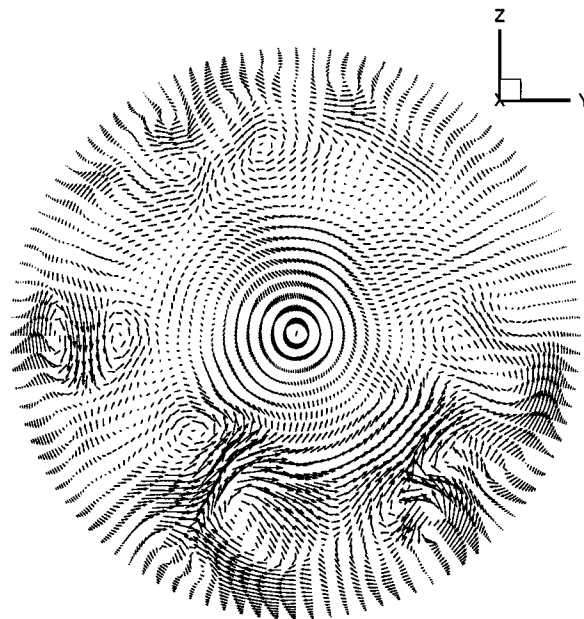


Figure 6.45 Instantaneous velocity vector plot for case 4

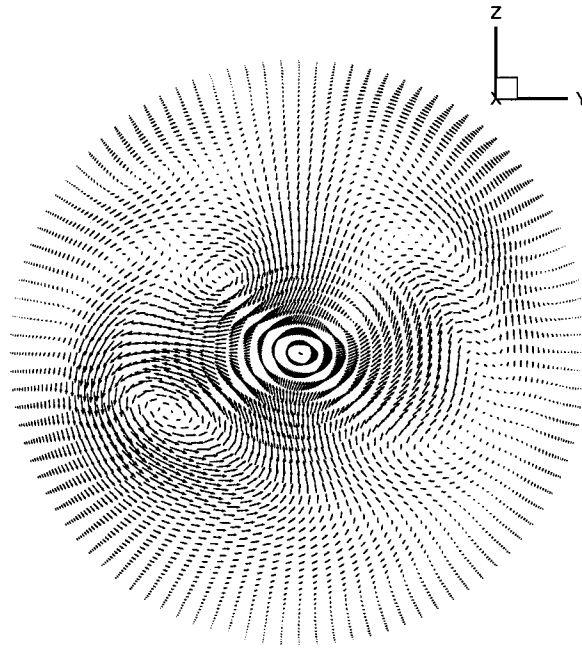


Figure 6.46 Instantaneous velocity vector plot for case 5

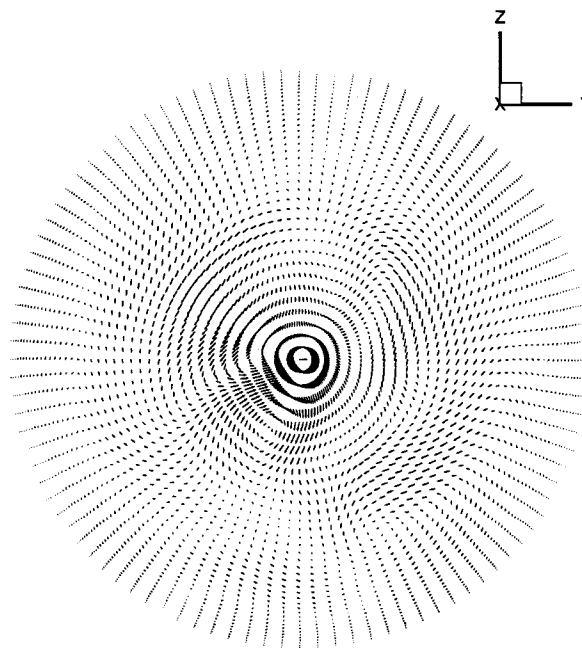


Figure 6.47 Instantaneous velocity vector plot for case 6

defined as

$$\frac{f}{f_{cp}} = \left( \frac{T_w}{T_b} \right)^m \quad (6.35)$$

$$\frac{Nu}{Nu_{cp}} = \left( \frac{T_w}{T_b} \right)^n \quad (6.36)$$

where the subscript  $cp$  refers to the corresponding constant property correlation.

Petukhov and Popov (1963) proposed a variable property correlation as

$$m = -0.6 + 0.79Re_w^{-0.11} , \quad n = - \left[ 0.3 \log_{10} \frac{T_w}{T_b} + 0.36 \right] \quad (6.37)$$

with  $Nu_{cp}$  and  $f_{cp}$  given by Eq. 4.37 and Eq. 5.17, respectively. The wall Reynolds number is defined as  $Re_w = u_b^* D_h^* \rho_w^* / \mu_w^*$ .

Kays and Crawford (1993) recommend the following exponents

$$m = -0.1 , \quad n = -0.5 \quad (6.38)$$

with  $Nu_{cp}$  and  $f_{cp}$  given by Eq. 5.19 and 4.40, respectively.

The correlations for gas heating at constant wall temperature in circular ducts resulting strictly from experimental studies are expressed in the form

$$Nu_D = C Re_D^{0.8} Pr^{0.4} \left( \frac{T_w}{T_b} \right)^n \quad (6.39)$$

where  $C$  and  $n$  are constants.

A correlation provided by Humble, Lowdermilk, and Desmon (1951) valid for  $0.46 < T_w/T_b < 3.5$  and  $7 \times 10^3 < Re_D < 3 \times 10^5$  is

$$Nu_D = 0.023 Re_D^{0.8} Pr^{0.4} \left( \frac{T_w}{T_b} \right)^{-0.55} \quad (6.40)$$

Barnes and Jackson (1961) proposed a correlation

$$Nu_D = 0.023 Re_D^{0.8} Pr^{0.4} \left( \frac{T_w}{T_b} \right)^{-0.4} \quad (6.41)$$

which is valid for  $1.2 < T_w/T_b < 2.2$  and  $4 \times 10^3 < Re_D < 6 \times 10^4$  and  $L/d > 60$ .

A similar correlation is given by McEligot et al. (1965) as

$$Nu_D = 0.021 Re_D^{0.8} Pr^{0.4} \left( \frac{T_w}{T_b} \right)^{-0.5} \quad (6.42)$$

Table 6.4 Comparison with variable property correlations for case 1

Correlation	Equation	$C_f$	% diff	$Nu_D$	% diff
Present simulation	–	0.00842	–	15.55	–
Experiment (Shehata and McEligot, 1998)	–	–	–	15.57	-0.13
Humble, Lowdermilk and Desmon (1951)	Eq. 6.40	–	–	16.91	-8.04
Barnes and Jackson (1961)	Eq. 6.41	–	–	17.79	-12.59
Petukhov and Popov (1963)	Eq. 6.37	0.00836	0.7	16.2	-4.01
McEligot et al. (1965)	Eq. 6.42	–	–	15.7	-0.96
Kays and Crawford (1993)	Eq. 6.38	0.00788	6.85	15.9	-2.2

valid for  $1 < T_w/T_b < 2.5$  and  $1.5 \times 10^4 < Re_D < 2.33 \times 10^5$  and  $L/d > 30$ .

Tables 6.4 through 6.9 show the comparison of results between the present simulations and experimental data and the variable property correlations discussed above. The difference between present results and experimental data or correlations, *diff*, is defined in Eq. 4.41. The Nusselt numbers of present simulations matched very well with experimental results. Comparing with the correlations, good agreement was obtained for case 1 for both friction coefficient and Nusselt number. The best agreement was obtained with the correlations of Petukhov and Popov (1963) and McEligot et al. (1965) for friction coefficient and Nusselt number, respectively. However, the simulations of cases 2-6 don't agree as well with the correlations as case 1. The large friction coefficient was overpredicted and the Nusselt number underpredicted. Since the correlations are for turbulent flows, laminarization of flows could be a plausible explanation, which leads to higher friction coefficient and lower Nusselt number.

## 6.9 Summary

To study mixed convection in a vertical turbulent pipe flow, the Favre filtered compressible Navier-Stokes equations were introduced by considering the buoyancy effect in the x-momentum and energy equations. Simulations were performed for air flowing upwards in a vertical pipe with three different constant wall heat fluxes.

Table 6.5 Comparison with variable property correlations for case 2

Correlation	Equation	$C_f$	% diff	$Nu_D$	% diff
Present simulation	–	0.00854	–	11.04	–
Experiment (Shehata and McEligot, 1998)	–	–	–	11.40	-3.16
Humble, Lowdermilk and Desmon (1951)	Eq. 6.40	–	–	13.09	-15.66
Barnes and Jackson (1961)	Eq. 6.41	–	–	14.42	-23.43
Petukhov and Popov (1963)	Eq. 6.37	0.00786	8.65	13.98	-21.03
McEligot et al. (1965)	Eq. 6.42	–	–	12.34	-10.53
Kays and Crawford (1993)	Eq. 6.38	0.0078	9.48	12.49	-11.61

Table 6.6 Comparison with variable property correlations for case 3

Correlation	Equation	$C_f$	% diff	$Nu_D$	% diff
Present simulation	–	0.0105	–	8.86	–
Experiment (Shehata and McEligot, 1998)	–	–	–	9.5	-6.74
Humble, Lowdermilk and Desmon (1951)	Eq. 6.40	–	–	9.711	-8.76
Barnes and Jackson (1961)	Eq. 6.41	–	–	10.79	-17.89
Petukhov and Popov (1963)	Eq. 6.37	0.0087	20.68	10.74	-17.5
McEligot et al. (1965)	Eq. 6.42	–	–	9.18	-3.5
Kays and Crawford (1993)	Eq. 6.38	0.0083	26.5	9.29	-4.6

Table 6.7 Comparison with variable property correlations for case 4

Correlation	Equation	$C_f$	% diff	$Nu_D$	% diff
Present simulation	–	0.00852	–	13.7	–
Experiment (Shehata and McEligot, 1998)	–	–	–	13.6	0.74
Humble, Lowdermilk and Desmon (1951)	Eq. 6.40	–	–	16.18	-15.32
Barnes and Jackson (1961)	Eq. 6.41	–	–	16.785	-18.38
Petukhov and Popov (1963)	Eq. 6.37	0.0088	-3.18	14.24	-3.79
McEligot et al. (1965)	Eq. 6.42	–	–	14.77	-7.24
Kays and Crawford (1993)	Eq. 6.38	0.00795	7.17	14.96	-8.42

Table 6.8 Comparison with variable property correlations for case 5

Correlation	Equation	$C_f$	% diff	$Nu_D$	% diff
Present simulation	–	0.00909	–	9.49	–
Experiment (Shehata and McEligot, 1998)	–	–	–	10.21	-7.05
Humble, Lowdermilk and Desmon (1951)	Eq. 6.40	–	–	12.68	-25.16
Barnes and Jackson (1961)	Eq. 6.41	–	–	13.89	-31.68
Petukhov and Popov (1963)	Eq. 6.37	0.00836	8.73	12.19	-22.15
McEligot et al. (1965)	Eq. 6.42	–	–	11.93	-20.45
Kays and Crawford (1993)	Eq. 6.38	0.00794	14.48	12.08	-21.44

Table 6.9 Comparison with variable property correlations for case 6

Correlation	Equation	$C_f$	% diff	$Nu_D$	% diff
Present simulation	–	0.011	–	7.32	–
Experiment (Shehata and McEligot, 1998)	–	–	–	7.45	-1.75
Humble, Lowdermilk and Desmon (1951)	Eq. 6.40	–	–	8.67	-15.57
Barnes and Jackson (1961)	Eq. 6.41	–	–	9.68	-24.38
Petukhov and Popov (1963)	Eq. 6.37	0.00934	17.77	8.28	-11.59
McEligot et al. (1965)	Eq. 6.42	–	–	8.21	-10.84
Kays and Crawford (1993)	Eq. 6.38	0.00847	29.87	8.31	-11.91

The mean streamwise velocity and temperature profiles of the present simulations were compared with experimental results. Very good agreement with the experimental results was obtained. Unlike the the velocity profiles plotted in wall coordinates, the mean velocity profiles collapsed together close to the low heating velocity profile when plotted in semi-local coordinates.

The plots of velocity fluctuations indicated that high heating suppressed the turbulent intensities due to the low local Reynolds number. The turbulent kinetic energy was dramatically attenuated for the “laminarizing” cases. The same trends were also observed for turbulent shear stresses and heat fluxes, which showed the effects of the reduction of turbulent structures.

The bursting phenomenon was clearly evident near the wall region for the turbulent cases, case 1 and case 4, as shown in the instantaneous contour plots of streamwise velocity and temperature, but diminished for the “laminarizing” cases. The velocity vector plots also showed large scale motions near the wall region for the turbulent cases, but no large scale eddies in the near wall region for the “laminarizing” cases.

Finally, the friction coefficients and Nusselt numbers were compared with property variation correlations. Case 1 compared favorably with the correlations, while cases 2-6 showed large overprediction for friction coefficient and underprediction for Nusselt number, which may indicate the occurrence of laminarization.

## CHAPTER 7. CONCLUSIONS AND RECOMMENDATIONS

A summary of the current research is given in the following section. The significant contributions are listed in Section 7.2. Conclusions drawn from the current work are presented in Section 7.3. Finally, the recommended future work is discussed in Section 7.4.

### 7.1 Summary

A compressible finite volume scheme was developed based on Cartesian coordinates for the large eddy simulation (LES) of turbulent pipe flows with significant property variations using hexahedral and tetrahedral control volumes. The algorithm solves the compressible Favre filtered Navier-Stokes equations in a fully coupled manner with a time-accurate implicit LU-SGS scheme. A time-derivative preconditioning technique was employed to enable the computation of nearly incompressible flows. The code was written in a multiblock frameworks so that it could be applied to complex geometries and be parallelized more easily. Finally, the code was parallelized with the message passing interface (MPI).

The second-order accurate finite volume LES formulation was evaluated by simulating two isothermal flows: turbulent annular flows and pipe flows. A grid independence study was performed for turbulent pipe flows. The results were compared with experimental data and incompressible DNS results. The friction coefficients were compared with empirical correlations.

The finite volume scheme was further evaluated by simulating turbulent pipe flows with very low constant wall heat flux. Two thermal wall boundary conditions were investigated. The results were compared with passive scalar DNS results. The Nusselt numbers and friction coefficients were compared with constant property empirical correlations.

The LES formulation was subsequently used to simulate turbulent mixed convection in a

vertical pipe with high constant wall heat flux by taking into account the buoyancy effects. Significant property variations across the pipe were induced by the high heat transfer. Three cases with three different constant wall heat fluxes were studied and the results were compared with experimental data and DNS results. Comparisons were made between the present results with empirical correlations for the Nusselt numbers and friction coefficients.

## 7.2 Contributions

Three significant contributions were made in this work as listed below.

- A second-order accurate, cell-centered, central differenced finite volume formulation for the compressible Favre filtered Navier-Stokes equations was extended for the axisymmetric geometry based on Cartesian coordinates. To author's knowledge, this was the first application of LES to an axisymmetric geometry with finite volume scheme based on conservation equations in Cartesian coordinates. The advantages of this idea have been listed in section 4.2. Tetrahedral and hexahedral control volumes were used along with the general finite volume scheme. The LU-SGS scheme for general control volumes was successfully implemented. The formulation was validated for isothermal fully developed turbulent pipe flow and turbulent pipe flow with very low heat transfer.
- The step-periodic boundary condition for large eddy simulation was modified to enable the simulation of turbulent flows with very high transfer. A proper distribution along the radial direction for the temperature difference,  $\Delta T_x$ , was proposed and employed in the step-periodic boundary condition when simulating quasi-developed flows. Good results were achieved.
- To the author's knowledge, this work represents the first report of LES of turbulent pipe flow with constant high heat fluxes leading to significant variations in the temperature-dependent fluid properties. The former LES simulations of pipe flows with constant heat fluxes assumed constant fluid properties, while the simulations in this research

investigated the effects of property variation on the turbulent statistics and structures, and the laminarization of flows with very high heat transfer.

### 7.3 Conclusions

Conclusions that can be drawn from this research are listed below.

- The extended finite volume scheme based on Cartesian coordinates was very efficient for the simulation of turbulent pipe flows and annular flows at low Mach numbers by using time-derivative preconditioning and a time-accurate LU-SGS scheme.
- The second-order accurate compressible finite volume LES formulation yielded excellent agreement with experimental and DNS results for isothermal turbulent pipe flows and annular flows with a relatively moderate amount of grid points.
- The mean temperature profiles of the low heating case with two different boundary conditions matched very well with DNS passive scalar results. However, temperature fluctuations in the near wall region were more reasonable with the fixed wall temperature distribution. Good agreement of Nusselt numbers and friction coefficients were obtained when compared to constant property correlations.
- The predicted mean velocity and temperature profiles for cases spanning from turbulence to laminarization compared favorably with experimental results. Good agreement was obtained for the Nusselt numbers compared with the experimental data.
- High heating suppressed the velocity fluctuations and turbulent kinetic energy. Laminarization occurred with a very high heat flux.
- The Nusselt numbers and friction coefficients compared well with variable property correlations for the flow located in the turbulent regime. However, for the flows in “sub-turbulent” and “laminarizing” regions, the Nusselt numbers and friction coefficients were dramatically underpredicted and overpredicted when compared with variable property correlations for turbulent flows. It could be due to the laminarization of the flows.

## 7.4 Recommendations for Future Work

The following recommendations can be made for future work based on the literature that has been reviewed and the experiences with the present work.

- The finite volume formulation could be extended to allow unstructured grids so that more general geometries can be considered.
- The low heat transfer problem due to small temperature differences in Chapter 5 could be overcome by non-dimensionalizing the temperature variable in the code with respect to a temperature difference rather than the reference temperature (Wang, 1994).
- It could be more helpful for understanding the physics of the high temperature flows inside advanced nuclear reactors to simulate rib-roughened annular flows.
- The localized SGS model and mixed model, which are assumed to have a deeper physical basis, could be implemented in this finite volume formulation.
- Step-periodic boundary conditions are very limiting for the LES of practical internal turbulent flows. The Navier-Stokes characteristic boundary condition proposed by Poinso and Lele (1992) could be considered as an alternative outlet boundary condition.
- It would also be very interesting and valuable to enable the code to simulate supercritical water as well as an ideal gas.

**APPENDIX A. JACOBIAN MATRICES FOR FAVRE FILTERED  
SYSTEM OF EQUATIONS**

$$[T] = \begin{bmatrix} \frac{1}{\tilde{T}} & 0 & 0 & 0 & -\frac{\bar{p}}{\tilde{T}^2} \\ \frac{\tilde{u}}{\tilde{T}} & \frac{\bar{p}}{\tilde{T}} & 0 & 0 & -\frac{\bar{p}\tilde{u}}{\tilde{T}^2} \\ \frac{\tilde{v}}{\tilde{T}} & 0 & \frac{\bar{p}}{\tilde{T}} & 0 & -\frac{\bar{p}\tilde{v}}{\tilde{T}^2} \\ \frac{\tilde{w}}{\tilde{T}} & 0 & 0 & \frac{\bar{p}}{\tilde{T}} & -\frac{\bar{p}\tilde{w}}{\tilde{T}^2} \\ c_v + \frac{\tilde{u}^2 + \tilde{v}^2 + \tilde{w}^2}{2\tilde{T}} & \frac{\bar{p}\tilde{u}}{\tilde{T}} & \frac{\bar{p}\tilde{v}}{\tilde{T}} & \frac{\bar{p}\tilde{w}}{\tilde{T}} & -\frac{\bar{p}(\tilde{u}^2 + \tilde{v}^2 + \tilde{w}^2)}{2\tilde{T}^2} \end{bmatrix} \quad (\text{A.1})$$

$$[\Gamma] = \begin{bmatrix} \frac{R}{\tilde{T}} & 0 & 0 & 0 & -\frac{\bar{p}}{\tilde{T}^2} \\ \frac{R\tilde{u}}{\tilde{T}} & \frac{\bar{p}}{\tilde{T}} & 0 & 0 & -\frac{\bar{p}\tilde{u}}{\tilde{T}^2} \\ \frac{R\tilde{v}}{\tilde{T}} & 0 & \frac{\bar{p}}{\tilde{T}} & 0 & -\frac{\bar{p}\tilde{v}}{\tilde{T}^2} \\ \frac{R\tilde{w}}{\tilde{T}} & 0 & 0 & \frac{\bar{p}}{\tilde{T}} & -\frac{\bar{p}\tilde{w}}{\tilde{T}^2} \\ R \left( c_v + \frac{\tilde{u}^2 + \tilde{v}^2 + \tilde{w}^2}{2\tilde{T}} \right) & \frac{\bar{p}\tilde{u}}{\tilde{T}} & \frac{\bar{p}\tilde{v}}{\tilde{T}} & \frac{\bar{p}\tilde{w}}{\tilde{T}} & -\frac{\bar{p}(\tilde{u}^2 + \tilde{v}^2 + \tilde{w}^2)}{2\tilde{T}^2} \end{bmatrix} \quad (\text{A.2})$$

$$[A] = \begin{bmatrix} \frac{\tilde{u}}{\tilde{T}} & \frac{\bar{p}}{\tilde{T}} & 0 & 0 & -\frac{\bar{p}\tilde{u}}{\tilde{T}^2} \\ \frac{\tilde{u}^2}{\tilde{T}} + R & \frac{2\bar{p}\tilde{u}}{\tilde{T}} & 0 & 0 & -\frac{\bar{p}\tilde{u}^2}{\tilde{T}^2} \\ \frac{\tilde{u}\tilde{v}}{\tilde{T}} & \frac{\bar{p}\tilde{v}}{\tilde{T}} & \frac{\bar{p}\tilde{u}}{\tilde{T}} & 0 & -\frac{\bar{p}\tilde{u}\tilde{v}}{\tilde{T}^2} \\ \frac{\tilde{u}\tilde{w}}{\tilde{T}} & \frac{\bar{p}\tilde{w}}{\tilde{T}} & 0 & \frac{\bar{p}\tilde{u}}{\tilde{T}} & -\frac{\bar{p}\tilde{u}\tilde{w}}{\tilde{T}^2} \\ \frac{\tilde{u}\hat{H}}{\tilde{T}} & \frac{\bar{p}(\hat{H} + \tilde{u}^2)}{\tilde{T}} & \frac{\bar{p}\tilde{u}\tilde{v}}{\tilde{T}} & \frac{\bar{p}\tilde{u}\tilde{w}}{\tilde{T}} & -\frac{\bar{p}\tilde{u}(\tilde{u}^2 + \tilde{v}^2 + \tilde{w}^2)}{2\tilde{T}^2} \end{bmatrix} \quad (\text{A.3})$$

$$[B] = \begin{bmatrix} \frac{\tilde{v}}{\tilde{T}} & 0 & \frac{\bar{p}}{\tilde{T}} & 0 & -\frac{\bar{p}\tilde{v}}{\tilde{T}^2} \\ \frac{\tilde{v}\tilde{u}}{\tilde{T}} & \frac{\bar{p}\tilde{v}}{\tilde{T}} & \frac{\bar{p}\tilde{u}}{\tilde{T}} & 0 & -\frac{\bar{p}\tilde{v}\tilde{u}}{\tilde{T}^2} \\ \frac{\tilde{v}^2}{\tilde{T}} + R & 0 & \frac{2\bar{p}\tilde{v}}{\tilde{T}} & 0 & -\frac{\bar{p}\tilde{v}^2}{\tilde{T}^2} \\ \frac{\tilde{v}\tilde{w}}{\tilde{T}} & 0 & \frac{\bar{p}\tilde{w}}{\tilde{T}} & \frac{\bar{p}\tilde{v}}{\tilde{T}} & -\frac{\bar{p}\tilde{v}\tilde{w}}{\tilde{T}^2} \\ \frac{\tilde{v}\hat{H}}{\tilde{T}} & \frac{\bar{p}\tilde{u}\tilde{v}}{\tilde{T}} & \frac{\bar{p}(\hat{H} + \tilde{v}^2)}{\tilde{T}} & \frac{\bar{p}\tilde{v}\tilde{w}}{\tilde{T}} & -\frac{\bar{p}\tilde{v}(\tilde{u}^2 + \tilde{v}^2 + \tilde{w}^2)}{2\tilde{T}^2} \end{bmatrix} \quad (\text{A.4})$$

$$[C] = \begin{bmatrix} \frac{\tilde{w}}{\tilde{T}} & 0 & 0 & \frac{\bar{p}}{\tilde{T}} & -\frac{\bar{p}\tilde{w}}{\tilde{T}^2} \\ \frac{\tilde{w}\tilde{u}}{\tilde{T}} & \frac{\bar{p}\tilde{w}}{\tilde{T}} & 0 & \frac{\bar{p}\tilde{u}}{\tilde{T}} & -\frac{\bar{p}\tilde{w}\tilde{u}}{\tilde{T}^2} \\ \frac{\tilde{w}\tilde{v}}{\tilde{T}} & 0 & \frac{\bar{p}\tilde{w}}{\tilde{T}} & \frac{\bar{p}\tilde{v}}{\tilde{T}} & -\frac{\bar{p}\tilde{w}\tilde{v}}{\tilde{T}^2} \\ \frac{\tilde{w}^2}{\tilde{T}} + R & 0 & 0 & \frac{2\bar{p}\tilde{w}}{\tilde{T}} & -\frac{\bar{p}\tilde{w}^2}{\tilde{T}^2} \\ \frac{\tilde{w}\hat{H}}{\tilde{T}} & \frac{\bar{p}\tilde{u}\tilde{w}}{\tilde{T}} & \frac{\bar{p}\tilde{v}\tilde{w}}{\tilde{T}} & \frac{\bar{p}(\hat{H} + \tilde{w}^2)}{\tilde{T}} & -\frac{\bar{p}\tilde{w}(\tilde{u}^2 + \tilde{v}^2 + \tilde{w}^2)}{2\tilde{T}^2} \end{bmatrix} \quad (\text{A.5})$$

where

$$\hat{H} = c_p \tilde{T} + \frac{1}{2}(\tilde{u}^2 + \tilde{v}^2 + \tilde{w}^2) \quad (\text{A.6})$$

## APPENDIX B. STREAMWISE TEMPERATURE DIFFERENCE FOR QUASI-DEVELOPED FLOW WITH HIGH HEAT TRANSFER

For the pipe flow with high heat transfer resulting in significant property variations, the streamwise temperature difference from the pipe inlet to outlet,  $\Delta T_x$ , is a function of radius,  $r$ . Referring to some experimental results, the dependence of temperature on radius may be assumed as

$$\Delta T_x(r) = c_1 r^n + c_2 \quad (\text{B.1})$$

where the constants,  $c_1$  and  $c_2$ , can be determined by specifying the bulk temperature rise,  $\Delta T_b$ , and wall temperature difference,  $\Delta T_w$ , from the pipe inlet to outlet.

The condition,  $\Delta T_x(1) = \Delta T_w$ , at the wall gives

$$c_1 + c_2 = \Delta T_w \quad (\text{B.2})$$

By assuming the axial conduction and viscous dissipation are negligible, the bulk temperature difference can be calculated with the integration of the energy equation around the solution domain as

$$\Delta T_b = \frac{1}{\rho_b u_b A_c} \int \rho u T dA \Big|_{x=L_x} - \frac{1}{\rho_b u_b A_c} \int \rho u T dA \Big|_{x=0} = \frac{4q_w}{\dot{m} D} L_x \quad (\text{B.3})$$

Equation B.3 can be expand as

$$\Delta T_b = \frac{1}{\rho_b u_b A_c} \left[ \int \rho u (T(0, r) + \Delta T_x(r)) dA \Big|_{x=L_x} - \int \rho u T(0, r) dA \Big|_{x=0} \right] = \frac{4q_w}{\dot{m} D} L_x \quad (\text{B.4})$$

Since the mass flux is assumed to be periodic in the streamwise direction, Equation B.4 is reduced to

$$\Delta T_b = \frac{1}{\rho_b u_b A_c} \int \rho u \Delta T_x(r) dA \Big|_{x=L_x} = \frac{4q_w}{\dot{m} D} L_x \quad (\text{B.5})$$

Substitution of Eq. B.1 into Eq. B.5 gives

$$\Delta T_b = \frac{1}{\rho_b u_b A_c} \left[ c_1 \int \rho u r^n dA + c_2 \int \rho u dA \right] \Big|_{x=L_x} = \frac{4q_w}{\frac{\dot{m}}{A_c} D} L_x \quad (\text{B.6})$$

or

$$\Delta T_b = c_1 I_{\rho u r} + c_2 \quad (\text{B.7})$$

where

$$I_{\rho u r} = \frac{1}{\rho_b u_b A_c} \int \rho u r^n dA \Big|_{x=L_x} \quad (\text{B.8})$$

Consequently, the constants,  $c_1$  and  $c_2$ , can be evaluated using Eq B.2 and Eq. B.7 as

$$c_1 = \frac{\Delta T_b - \Delta T_w}{I_{\rho u r} - 1} \quad (\text{B.9})$$

$$c_2 = \frac{I_{\rho u r} \Delta T_w - \Delta T_b}{I_{\rho u r} - 1} \quad (\text{B.10})$$

**BIBLIOGRAPHY**

- Abe, K., Kondoh, T. and Nagano, Y. (1994). "A New Turbulence Model For Predicting Fluid Flow and Heat Transfer In Separating and Reattaching Flows-I. Flow Field Calculations," *Int. J. Heat Mass Transfer*, Vol. 37, pp. 139-151.
- Ansari, A. and Strang, W.Z. (1996). "Large-Eddy Simulation of Turbulent Mixing Layers," *AIAA Paper*, 96-0684.
- Bankston, C. A. and McEligot, D. M. (1970). "Turbulent and Laminar Heat Transfer to Gases with Varying Properties in the Entry Region of Circular Ducts," *Int. J. Heat Mass Transfer*, Vol. 13, pp. 319-344.
- Barnes, J. F. and Jackson, J. D. (1961). "Heat Transfer to Air, Carbon Dioxide and Helium Flowing through Smooth Circular Tubes under Conditions of Large Surface / Gas Temperature Ratio," *Journal of Mechanical Engineering Science*, Vol. 3, pp.303-314.
- Bates, J. A., Schmall, R. A., Hansen, G. A. and McEligot, D. M. (1974). "Effects of Buoyancy Body Forces on Forced Convection in Heated Laminarizing Flows," *Int. Heat Transfer Conf.*, Tokyo, Japan, Vol. II, pp. 141-145.
- Benocci, C. and Pinelli, A. (1990). "The Role of the Forcing Term in the Large Eddy Simulation of Equilibrium Channel Flow," *Engineering Turbulence Modeling and Experiments*, W. Rodi and E. N. Ganic (Eds), New York, pp. 287-296.
- Boersma, B.J. and Nieuwstadt, F.T.M. (1996). "Large-Eddy Simulation of Turbulent Flow in a Curved Pipe," *Transaction of ASME*, Vol. 118, pp. 248-254.
- Bradshaw P. (1971). *An Introduction to Turbulence and its Measurement*, Pergomon, New York.
- Cebeci, T. and Smith, A.M.O. (1974). *Analysis of Turbulent Boundary Layers*, Academic Press, New York
- Ciofalo, M. and Colins, M.W. (1992). "Large-Eddy Simulation of Turbulent Flow and Heat Transfer in Plane and Rib-Roughened Channels," *International Journal for Numerical Methods in Fluids*, Vol. 15, pp. 453-489

- Chambers F. W., Murphy H. D. and McEligot D. M. (1983). "Laterally Converging Flow. Part 2. Temporal Wall Shear Stress," *Journal of Fluid Mechanics*, Vol. 127, pp. 403-428.
- Chen, K.-H. and Shuen, J.-S. (1994). "Three Dimensional Coupled Implicit Methods for Spray Combustion Flows at All Speeds," *AIAA Paper*, 94-3047.
- Choi, Y.-H. and Merkle, C. L. (1993). "The Application of Preconditioning in Viscous Flows," *Journal of Computational Physics*, Vol. 105, pp. 207-223.
- Coon, C. W. and Perkins, H. C. (1970). "Transition From The Turbulent to Laminar Regime for Internal Convective Flow with Large Property Variations," *Transactions of ASME series C*, Vol. 92, pp. 506-512.
- Cotton, D., and Kerwin, P. J. (1995). "A Variant of the Low-Reynolds-Number Two-Equation Turbulence Model Applied to Variable Property Mixed Convection Flows," *Int. J. Heat Fluid Flow*, Vol. 16, pp. 486-492.
- Currie, I.G. (1974). *Fundamental Mechanics of Fluids*, McGraw-Hill, Inc., New York
- Dailey, L.D. and Pletcher, R.H. (1998). "Large Eddy Simulation of Constant Heat Flux Turbulent Channel Flow with Property Variations," *36th AIAA Aerospace Sciences Meeting and Exhibit*, January 12-15.
- Dailey, L. D. (1997). "Large Eddy Simulation of Turbulent Flows with Variable Property Heat Transfer Using a Compressible Finite Volume Formulation," *Ph.D. thesis*, Iowa State University, Ames, IA.
- Deardroff, J.W. (1970). "A Numerical Study of Three-Dimensional Turbulence Channel Flow at Large Reynolds Number," *Journal of Fluid Mechanics*, Vol. 41, pp. 452-456
- Eggles, J.G.M. and Nieuwstadt, F.T.M. (1993). "Large-eddy Simulation of Turbulent Flow in an Axially Rotating Pipe." *Proceeding of the 9th Symposium on Turbulent Shear flows*, pp. 310-1-310-4.
- Eggels, J. G. M. (1994). "Direct and Large Eddy Simulation of turbulent flow in a cylindrical pipe geometry," *PhD thesis*, Delft University of Technology, the Netherlands.
- Eggels, J.G.M., Unger, F., Weiss, M.H., Westerweel, J., Adrian, R.J., Friedrich, R. and Nieuwstadt, F.T.M. (1994). "Fully Developed Turbulent Pipe Flow: a Comparison Between Direct Numerical Simulation and Experiment," *Journal of Fluid Mechanics*, Vol. 268, pp. 175-209.
- Ezato, K., Shehata, A.M., Kunugi, T. and McEligot, D.M. (1999). "Numerical Prediction of Transitional Features of Turbulent Forced Gas Flows in Circular Tubes With Strong Heating," *Transactions of the ASME*, Vol. 121, pp. 546-555.

- Favre, A. (1983). "Turbulence: Space-Time Statistical Properties and Behavior in Supersonic Flows," *Physics of Fluids*, Vol. 26, pp. 2851-2863
- Feng, J. and Merkle, C. L. (1990). "Evaluation of Preconditioning Methods for Time-Marching Methods," *AIAA Paper*, 90-0016.
- Ferziger, J. H. and Peric, M. (1996). *Computational Methods for Fluid Dynamics*, Springer, New York.
- Fujii, S. N., Akino, N., Hishida, M., Kawamura, H. and Sanokawa, K. (1991). "Experimental and Theoretical Investigations on Heat Transfer of Strongly Heated Turbulent Gas Flow in an Annular Duct," *JSME International J., Ser. II*, Vol. 34, No. 3, pp. 348-354.
- Germano, M., Piomelli, U. Moin, P. and Cabot, W. (1991). "A Dynamic Subgrid-scale Eddy Viscosity Model", *Journal of Fluid Mechanics*, Vol. 177, pp. 133-166.
- Ghosal, S. and Moin P. (1995). "The Basic Equations of the Large Eddy Simulation of Turbulent Flows in Complex Geometry", *Journal of Computational Physics*, Vol. 118, pp. 24-37.
- Gnielinski, V. (1976). "Neue Gleichungen für den Wärme- und den Stoffübergang in Turbulent durchströmten Rohren und Kanälen," *International Chemical Engineering*, Vol. 16, pp. 359-368.
- Grasso, F. and Marini, M. (1991). "LU Implicit TVD Scheme for the Solution of Viscous Two Dimensional High Speed Flows," *AIAA Paper*, 91-1573.
- Härtel, C. and Kleiser, L. (1997). "Galilean Invariance and Filtering Dependence of Near-wall Grid Scale/Subgrid-scale Interactions in Large-eddy Simulation," *Phys. Fluids*, Vol. 9, 473-475.
- Huang, P. G., Coleman, G. N. and Denmon, L. G. (1995). "Compressible Turbulent Channel Flow - A Close Look Using DNS Data," *AIAA Paper*, 95-0584.
- Humble, L. V., Lowdermilk, W. H. and Desmon, L. G. (1951). "Measurement of Average Heat Transfer and Friction Coefficients for Subsonic Flow of Air in Smooth Tubes at High Surface and Fluid Temperatures," *NACA Report 1020*.
- Iida, O. and Kasagi, N. (1997). "Direct Numerical Simulation of Unsteady Stratified Turbulent Channel Flow," *Journal of Heat Transfer*, Vol. 119, pp. 53-61.
- Jackson, J. D., Cotten, M. A. and Axcell, B. P. (1989). "Studies of Mixed Convection in Vertical Tubes," *Int. J. Heat and Fluid Flow*, Vol. 10, pp. 2-15.

- Kakac, S. (1987). "The Effect of Temperature-Dependent Fluid Properties on Convective Heat Transfer," *Handbook of Single-Phase Convective Heat Transfer*, Kakac, S., Shah, R. K., and Aung, W. (Eds), John Wiley and Sons, New York, pp. 18.1-18.56.
- Kasagi, N., Kuroda, A. and Hirata, M. (1989). "Numerical Investigation of Near Wall Turbulent Heat Transfer Taking Into Account the Unsteady Heat Conduction in the Solid Wall," *Journal of Heat Transfer*, Vol. 111, pp. 53-61.
- Kawamura, H. (1979). "Analysis of Laminarization of Heated Turbulent Gas Using a Two-Equation Model of Turbulence," *Proc. 2nd Intl. Symp. Turb. Shear Flow*, London, pp. 18.16-18.21.
- Kawamura, H., Nakamura, S., Satake, S. and Kunugi, T. (1994). "Large Eddy Simulations of Turbulent Heat Transfer in a Concentric Annulus," *Thermal Science & Engineering*, pp. 16-25 (In Japanese).
- Kays, W. M. and Crawford, M. E. (1993). *Convective Heat and Mass Transfer*, 3rd ed., McGraw-Hill, Inc., New York.
- Kim, J., Moin, P. and Moser, R. (1987). "Turbulence Statistics in Fully Developed Channel Flow at Low Reynolds Number," *Journal of Fluid Mechanics*, Vol. 177, pp. 133-166.
- Kim, J., Moin, P. (1989). "Transport of Passive Scalars in a Turbulent Channel Flow," *Turbulent Shear Flows 6*, Springer-Verlag.
- Kline, S. J., Reynolds, W. C., Schraub F. A. and Rundstadler P. W. (1967). "The Structure of Turbulent Boundary Layers," *Journal of Fluid Mechanics*, Vol. 30, pp. 741-773.
- Laufer, J. (1954). "The Structure of Turbulence in Fully Developed Pipe Flow," *NACA Report*, pp. 1174.
- Lauder, B. E. and Sharma, B. I. (1974). "Application of the Energy-Dissipation Model of Turbulence to the Calculation of Flow Near a Spinning Disc," *Lett. Heat Transfer*, Vol. 1, pp. 131-138.
- Lawn, C. J. (1971). "The Determination of the Rate of Dissipation in Turbulent Pipe Flow," *Journal of Fluid Mechanics*, Vol. 48, PP. 477-505.
- Leonard, A. (1974). "Energy Cascade in Large Eddy Simulation of Turbulent Fluid Flow," *Adv. in Geophys.*, 18A, pp. 237
- Lilly, D. K. (1992). "A Proposed Modification of the Germano Subgrid-Scale Closure Method," *Physics of Fluids A*, Vol. 4, 633-635.
- McAdams (1954). *Heat Transmission*, 3rd ed., McGraw-Hill, New York

- McEligot, D. M. (1986). "Convective Heat Transfer in Internal Gas Flows with Temperature-Dependent Properties," *Advances in Transport Processes*. Vol. 4, pp. 113-200.
- McEligot, D. M. and Bankston, C. A. (1969). "Turbulent Predictions for Circular Tube Laminarization by Heating," *ASME Paper*, 69-HT-52.
- McEligot, D. M., Coon, C. M. and Perkins, H. C. (1970). "Relaminarization in Tubes," *Int. J. Heat Mass Transfer*, Vol. 13, pp. 431-433.
- McEligot, D. M. and Shehata, A., and Kunugi, T. (1998). "Prediction of Strongly-Heated Internal Gas Flows," *Engineering Foundation Conference Turbulent Heat Transfer II*, Manchester, UK.
- McEligot, D. M., Magee, P. M. and Leppert, G. (1965). "Effect of Large Temperature Gradients on Convective Heat Transfer: Downstream Region," *Journal of Heat Transfer*, Vol. 88, pp. 67-76.
- Meneveau, C. and Katz J. (2000). "Scale-Invariance and Turbulence Models for Large-eddy Simulation," *Annu. Rev. Fluid Mech.*, Vol 32, 1-32.
- Meng, N., Pletcher, R.H. and Simons, T. (1998). "Large Eddy Simulation of a Turbulent Channel Flow with a Rib-roughened Wall," *AIAA Paper* 99-3356
- Meng, N. (2000). "Large Eddy Simulation of Turbulent Flows with Property Variations, Rotation and Complex Geometry," *Ph.D. thesis*, Iowa State University, Ames, IA.
- Mikielewicz, D. P. (1994). "Comparative Studies of Turbulent Models under Conditions of Mixed Convection with Variable Properties in Heated Vertical Tubes," *Ph. D. Thesis*, Univ. Manchester.
- Mittal, R. (1996). "Progress on LES of Flow Past a Circular Cylinder," *Annual Research Briefs*, Center for Turbulence Research, pp. 233-241.
- Moin, P. and Kim, J. (1982). "Numerical Investigation of Turbulent Channel flow," *Journal of Fluid Mechanics*, Vol. 118, pp. 341-377.
- Moin, P., Squires, K., Cabot, W. and Lee S. (1991). "A Dynamic Subgrid-Scale Model for Compressible Turbulence and Scalar Transport," *Physics of Fluids A*, Vol.3, pp. 2746-2757.
- Nagano, Y. and Shimada, M. (1995) "Computational Modeling and Simulation of Turbulent Flows," *Computational Fluid Dynamics Review*, Hafez, M. and Oshima, K. (Eds), Chichester: John Wiley & Sons, pp. 695-714.

- Nakajima, M., Fukui, K., Ueda, H. and Mizushima, T. (1979). "Buoyancy Effects on Turbulent Transport in Combined Free and Forced Convection between Vertical Parallel Plates," *Int. J. Heat Mass Transfer*, Vol. 23, pp. 1325-1336.
- Nicoud, F. and Poinso, T. (1999). "DNS of a Channel Flow with Variable Properties," *Proceedings of the First International Symposium of Turbulence and Shear Flow Phenomena*, Santa Barbara, California.
- Niederschulte, M., Adrian, R. and Hanratty, T. (1990). "Measurements of Turbulent Flow in a Channel at Low Reynolds Numbers," *Experiments in Fluids*, Vol. 9, pp. 222-230.
- Nishimura, M., Fujii, S., Shehata, A. M., Kunugi, T. and McEligot, D. M. (2000). "Predictions of Forced Gas Flows in Circular Tubes at High Heat Fluxes Accompanied by Laminarization," *J. Nuclear Science and Technology*, Vol. 37, No. 7, pp. 581-594.
- Ogawa, M., Kawamura, H., Takizuka, T. and Akino, N. (1982). "Experiments on Laminarization of Strongly Heated Gas Flow in a Circular Tube," *J. At. Energy Soc., Japan*, Vol. 24, No. 1, pp. 60-67 (in Japanese).
- Ogawa, M. and Kawamura, H. (1986). "Experimental and Analytical Studies on Friction Factor of Heated Gas Flow in Circular Tube," *J. At. Energy Soc., Japan*, Vol. 28, No. 10, pp. 957-965 (in Japanese).
- Orlandi, P. and Fatica, M. (1997). "Direct Numerical Simulation of Turbulent Flow in a Pipe Rotating about its Axis," *Journal of Fluid Mechanics*, Vol. 343, pp. 43-72.
- Patel, V. C. and Head, M. R. (1969). "Some Observations on Skin Friction and Velocity Profiles in Fully Developed Pipe and Channel Flows," *Journal of Fluid Mechanics*, Vol. 38, 181-201.
- Perkins, K. R. (1975). "Turbulence Structure in Gas Flows Laminarizing by Heating," *Ph. D. thesis*, University of Arizona.
- Petukhov, B. S. and Popov, V. N. (1963). "Theoretical Calculation of Heat Exchange and Frictional Resistance in Turbulent Flow in Tubes of an Incompressible Fluid With Variable Physical Properties," *High Temperature*, Vol. 1, pp. 69-83.
- Piomelli, U., Moin, P., and Ferziger, J. H. (1988). "Model Consistency in Large Eddy Simulation of Turbulent Flows," *Physics of Fluids*, Vol. 31, pp. 1884-1891.
- Piomelli, U., Cabot, W.H., Moin, P. and Lee, S. (1991). "Subgrid-scale Backscatter in Transitional and Turbulent Flows," *Physics of Fluids*, A 3, 1766-1771.
- Piomelli, U. and Zhang T.A. (1991). "Large-Eddy-Simulation of Transitional Channel Flow," *Comput. Phys. Commun.*, Vol. 65, 224-230

- Pletcher, R. H. and Chen, K.-H. (1993). "On Solving the Compressible Navier-Stokes Equations for Unsteady Flows at Very Low Mach Numbers," *AIAA Paper*, 93-3368.
- Poinsot, T. J. and Lele, S. K. (1992). "Boundary Conditions for Direct Simulations of Compressible Viscous Flows," *Journal of Computational Physics*, Vol. 101, pp. 104-129.
- Polyakov, A. F. (1973). "Transient Effects due to Thermogravity in Turbulence and Heat Transfer," *Heat Transfer Sov. Res.* 11, pp. 90-98.
- Prandtl, L. (1944). *Führer Durch die Stömungslehre*, Vieweg, Braunschweig, pp. 359.
- Rieger, H. and Jameson, A. (1988). "Solution of Steady Three Dimensional Compressible Euler and Navier Stokes Equations by an Implicit LU Scheme," *AIAA Paper*, 88-0619.
- Rogallo, R.S. and Moin, P. (1984). "Numerical Simulation of Turbulent Flows," *Ann. Rev. Fluid Mech.*, Vol. 16, 99-137.
- Satake, S. and Kawamura, H. (1995). "Large Eddy Simulation of Turbulent Flow in Concentric Annuli With a Thin Inner Rod," *Turbulent Shear Flow*. Vol. 9, F. Durst, Kasagi, N., Launder, B. E., Schmidt, F. W., Suzuki, K. & Whitelaw, J. H. (Eds), Berlin: Springer, pp. 259-281.
- Satake, S. and Kunugi, T. (1998a). "Direct Numerical Simulation of Turbulent Pipe Flow," (in Japanese), *Trans. JSME 64-617B*, pp. 65-70.
- Satake, S. and Kunugi, T. (1998b). "Direct Numerical Simulation of an Impinging Jet into Parallel Disks," *Int. J. of Numerical Methods for Heat & Fluid Flow*, Vol. 8, No. 7, pp. 768-780.
- Satake, S. and Kunugi, T. (1998c). "Direct Numerical Simulation of Turbulent Pipe Flow with Non-Uniform Surface Heat Flux," *Thermal Sci. Eng.*, Vol. 6, No. 2, pp. 1-7 (In Japanese).
- Satake, S. and Kunugi, T. (1998d). "Direct Numerical Simulation of Turbulent Heat Transfer in an Axially Rotating Pipe Flow: Reynolds Stress and Scalar-Flux Budgets," *Bulletin of the America Physical Society*, Vol. 43, No. 9, pp. 1976.
- Satake, S. and Kunugi, T. (1999). "Direct Numerical Simulation of Turbulent Pipe Flow with Uniform Surface Heat Flux (in Japanese)", *Trans. JSME*, 65-631B, pp. 192-197.
- Satake, S., Kunugi, T., Mohsen Shehata, A. and McEligot, D.M. (2000). "Direct Numerical Simulation for Laminarization of Turbulent Forced Gas Flows in Circular Tubes with Strong Heating," *Int. J. Heat and Fluid Flow*, Vol. 21, 526-534.
- Schlichting, H. (1979). *Boundary-layer Theory (7th ed.)*. McGraw-Hill, Inc., New York.

- Shehata, A. M. and D. M. McEligot (1995). "Turbulence Structure in the Viscous Layer of Strongly Heated Internal Gas Flows," *Tech. Report INEL-95/0223*, Idaho National Engineering Laboratory.
- Shehata, A. M. and D. M. McEligot (1998). "Mean Structure in the Viscous Layer of Strongly-Heated Internal Gas Flows : Measurements," *Int. J. Heat Mass Transfer*, Vol. 41, pp. 4297-4313.
- Shuen, J.-S., Chen, K.-H., and Choi, Y. (1992). "A Time-Accurate Algorithm for Chemical Non-Equilibrium Viscous Flows at All Speeds," *AIAA Paper*, 95-0203.
- Smagorinsky, J. (1963). "General Circulation Experiments With the Primitive Equations: Part I. The Basic Experiment," *Monthly Weather Review*, Vol. 91, pp. 99-164.
- Speziale, C. G. (1985). "Galilean Invariance of Subgrid-scale Stress Models in the Large-eddy Simulation of Turbulence," *Journal of Fluid Mechanics*, Vol. 156, pp. 55-62.
- Spyropoulos, E. T. and Blaisdell, G. A. (1995). "Evaluation of the Dynamic Subgrid-Scale Model for Large Eddy Simulation of Compressible Turbulent Flows," *AIAA Paper*, 95-0355
- Tafti, D. K. and Vanka, S. B. (1990). "Large Eddy Simulation of Channel Flow Using Finite-Difference Techniques," *Technical report*, Department of Mechanical Engineering, University of Illinois at Urbana-Champaign.
- Tennekes, H. and Lumley, J. L. (1972). *A First Course in Turbulence*, the MIT Press.
- Torri, S., Shimizu, A., Hasegawa, S. and Kusama, N. (1991). "Laminarization of Strongly Heated Annular Gas Flows," *JSME International J., Ser II*, Vol. 34, No. 2, pp. 157-168.
- Torri, S., Shimizu, A., Hasegawa, S. and Higasa, M. (1993). "Numerical Analysis of Laminarizing Circular Tube Flows by Means of a Reynolds Stress Turbulent Model," *Heat Transfer - Japanese Research*, Vol. 22, pp. 154-170.
- Torri, S. and Yang, W.-J (1997). "Laminarization of Turbulent Gas Flow Inside a Strongly Heated Tube," *Int. J. Heat Mass Transfer*, Vol. 40, pp. 3105-3117.
- Turkel, E. (1987). "Preconditioned Methods for Solving the Incompressible and Low Speed Compressible Equations," *Journal of Computational Physics*, Vol. 72, pp. 277-298.
- Unger, F. and Friedrich, R. (1991). "Large Eddy Simulation of Fully-developed Pipe Flow," *Proceedings of Eighth Symposium on Turbulent Shear flows*, pp. 19-3-1 - 19-3-6.
- Unger, F. and Friedrich, R. (1993). "Large Eddy Simulation of Fully-Developed Pipe Flow," *Flow Simulations of High Performance Computers 1 (ed. L. H. Hirschel), NCFM*, Vol. 38, pp. 201-216.

- Verzicco, R. and Orlandi, P. (1996). "A Finite-Difference Scheme for Three-Dimensional Incompressible Flows in Cylindrical Coordinates," *Journal of Computational Physics*. Vol. 123, pp. 402-414.
- Vogel, J.C. and Eaton, J.K. (1984). "Heat Transfer and Fluid Mechanics Measurements in the Turbulent Reattaching Flow Behind a Backward Facing Step," *Report MD-44*, Thermosciences Division, Dept. Mechanical Engr., Stanford Univ.
- Volpe, G. (1991). "On the Use and Accuracy of Compressible Flow Codes at Low Mach Numbers," *AIAA Paper*. 91-1662.
- Vreman, A.W., Geurts, B.J., Kuerten, J.G.M., and Zandbergen, P.J. (1992). "A Finite Volume Approach to Large Eddy Simulation of Compressible, Homogeneous, Isotropic, Decaying Turbulence," *International Journal for Numerical Methods in Fluids*, Vol. 15, pp. 799-816.
- Vreman, A.W., Geurts, B.J., Kuerten, H. (1995), "Subgrid-modeling in LES of Computational Flow," *Applied Scientific Research*, Vol. 54, pp. 191-203.
- Wang, W.-P. and Pletcher, R.H. (1995). "Evaluation of Some Coupled Algorithms for Large Eddy Simulation of Turbulent Flow Using a Dynamic SGS Model," *AIAA Paper* 95-2244.
- Wang, W.-P. and Pletcher, R.H. (1996). "On the Large Eddy Simulation of a Turbulent Channel Flow with Significant Heat Transfer," *Physics of Fluids*, Vol. 8, pp. 3354-3366.
- Westerweel, J., Draad, J.G.Th., van der Hoeven and van Oord, J. (1996). "Measurement of Fully-developed Turbulent Pipe Flow with Digital Particle Image Velocimetry," *Experiments in Fluids*, Vol. 20, pp. 165-177.
- Yang, K.-S. and Ferziger, J.H. (1993). "Large-eddy Simulation of Turbulent Obstacle Flow Using a Dynamic Subgrid-scale Model," *AIAA Journal*, Vol. 31, pp. 1406-1413.
- Yang, Z.-y. (2000). "Large Eddy Simulation of Fully Developed Turbulent Flow in a Rotating Pipe," *International Journal for Numerical Methods in Fluids*, Vol. 33, 681-694.
- Yoon, S. and Jameson, A. (1987). "An LU-SSOR Scheme for the Euler and Navier-Stokes Equations," *AIAA Paper*, 87-600.
- Yoshizawa, A. (1986). "Statistical Theory for Compressible Turbulent Shear Flows, With the Application to Subgrid Modeling," *Physics of Fluids A*, Vol. 5, pp. 3186-3196.
- Zang, Y., Street, R.L. and Koseff, J.R. (1993). "A Dynamic Mixed Subgrid-scale Model and its Application to Turbulent Recirculating Flows," *Physics Fluids*, Vol. 5, pp. 3186-3196.

## ACKNOWLEDGMENTS

I would like to take this opportunity to express my gratitude to those who helped me finish this thesis.

I am deeply grateful to my major professor, Dr. Richard H. Pletcher. His great enthusiasm and integral view on research has made a deep impression on me. His guidance, patience and support throughout this research and the writing of this thesis have been invaluable. I would also like to thank Drs. Francine Battaglia, Soma Chaudhuri, Gerald M. Colver, Ganesh R. Rajagopalan, John C. Tannehill for being on my program of study committee.

The current research was supported by the Department of Energy through grant DE-FG03-995F21924 under the NERI program. The majority of this research was conducted using the IBM-SP2, Origin 2000 and Origin 3800 at University of Minnesota Supercomputing Institute and the Origin 2000 at Iowa State University High Performance Computing Center. These institutes are all greatly appreciated.

My colleagues in the CFD laboratory of Iowa State University, Ravi, Ning, Joon, Steve, Yang, Charles, Kunlun, Anup, Nan, John, Fashid, and Jin are all acknowledged for their help and for the good time together.

My special thanks is offered to Lyle Dailey, who developed the basic frame work of the code in this research. I benefited tremendously from his papers and codes.

Finally, I would like to dedicate this work to my parents, JiaYan and Suzhen, and my wife, Li. Thank you so much for your love, support and patience.